Università degli Studi di Trieste

Dipartimento di Fisica

Corso di Laurea Magistrale in Fisica
Curriculum in Fisica della Materia Condensata

Multimode Heterodyne Detection for time domain studies of quantum materials

Detezione eterodina multimodo risolta in tempo per lo studio di materiali quantistici

Laureando:
Enrico Maria Rigoni

Relatore:
Prof. Daniele Fausti

Correlatori:
Dott.ssa Francesca Giusti
Dott. Filippo Glerean

ANNO ACCADEMICO 2019–2020

Che cosa facciamo dopo pranzo?
E che cosa facciamo domani?
E nei prossimi trent'anni?

F. S. Fitzgerald

Contents

Introduction **1**

1 Detection of light quantum states **4**
1.1 Quantum state of a physical system 5
1.2 Balanced Heterodyne Detection 7
1.3 Quantum noise sensitivity 10
1.4 Generalization to multimode quantum states 12

2 Experimental setup **14**
2.1 Setup 15
2.1.1 Multimode Heterodyne Detection 16
2.2 Pulse shaping for frequency resolving a single channel detector heterodyne measurement 20
2.2.1 Ultrafast Pulse-Shaping 20
2.2.2 Two dimensional Liquid Crystal Spatial Light Modulator 21
2.2.3 Pulse shaping capabilities 24
2.2.4 Pulse shaper calibration 27
2.3 Balanced Heterodyne detection using polarizing beam splitters 29
2.4 Detection system 30
2.4.1 Fast acquisition system: photodiodes arrays 31
2.4.2 Low noise configuration: differential detector 33
2.5 Carrier-Envelope Phase stabilization system 34

3 Characterization of the interferometric setup for optical tomography with short pulses **38**
3.1 Characterization of the photonic noise 39
3.1.1 Propagation of classical noise: a Beam Splitter Model 39
3.1.2 Shot noise linearity test 41
3.1.3 Interferometer stability 44
3.2 A rescaling procedure for the quadrature field for photon number estimations . . . 46
3.2.1 Rescaling procedure 46
3.2.2 Photon number estimation 49

4 Multimode time domain heterodyne detection study of coherent phononic oscillations in $\alpha-$quartz **52**
4.1 Mean value maps 53
4.2 Amplitude and Phase maps 55
4.3 Amplitude map: Impulsive Stimulated Raman Scattering 57
4.3.1 Periodic oscillation: a phonon signature 57
4.3.2 Spectral weight redistribution via ISRS 58
4.4 Phase map: Linear Refractive Modulation 61
4.4.1 Linear modulation of the refractive index (LRM) 62

5 Generation of an incoherent superposition of quantum states **66**
5.1 Second Harmonic Generation with a collinear resonant pump. 67
5.2 Mean value study on a Beta Barium Borate crystal (BBO) 69
5.3 Distribution Study of the pump second harmonic heterodyne trace 71
5.3.1 Distribution vs quadrature phase 71
5.3.2 Distribution vs pulse frequencies 75
5.3.3 Distribution vs pump delay 79
5.3.4 Pump power test 81
5.4 The origin of bimodal distribution: phase uncertainty 83
5.4.1 CEP test 87
5.5 Quantitative estimations by means of Pattern Function Tomography 90
5.5.1 Pattern Function Quantum Tomography 90
5.5.2 Quadrature expectation values 92
5.5.3 Photon number estimation 94

Conclusions **98**

Riassunto **101**

Appendices **103**

A A Beam Splitter Model for Heterodyne Detection **104**

B A Beam Splitter Model for Balanced Heterodyne Detection with polarizing beam splitters **107**

C Pattern Function Quantum Tomography for a coherent state **110**

Ringraziamenti **115**

Introduction

The study of low energy excitations in solids experienced a significant boost with the advent of femtosecond pulsed lasers. In particular, approaching femtosecond time scales enables the possibility of detecting coherent vibrational states with a time resolution that is shorter than their characteristic oscillation period.

The typical technique used to study these phenomena is the Pump and Probe one (P&P). In a P&P experiment, two pulses impinge on a sample. The first one, named *pump*, triggers an excitation in the system. Subsequently the second pulse, dubbed *probe*, interacts with the excited system after a variable time delay and is finally acquired. By changing the time delay between the two pulses, we can investigate the evolution of the excited system mapped in the spectral modifications of the probe pulse.

Quantum Mechanics establishes that the knowledge of the state of a system combined with its evolution laws enables the prediction of any possible outcome of any possible measurement performed on that system. In a P&P experiment, this is achieved with the full reconstruction of the probe quantum state.

Unfortunately, standard intensity measurements do not suffice for this task. Indeed, intensity is related to the electric field spectral amplitude, but doesn't carry any information about the spectral phase, that is the other observable characterizing a light quantum state.

In order to perform a phase-resolved measurement, and hence to fully reconstruct the probe state, other techniques must be adopted. In particular, in this thesis we couple P&P technique with *Balanced Heterodyne Detection*.

Balanced Heterodyne Detection is an interferometric technique where the beam under study, typically named *signal*, interferes with a strong classical reference beam called *local oscillator* (LO). By tuning the phase relation between signal and LO, we're able to phase-resolve signal electric field and hence fully reconstruct its quantum state. Thus, with the combination of P&P technique and Balanced Heterodyne Detection of the probe pulse, we can address both amplitude and phase spectral modifications due to system excitations.

Moreover, ultrashort short light pulses exhibit a broad spectral content according to Heisenberg uncertainty principle. This feature can be exploited to perform frequency resolved measurements.

In this thesis we present the experimental realization of an innovative frequency-resolved Balanced Heterodyne Detection setup, that hence provides the full reconstruction of a multimode light quantum state. Thanks to this possibility, we can selectively have access to amplitude and phase of each spectral component of the probe pulse and monitor their out-of-equilibrium dynamics.

We exploit the potentiality of the setup to address the coherent evolution of lattice vibrations in solid state systems. In particular, we investigate the presence of phonons in an $\alpha-$quartz crystal. We use this crystal since no electronic transitions are dipole allowed within the pump or probe bandwidth. This enables us to treat probe-matter interaction as an effective photon-phonon coupling and hence to find in the probe spectral features direct signature of the phonon.

We underline that we can look for phonon signature in both amplitude and phase of each spectral component. As we'll see, this analysis unveils different dynamic responses for the two observables. This is linked to the different phenomena that affect amplitude and phase dynamics.

In particular, spectral amplitude is dominated by *Impulsive Stimulated Raman Scattering*, an intrinsic multimode process that creates/annihilates a phonon redistributing the spectral weight inside the light pulse. On the contrary, spectral phase dynamics is dominated by *Linear Refractive Modulation*, i.e. a change in the refractive index of the material due to a displacement of atoms positions.

However, potentialities of our setup do not limit to standard mean value measurements. Indeed, shot by shot pulse acquisition provided by our detection system enables the access to the full statistics of the measurement.

Moreover, Balanced Heterodyne Detection maintains classical extrinsic noise below the intrinsic fluctuations of the number of photons (shot-noise regime). Therefore, field fluctuations we detect pertain to the fundamental quantum nature of light.

We exploit these capabilities of our setup to study the second harmonic generation process of the pump pulse and show how higher order momenta can encode information hidden in the mean value of an observable.

In particular, we generate a phase-randomized quantum state relying on the random relative phase between pump and local oscillator pulses. Performing an analysis on measurements distribution, we provide a full characterization of the state and an insight on its originating process.

The thesis is organized as follows:

- In Chapter 1 we introduce the concept of "quantum state measurement" and provide the theoretical description of Balanced Heterodyne Detection. After showing the capability of the technique to measure quantum fluctuations, we end the Chapter with an extension of the formalism to multimode light quantum states.

- Chapter 2 presents the Multimode Balanced Heterodyne Detection setup specifically developed in the Q4Q laboratory at Elettra Sincrotrone Trieste. After a general overlook of the setup, we provide an insight on peculiar features of the experimental apparatus. In particular, we present two alternative ways to perform a frequency-resolved measurement: the first one relying on a multi-channel detector and the second one employing a single channel low noise detector in combination with a pulse shaper. A description of the balanced configuration implemented and of the laser phase stabilization system completes the Chapter.

- In Chapter 3 we perform preliminary characterization studies of the multimode heterodyne detection measurements. In the first part of the Chapter we present the complete characterization of our set-up noise, which is crucial to test the quantum noise sensitivity of the technique and eventually select suitable experimental conditions to ensure a shot-noise limited detection. In the second part, we provide a rescaling procedure for the heterodyne traces acquired, in order to express the measured fields in photon units and perform quantitative estimations.

- Mean value outcomes of a time-resolved Multimode Heterodyne Detection experiment are presented in Chapter 4. In particular, we investigate the presence of coherent phonons in the probe spectral amplitude and phase dynamic response. We retrieve a different behavior for the two observables, that we explain with two different phenomena. Indeed, we point out that amplitude dynamics is ruled by Impulsive Stimulated Raman Scattering, while phase dynamics is determined by Linear Refractve Modulation. As a conclusion of the Chapter, we provide a theoretical picture that explains experimental evidences.

- In Chapter 5 we go beyond the mean value approach and perform a study of the pump second harmonic generation process based on quantum fluctuations of the measurements. In particular, we show that the interference between local oscillator and pump second harmonic gives rise to an incoherent superposition of quantum states characterized by a random phase. Moreover, we exploit the laser phase stabilization system to control this phase uncertainty and address its origin. In conclusion, we perform quantitative estimations by means of *Pattern Function Quantum Tomography.*

Chapter 1

Detection of light quantum states

Quantum Mechanics asserts that, if we know the state of a system combined with its evolution laws, we're able to predict any possible outcome of any possible measurement performed on it.

However, knowing the state of a system isn't an easy task to reach. In particular, to reconstruct the *quantum state*, we need to perform repeated measurements of a set of observables called *quorum* on equally prepared systems.

When we deal with light quantum state, the observables that have to be measured in order to retrieve complete information about the state are electric field amplitude and phase. Unfortunately, standard intensity measurements do not allow to perform a full state reconstruction, since phase information is lost.

In order to perform a phase-resolved measurement, we introduce the interferometric technique dubbed Balanced Heterodyne Detection. This technique, through the recombination of the beam under investigation (signal) with a strong classical one (local oscillator), provides a full reconstruction of the quadrature, a representative observable of the electric field.

In this Chapter, after a brief introduction on what measuring a quantum state means, we introduce Balanced Heterodyne Detection for a monochromatic wave. Moreover, we show the capability of this technique to perform measurements where classical noise is killed unveiling measurements quantum fluctuations. In conclusion, we provide an extension of the formalism to multimode electric fields.

1.1 Quantum state of a physical system

In this section we present a brief introduction on what measuring a quantum state means. We will exploit the concepts provided in this section as a benchmark framework for introducing the detection of quantum light systems.

"State means whatever information is required about a specific system, in addition to physical laws, in order to predict its behaviour in future experiments" is the way Fano uses to introduce the concept of quantum state in his review paper [1]. In order to discuss detection of quantum states, we first need to briefly recall some basic concepts.

In quantum mechanics, we represent the state of a quantum object by a normalized vector $|\Psi\rangle$. We call this state *pure state*. The vector $|\Psi\rangle$ belongs to a Hilbert-space $\mathcal{H}$, where all the possible states of the system are contained. If we know that the system is in the state $|\Psi\rangle$, we can retrieve the expectation value of a generic observable $\hat{O}$ just by computing:

$$\langle\hat{O}\rangle = \langle\Psi|\hat{O}|\Psi\rangle \tag{1.1}$$

We underline that, if the initial state and the Hamiltonian operator of the system are known, the previous formalism provides a complete description of the system, of its time evolution and of the properties of its observables [2].

Nonetheless, there are physical circumstances in which we are not able to know the state of the system $|\Psi\rangle$. For this reason, we have to adopt a more general formalism based on a statistical approach. This is the density matrix formalism.

In order to introduce this formalism, let us assume to have an ensemble of physical states equally prepared and to have statistical information about them, that is, to have a set of eigenstates $|\Psi_n\rangle$ in which the system stays with probabilities p_n. In this case, the mean value of a physical observable $\hat{O}$ becomes:

$$\langle\hat{O}\rangle = \sum_n p_n \langle\Psi_n|\hat{O}|\Psi_n\rangle \tag{1.2}$$

Therefore, the statistic state of a quantum system can be defined as a linear combination of the states $|\Psi_n\rangle$ weighted on the corresponding probabilities p_n.

All the previous information can be gathered in just one operator $\hat{\rho}$, called density operator, which is the weighted average over the projectors of the states $|\Psi_n\rangle$:

$$\langle\hat{\rho}\rangle = \sum_n p_n |\Psi_n\rangle\langle\Psi_n| \tag{1.3}$$

In this statistical framework, the mean value of a physical observable can be expressed in terms of the density operator as follows:

$$\langle\hat{O}\rangle = \sum_n p_n \langle\Psi_n|\hat{O}|\Psi_n\rangle = \sum_m \sum_n p_n \langle\Psi_n|\hat{O}|\Psi_m\rangle\langle\Psi_m|\Psi_n\rangle = Tr[\hat{\rho}\hat{O}] \tag{1.4}$$

where $Tr[\hat{\rho}\hat{O}]$ is the trace[1] of $\hat{\rho}\hat{O}$.

The set of the matrix elements of the operator $\hat{\rho}$ on whatever basis is called density matrix and plays a crucial role in the statistical description of a quantum state. As a matter of fact, the probability of any outcome of any measurement performed on a system can be extracted from the density matrix of that system [3]. In particular, the diagonal elements ρ_{nn} represent the probability of the system to be in the eigenstate $|\Psi_n\rangle$, while the off-diagonal elements ρ_{mn} provide the coherence between the state $|\Psi_n\rangle$ and $|\Psi_m\rangle$. This means that ρ_{mn} is different from zero only if the system is in a coherent superposition of the eigenstates $|\Psi_n\rangle$ and $|\Psi_m\rangle$ [4].

[1] We recall that the trace of an operator is the sum of its diagonal matrix elements in any matrix representation

Therefore, all the information needed to perform statistical previsions on a quantum system are encoded inside the density matrix. By its elements ρ_{ij} we are hence able to predict the outcomes of any measurement performed on the system.

We stress that, while the state of a classical system can be determined by performing repeated measurements on it, the knowledge of a quantum state is not accessible, in general, when a single copy of the system itself is available. In fact, the act of measuring an observable of the system changes its state, making repeated measurements on it meaningless towards the determination of its initial state [3]. Therefore, statistical previsions on a quantum system are only possible when an ensemble of identically prepared systems is available.

As proved in [1], in order to fully reconstruct the density matrix, it is necessary to measure a set, called quorom, of at least two non-commuting observables $\hat{O}_i$. The previous statement has a direct implication on the measurement of optical quantum state. Indeed, it implies that no complete statistical information on an optical field can be retrieved if we limit in measuring only its intensity. This holds because intensity is related to the amplitude of the electric field, but encodes no information about the phase, that is the other observable characterizing the system. Therefore, to have access to a meaningful statistics, a phase-resolved approach has to be implemented. This is provided by Balanced Heterodyne Detection.

1.2 Balanced Heterodyne Detection

In the previous section we have pointed out the necessity of having access to the statistics of at least two non-commuting observables in order to perform statistical previsions of any measurement on a quantum state. In the quantum optics framework, this requirement implies the necessity of having access to phase dynamics, which cannot be unveiled in standard intensity measurements. In this section we will present an interferometric technique, named Balanced Heterodyne Detection, able to accomplish this requirement. We will preliminary study this approach in the case in which the optical state under investigation is a single electromagnetic field mode of the form [4]:

$$\hat{E}_j(z,t) = i\sqrt{\frac{\omega_j}{2\epsilon_0 V}}\left[\hat{a}_j e^{-i(\omega_j t - k_j z)} - \hat{a}_j^\dagger e^{i(\omega_j t - k_j z)}\right] \tag{1.5}$$

where $\hat{a}_j$ and $\hat{a}_j^\dagger$ are the ladder operators of the quantum-harmonic oscillator satisfying the commutation relation:

$$[\hat{a}_j^\dagger, \hat{a}_k] = \delta_{jk} \tag{1.6}$$

The expression of the quantized electromagnetic field can be written in terms of the adimensional quantum harmonic oscillator position

$$\hat{Q}_j = \frac{1}{2}(\hat{a}_j^\dagger + \hat{a}_j) \tag{1.7}$$

and momentum

$$\hat{P}_j = \frac{i}{2}(\hat{a}_j^\dagger - \hat{a}_j) \tag{1.8}$$

resulting in

$$\hat{E}_j(z,t) = \sqrt{\frac{\omega_j}{2\epsilon_0 V}}\left[\hat{Q}_j cos(\phi_j) + \hat{P}_j sin(\phi_j)\right] \tag{1.9}$$

where we have defined the phase as $\phi_j = \omega_j t - k_j z + \pi/2$. If we now define the phase-dependent operator $\hat{X}_{\phi_j}$ as:

$$\hat{X}_{\phi_j} = \frac{1}{\sqrt{2}}\left(\hat{a}_j e^{-i\phi_j} + \hat{a}_j^\dagger e^{i\phi_j}\right) \tag{1.10}$$

the quantized electromagnetic field can be expressed as:

$$\hat{E}_j(z,t) = \sqrt{\frac{\omega_j}{\epsilon_0 V}}\hat{X}_{\phi_j} \tag{1.11}$$

$\hat{X}_{\phi_j}$ is dubbed quadrature operator, it is proportional to the quantized electric field and we will see that it is the detected observable in a Balanced Heterodyne experiment, whose main features will be highlighted in the following.

Balanced Heterodyne Detection is a powerful method for measuring phase-sensitive properties of travelling optical fields that is used for the reconstruction of quantum light states [3]. In this framework, the quantum state is characterized through the repeated measurements of the optical field quadratures $\hat{X}_{\phi_j}$ (equation 1.10) for different phases $\phi_j \in [0, 2\pi]$.

Quadratures at fixed phase ϕ_j are continuum-spectrum observables and constitute a quorum of observables, whose measurement hence provides a complete information about the quantum state of the electromagnetic field [5]. The schematic diagram employed in Balanced Heterodyne Detection is depicted in figure 1.1.

The optical state under investigation, named signal, is mixed with a strong classical reference state, named local oscillator (LO), by a 50:50 beam spitter (whence the attribute balanced).

Since the signal beam (mode $\hat{a}$ in figure 1.1) can be prepared in an unknown way, it can be conveniently described in a statistical way by mean of the density operator $\hat{\rho}$ (equation 1.3). The

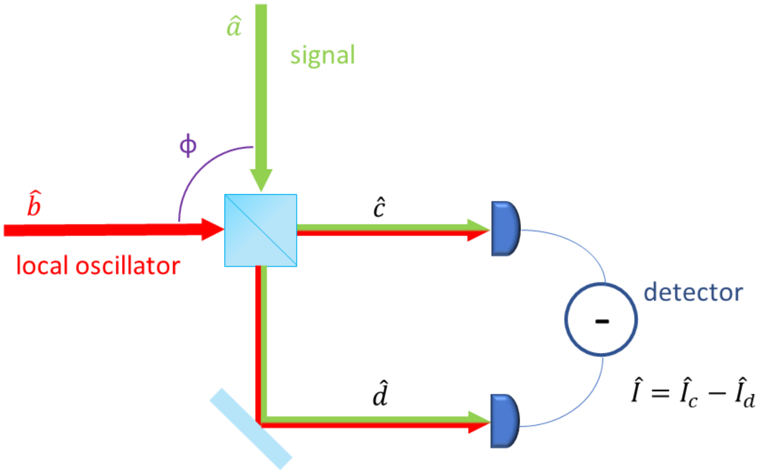

Figure 1.1: scheme of a Balanced Heterodyne Detection setup. The beam under investigation, typically named *signal*, interferes with a strong classical beam, dubbed *local oscillator* in a 50:50 beam splitter. The resulting beams are acquired and the differential photon current is measured. It can be proved that differential photon current is proportional to the quadrature of the signal electric field.

local oscillator (mode $\hat{b}$ of figure 1.1) is instead in a classical coherent state[2] $|z\rangle\langle z|$. Therefore, it satisfies:

$$\hat{b}|z\rangle = z|z\rangle \quad z \in \mathbb{C} \tag{1.12}$$

The beam splitter outputs in the mode states $\hat{c}$ and $\hat{d}$ are collected by two photodiodes and the differential photon current $\hat{I}$ (heterodyne current) is measured. The modes $\hat{c}$ and $\hat{d}$ are linked to the incoming modes $\hat{a}$ and $\hat{b}$ by mean of the balanced beam splitter, whose action is ruled by the unitary operator (see section 1.3):

$$\hat{U}_{BS} = \frac{1}{\sqrt{2}} \begin{pmatrix} 1 & 1 \\ -1 & 1 \end{pmatrix} \tag{1.13}$$

Therefore, as a consequence of $\hat{U}_{BS}$ action, we get:

$$\begin{cases} \hat{a} & \rightarrow \quad \hat{c} = \dfrac{\hat{a} + \hat{b}}{\sqrt{2}} \\ \hat{b} & \rightarrow \quad \hat{d} = \dfrac{\hat{b} - \hat{a}}{\sqrt{2}} \end{cases} \tag{1.14}$$

After the 50:50 BS, the two modes are detected by two identical photodiodes and the respective photon currents ($\hat{I}_c$ and $\hat{I}_d$) are measured and subtracted.

The currents $\hat{I}_c$ and $\hat{I}_d$ (figure 1.1) are the measured values of the photon number observables $\hat{n}_c = \hat{c}^\dagger \hat{c}$ and $\hat{n}_d = \hat{d}^\dagger \hat{d}$. Therefore, the differential photon current $\hat{I}$ reads:

$$\hat{I} = \hat{n}_c - \hat{n}_d = \hat{c}^\dagger \hat{c} - \hat{d}^\dagger \hat{d} \tag{1.15}$$

which, exploiting the beam spitter transformation rules (equation 1.14), becomes:

$$\hat{I} = \hat{a}^\dagger \hat{b} + \hat{b}^\dagger \hat{a} \tag{1.16}$$

[2]Coherent states are the eigenstates of the annihilation operator $\hat{a}$ of the harmonic oscillator. They are used in quantum optics to represent classical states, since the mean evolution of the canonical operators ($\hat{p}$ and $\hat{q}$) on those states is the same as the classical one.

The phase-sensitivity of the technique is achieved by tuning the phase difference between the local oscillator and the signal, which can be controlled by changing the length of the LO optical path. This implies that the LO mode is subjected to the following phase shift:

$$\begin{cases} \hat{b} \quad \rightarrow \quad \hat{b}\, e^{i\phi} \\ \hat{b}^{\dagger} \quad \rightarrow \quad \hat{b}^{\dagger} e^{-i\phi} \end{cases} \tag{1.17}$$

and the heterodyne current operator can be subsequently redefined as:

$$\hat{I}_{\phi} = \hat{a}^{\dagger}\hat{b}e^{i\phi} + \hat{b}^{\dagger}\hat{a}e^{-i\phi} \tag{1.18}$$

Now, a natural question arises: how, by measuring the phase-resolved heterodyne current $\hat{I}_{\phi}$, can we obtain a value for the quadrature of the electric field? The answer comes from the fact that the expectation value of the heterodyne current $\langle \hat{I}_{\phi} \rangle$ on the total LO-signal input state $\hat{\rho} \otimes |z\rangle\langle z|$ is proportional to the expectation value of the field quadrature $\hat{X}_{\phi}$ defined in equation 1.11:

$$\langle \hat{I}_{\phi} \rangle = Tr\Big[\hat{\rho} \otimes |z\rangle\langle z|\hat{I}_{\phi}\Big] = Tr\Big[\hat{\rho} \otimes |z\rangle\langle z|(\hat{a}^{\dagger}\hat{b}e^{i\phi} + \hat{b}^{\dagger}\hat{a}e^{-i\phi})\Big] = \sqrt{2}|z|\langle \hat{X}_{\phi} \rangle \tag{1.19}$$

We underline that to write equation 1.19 we neglect the phase of the initial local oscillator coherent state, i.e. $z = |z|$ (equation 1.12).

By means of balanced heterodyne detection we can therefore measure the quadrature of the signal field amplified by the local oscillator. Indeed, the detected heterodyne current scales linearly with the LO amplitude $|z|$.

We underline that, in order to ensure the heterodyne current to be a representative observable of the field quadrature at each phase, it's not sufficient that their expectation values coincide. Indeed, all higher order momenta of the two observables must coincide. For the second order momentum we get the following expression [5]:

$$\langle \hat{I}_{\phi}^{2} \rangle = \frac{1}{2|z|^{2}} Tr\Big[\hat{\rho} \otimes |z\rangle\langle z|(\hat{a}^{\dagger}\hat{b}e^{i\phi} + \hat{b}^{\dagger}\hat{a}e^{-i\phi})^{2}\Big] = \langle \hat{X}_{\phi}^{2} \rangle + \langle \frac{\hat{a}^{\dagger}\hat{a}}{2|z|^{2}} \rangle \tag{1.20}$$

We notice that the heterodyne current second order momentum tends to the quadrature one only if $2|z| >> \hat{a}^{\dagger}\hat{a}$. Therefore, we can extract meaningful statistical information on the quantum signal field through Balanced Heterodyne Detection only if we mix it with a much more intense classical field (the local oscillator). This situation can be hence referred to as quantum regime of the interferometer, opposed to the classical one in which the signal field is in a large-amplitude coherent state $|\alpha\rangle$:

$$\hat{a}|\alpha\rangle = \alpha|\alpha\rangle \quad \alpha \in \mathbb{C} \tag{1.21}$$

In the latter case only mean values coincide and classical interference pattern can be retrieved. If the signal field is classical ($2|z| \sim \hat{a}^{\dagger}\hat{a} = 2|\alpha| >> 1$) we have indeed[3]:

$$\langle \hat{X}_{\phi} \rangle = Tr\big[\hat{X}_{\phi}|\alpha\rangle\langle\alpha|\big] = \langle\alpha|\frac{\hat{a}e^{-i\phi} + \hat{a}^{\dagger}e^{i\phi}}{2}|\alpha\rangle = \sqrt{2}|\alpha|cos(\phi) \tag{1.22}$$

which implies:

$$\langle \hat{I}_{\phi} \rangle = 2|z||\alpha|cos(\phi) \tag{1.23}$$

In conclusion, we have shown (equation 1.34) that a requirement for Balanced Heterodyne Detection to be sensitive on quantum fluctuations of the signal quadrature is to work with a local oscillator in a strong classical state.

A natural question therefore arises: how can we filter out LO classical noise and ensure a quantum noise sensitiviy? In the following section we will analyse this issue and prove that balanced configuration[4] plays a crucial role in ensuring quantum sensitivity.

[3] we have neglected the phase of the signal coherent state, i.e. $\alpha = |\alpha|$.

[4] i.e. a configuration where the recombining beam splitter is 50:50.

1.3 Quantum noise sensitivity

The crucial element on which quantum noise sensitivity relies is the last beam splitter before the differential detection (figure 1.1).

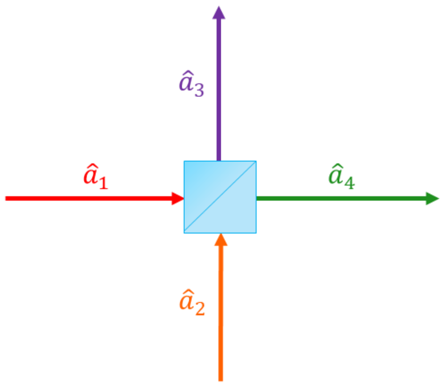

Figure 1.2: scheme of a lossless beam splitter. In a quantum formalism, the second entrance $\hat{n}_2$ must always be present, even if the signal channel is blocked. In this case, $\hat{n}_2$ is described by the vacuum state $|0\rangle$

A beam splitter is a dielectric medium able to split a beam into two with a defined proportion [6]. A representation of a lossless beam splitter is depicted in figure 1.2, in which two beams, that we will indicate with their annihilation operators $\hat{a}_1$ and $\hat{a}_2$, impinge on it and two other beams, $\hat{a}_3$ and $\hat{a}_4$, emerge from it. We can write the relation between the input and the output states as:

$$\begin{aligned} \hat{a}_3 &= R\hat{a}_1 + T\hat{a}_2 \\ \hat{a}_4 &= T\hat{a}_1 + R\hat{a}_2 \end{aligned} \tag{1.24}$$

where R and T represent the complex reflectivity and transmittance of the beam splitter: $R = |R|e^{i\phi_R}$, $T = |T|e^{i\phi_T}$. In order to ensure photon number conservation the following relations must hold between the BS parameters:

$$\begin{aligned} |R|^2 + |T|^2 &= 1 \\ R^*T + T^*R &= 0 \end{aligned} \tag{1.25}$$

As a consequence of equation 1.24, the output photon number operators are related to input ones by the relations:

$$\begin{aligned} \hat{n}_3 = \hat{a}_3^\dagger\hat{a}_3 = |R|^2\hat{a}_1^\dagger\hat{a}_1 + |T|^2\hat{a}_2^\dagger\hat{a}_2 + R^*T\hat{a}_1^\dagger\hat{a}_2 + T^*R\hat{a}_2^\dagger\hat{a}_1 \\ \hat{n}_4 = \hat{a}_4^\dagger\hat{a}_4 = |T|^2\hat{a}_1^\dagger\hat{a}_1 + |R|^2\hat{a}_2^\dagger\hat{a}_2 + T^*R\hat{a}_1^\dagger\hat{a}_2 + R^*T\hat{a}_2^\dagger\hat{a}_1 \end{aligned} \tag{1.26}$$

From the expressions of the number operators (equation 1.26) we can retrieve for each output the mean number of photons and the related variance. The expressions for the mean photon number of the two outputs are:

$$\begin{aligned} \langle\hat{n}_3\rangle &= |R|^2\langle\hat{n}_1\rangle + |T|^2\langle\hat{n}_2\rangle \\ \langle\hat{n}_4\rangle &= |T|^2\langle\hat{n}_1\rangle + |R|^2\langle\hat{n}_2\rangle \end{aligned} \tag{1.27}$$

The same calculation can be done for the related variances. In order to simplify the notation, we will only consider the case in which $\hat{n}_2$ is in a vacuum state $|0\rangle$. In this situation, the expressions of the variances of the two output beams read:

$$
\begin{aligned}
\sigma_3^2 &= |R|^4\sigma_1^2 + |R|^2|T|^2\langle\hat{n}_1\rangle \\
\sigma_4^2 &= |T|^4\sigma_1^2 + |R|^2|T|^2\langle\hat{n}_1\rangle
\end{aligned}
\tag{1.28}
$$

We can recognize that the variances of both channels have two contributions [6] (figure 1.3):

- Classical noise: it is proportional to the input noise σ_1^2 of the only physical beam impinging on the BS and it is related to the intensity of the reflected/transmitted beam.
- Quantum (partition) noise: it is caused by the random division of the input photons in the two channels with probabilities $|R|^2$ and $|T|^2$. Therefore it pertains to the intrinsic quantum nature of the electromagnetic field.

Figure 1.3: every beam exiting from a beam splitter presents two noise contributions: a classical one, related to the beam intensity, and a quantum one, determined by the random division of photons that ovvurs on the beam splitter.

Let us now exploit the beam splitter formalism to retrieve mean value and noise information on the heterodyne current, which is the observable in our experiment (figure 1.1).

For the fluctuations, we will limit to the second order momentum (variance), thus neglecting the information encoded in higher order momenta. With the notation of figure 1.2, mean value and variance of the heterodyne current $\hat{n}_3 - \hat{n}_4$ can be expressed as follows:

$$
\langle\hat{n}_{3-4}\rangle = \langle\hat{n}_3 - \hat{n}_4\rangle = \Big(|R|^2 - |T|^2\Big)\langle\hat{n}_1\rangle \tag{1.29}
$$

$$
\sigma_{3-4}^2 = \langle(\hat{n}_3 - \hat{n}_4)^2\rangle - \langle\hat{n}_3 - \hat{n}_4\rangle^2 = \Big(|R|^2 - |T|^2\Big)\sigma_1^2 + 4|R|^2|T|^2\langle\hat{n}_1\rangle \tag{1.30}
$$

From the previous equations we can immediately recognize that, by working in balanced conditions[5], the classical noise can be filtered out from the differential response. As a matter of fact, we get:

$$
\sigma_{3-4}^2 = \langle\hat{n}_1\rangle \tag{1.31}
$$

We underline that, in the heterodyne framework (figure 1.1), these fluctuations come from the vacuum fluctuations of the signal encoded inside the partition noise of the local oscillator. Some characterizations of this noise are performed in Chapter 3.

[5] i.e. by setting $|R|^2 = |T|^2 = 1/2$

1.4 Generalization to multimode quantum states

The single mode description provided in the previous section has to be generalized when ultrashort laser pulses are used. Indeed, owing to the Heisenberg uncertainty principle, to a short pulse duration corresponds a broad spectrum of frequency modes of the radiation. In the following we introduce multimode light states and show that we can generalize single mode heterodyne formalism to multimode quantum states.

For pulsed laser sources, as the ones used for the experiments in this thesis, we can't approximate the emitted light as monochromatic, since the short duration of the pulse in time is necessarily followed by a certain broadening in frequency.

Quantized pulsed laser light is described by associating to each monochromatic component a coherent state $|\alpha_j\rangle$, that is an eigenstate of the annihilation operator $\hat{a_j}$ of photons in the mode of frequency ω_j:

$$\hat{a_j}|\alpha_j\rangle = \alpha_j|\alpha_j\rangle$$

The entire pulse, consisting in a superposition of N different modes, is then described by the tensor product:

$$|\alpha_1\rangle \otimes |\alpha_2\rangle \otimes ... \otimes |\alpha_j\rangle \otimes ...|\alpha_N\rangle$$

For monochromatic light, we showed that heterodyne differential current reads:

$$\hat{I}_\phi = \hat{a}^\dagger \hat{b} e^{i\phi} + \hat{b}^\dagger \hat{a} e^{-i\phi}$$

If more frequencies ω_j are present both in the LO and in the signal[6], each one of the corresponding mode operators will be subjected to the beam splitting transformation (equation 1.24) and the detectors will ideally register photons of all involved frequencies[7]. Then, the photon current operator becomes:

$$\hat{I}_\phi = \sum_j \hat{a}_j^\dagger \hat{b_j} e^{i\phi_j} + \hat{b_j}^\dagger \hat{a_j} e^{-i\phi_j} \tag{1.32}$$

We underline that no contribution derives from mixed frequency terms, i.e. interference occurs only between modes of the same frequency [7]. Consequently, the mean multimode current is (cfr equation 1.19):

$$\langle \hat{I}_\phi \rangle = \sqrt{2} \sum_j |z_j| \langle \hat{X}_{\phi_j} \rangle \tag{1.33}$$

Similarly, the second order momentum of the differential photon current is:

$$\langle \hat{I}_\phi^2 \rangle = \langle \hat{X}_\phi^2 \rangle + \sum_j \langle \frac{\hat{a}_j^\dagger \hat{a}_j}{2|z_j|^2} \rangle \tag{1.34}$$

Therefore, current and quadrature second order momenta match only in the case of quantum regime[8]. As a final remark, notice that, in the case of only one frequency mode, the above treatment reduces to the single mode one.

[6] i.e. both LO and signal are described by multimode states

[7] The multimode acquisition setup is described in Chapter 2

[8] i.e. when $2|z_j| >> \hat{a}_j^\dagger \hat{a}_j$

Chapter 2

Experimental setup

To study low energy excitations dynamics, the standard measurement performed is the pump and probe one.It consists in impinging on the sample with two consecutive pulses: the pump pulse, to excite the system, and the probe one, to investigate it. Typically, the detection system acquires probe intensity, retrieving its electric field amplitude. However, we showed in Chapter 1 that, in order to reconstruct completely the light quantum state, we need to measure also the electric field phase. This requirement is fulfilled by the interferometric technique called Balanced Heterodyne Detection.

In this Chapter we describe the experimental realization of a setup that performs the heterodyne detection of the probe pulse. We underline that combining pump and probe technique with Balanced Heterodyne Detection is a very powerful tool, since it allows us to study separately the amplitude and phase dynamic response of the electric field.

Anyway, these aren't the only parameters under our control. Indeed, we exploit the ultrashort time duration of the probe pulse ($< 50\ fs$) to perform a frequency resolved measurement. As we'll see, the way we achieve this goal changes depending on the detection system used.

In particular, to detect the heterodyne trace we adopt two different configurations characterized by a different signal to noise ratio: the first one uses two arrays of photodiodes while the second one employs a differential low noise detector in combination with a pulse shaper. In both cases the acquisition is performed pulse by pulse, giving us access to the statistical degrees of freedom of the measurement (some results are presented in Chapter 5).

In the following, the description of the setup and some focuses on peculiar parts of the experimental apparatus. In particular, we provide an accurate description of the pulse shaper, the balanced configuration, the detectors and the laser phase stabilization system.

2.1 Setup

Our experimental setup takes origin from the necessity of extracting as much information as possible from the widespread pump and probe technique (P&P). In these kind of experiments a first pulse (pump) impinges on the sample to excite it and then, after a well defined time delay, a second pulse (probe) interacts with the excited system. The typical information obtained from a P&P experiment is the intensity of the probe electric field for different time delays. Since intensity can be linked to sample properties like reflectivity [6], transmittance, etc, looking at modifications in probe intensity returns information about excitation dynamics.

However, because of the wave nature of the electromagnetic radiation, the electric field is characterized also by a phase, that in principle can encode different information and so unveil additional features of the system studied. In order to achieve a phase sensitive P&P measurement, we implement in the setup the heterodyne detection of the probe pulse. A simplified scheme is presented in figure 2.1.

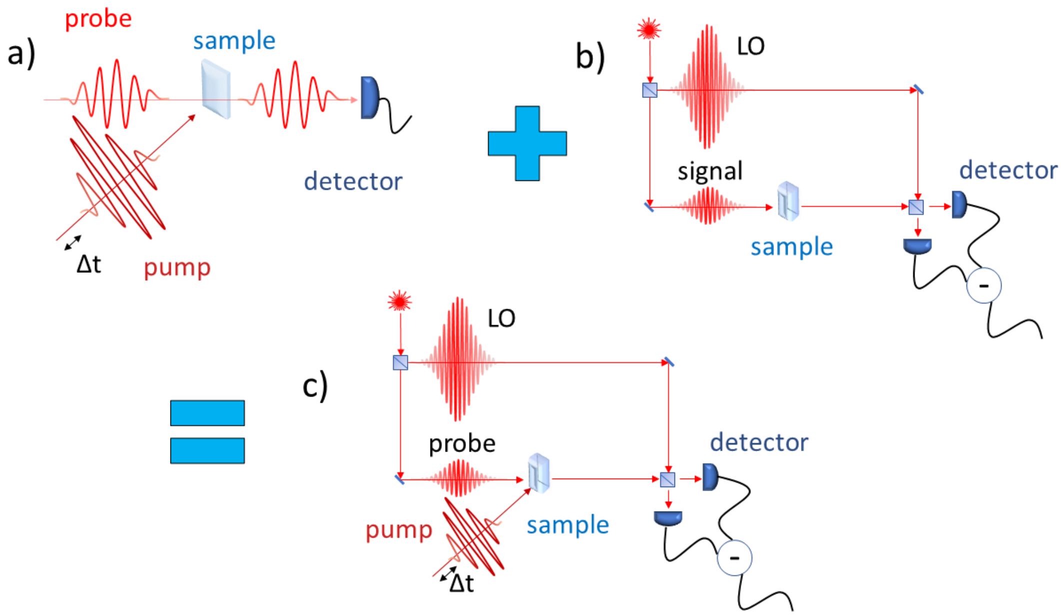

Figure 2.1: The combination of the pump and probe technique (a) with heterodyne detection (b) allows us to perform a pump and probe phase sensitive experiment. A simplified scheme of the heterodyne detection of the probe is shown in (c).

The initial beam is divided in two parts, typically named signal and local oscillator (LO), by means of a beam splitter. The signal, playing the role of the probe, impinges on the sample previously excited by a pump pulse and then is recombined with the local oscillator that acts as a reference beam. The recombination is performed by a 50:50 beam splitter. We finally detect the two outcoming beams and measure the differential photon current, that is proportional to the quadrature field (equation 1.19). By tuning the relative phase between LO and signal, we can reconstruct the quadrature oscillation and hence perform a phase sensitive pump and probe experiment.

We adopt a *balanced* heterodyne configuration, i.e. we use a 50:50 beam splitter to recombine signal and local oscillator. As we proved in section 1.2, employing a balanced configuration allows us to drastically reduce the extrinsic classical noise and to measure the intrinsic quantum fluctuations of the photon number. This enables us to reach the best signal-to-noise ratio.

2.1.1 Multimode Heterodyne Detection

As a consequence of the Heisenberg uncertainty principle, ultrashort light pulses have a broad spectral content and this enables the possibility of performing a frequency-resolved measurement. In the following, we present two configurations that perform a Multimode Heterodyne Detection experiment (figure 2.2).

The most immediate way to achieve this goal is by dispersing the beams exiting from the final beam splitter with a prism. Subsequently, we detect the pulse dispersed spectral components with a multi-channel detector (figure 2.2a) consisting of two photodiodes arrays (see section 2.4). In figure 2.2a we present the scheme of the configuration with an example of quadrature map acquired. The map presents the phases of the quadrature field along the horizontal axis and the different pulse frequencies along the vertical axis. We underline that we obtain a quadrature map for each pump-probe time delay.

However, this isn't the only possible configuration to perform Multimode Heterodyne Detection. In particular, we're interested in performing this measurement with a low noise single channel detector[1]. Even with this limitation, a frequency resolved measurement can be performed with the employment of a pulse shaper (figure 2.2b).

A pulse shaper is a tool that controls amplitude and phase of each pulse spectral component independently (more details in section 2.2). We use this device to modulate the local oscillator and obtain a spectrally narrow band pulse, centered on a selected mode. A scan through different LO modes, thanks to the probe amplification (equation 1.19), allows us to selectively measure different frequencies of the emitted probe and hence to perform a frequency-resolved measurement (figure 2.2b). We underline that also in this case the outcome of a measurement is a quadrature map (figure 2.2b).

The reader may notice that in this setup (figure 2.2b) both the probe and the LO oscillator are sent to the pulse shaper, even if Multimode Heterodyne Detection necessities the shaping of just the latter. This solution is adopted to employ the same optical elements for the two beams and so to improve the stability of the interferometer.

Since we employ both a single channel (differential detector) and a multi channel (photodiodes arrays) detection system, we implement in our experimental setup both the configurations described. We can easily switch between the two removing/inserting a mirror.

We underline that with this technique we're able to resolve the measurement in the time domain and in the frequency domain independently. This is possible because the time measurement is performed on the sample while the frequency one happens on the detector, and therefore we're not violating the Heisenberg uncertainty principle.

[1] The reason why in this case we cannot adopt the first configuration is that dispersing the final beam on a single channel detector would provide just a measurement of a single mode.

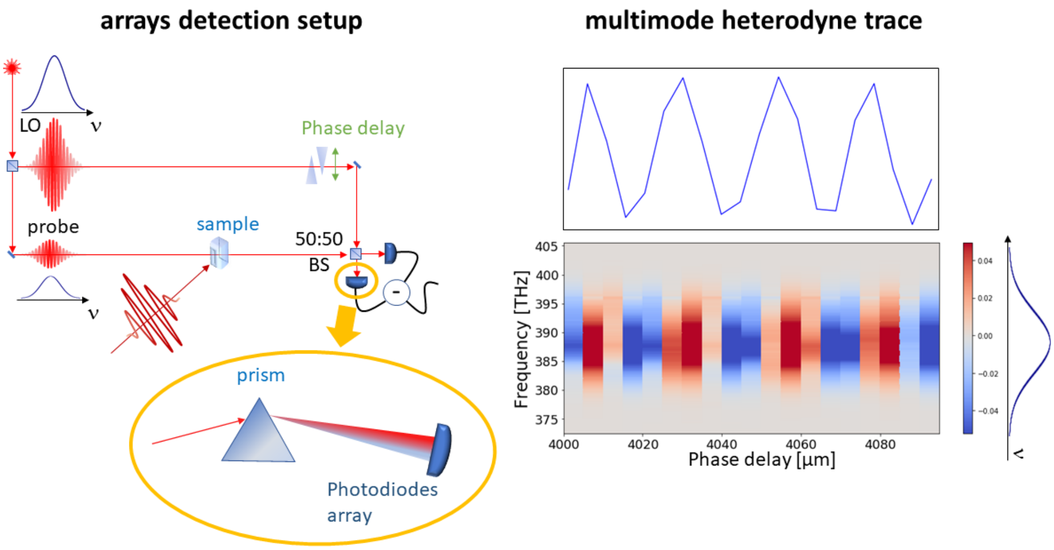

(a) Multimode setup for a multi-channel detector

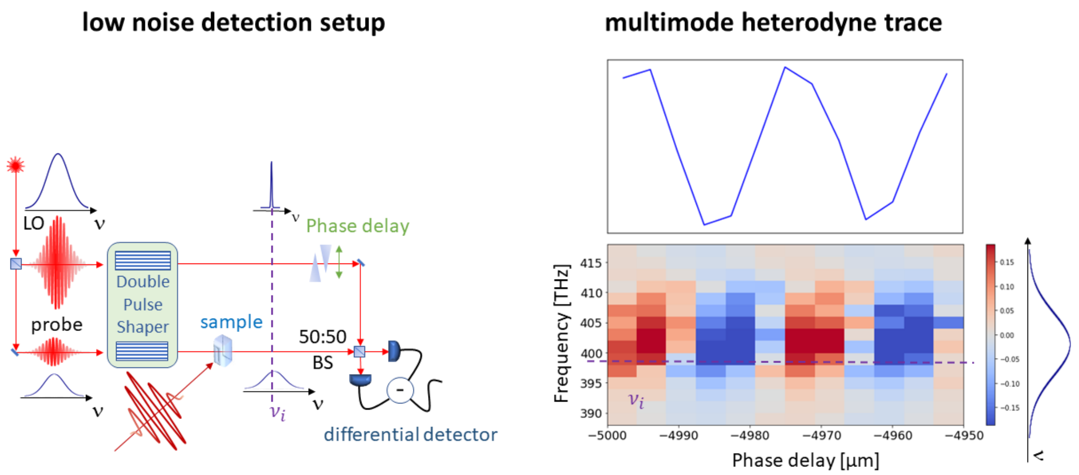

(b) Multimode setup for a single channel detector

Figure 2.2: we present two different configurations for a Multimode Heterodyne Detection setup. In (a) the final beams are spectrally dispersed and sent to a multi-channel detector (that in our case consists in a pair of photodiodes arrays). The other option (b) uses a single channel detector and necessities the employment of a pulse shaper to measure on mode at a time. Both methods produce a quadrature map for every pump delay.

Setup technical specification

P&P pulses are produced by a commercial 200 kHz pulsed laser + optical parametric amplifier (OPA) system (Pharos + Orpheus-F, Light Conversion). The signal produced by the OPA, used as the probe and the heterodyning field in the interferometer, has a time duration $< 50\ fs$ and a tunable wavelength in the range of $650 - 950\ nm$. The idler is used as the pump and has a duration $< 50\ fs$ and its wavelength resides in the near-infrared. The measurements reported in this thesis are performed at a reduced[2] repetition rate of 1 kHz with a probe wavelength of 745 nm and a pump one of 1640 nm.

The relative phase between the probe and the local oscillator is controlled by mean of a wedge pair mounted on a piezoelectric translator, whereas the pump delay line lies on a mechanical translation stage.

Since we want to isolate from the heterodyne current purely dynamical features imprinted on the equilibrium response (i.e. without the pump), we have inserted a chopper along the pump beam. Indeed, by chopping the pump beam at a frequency (500 Hz) that is half the laser repetition rate and by triggering the pump arrival by mean of a diode, both the pumped and the equilibrium quadrature can be measured at every delay. The difference between these two quadratures encodes the pump-dependent dynamics of the probe. Moreover, by chopping the pump, we can eliminate from the heterodyne current noises slower than the chopping rate (500 Hz).

A detailed representation of the setup is shown in figure 2.3. Lenses and polarizing elements are omitted. Even if they're not shown in figure 2.3, polarizing elements ($\lambda/2$ and polarizers) are present along the probe and the pump paths to independently control their polarizations.

We underline that figure 2.3 scheme is valid for both Multimode Heterodyne Detection configurations previously described (figure 2.2). LO and probe are always sent to the pulse shaper: depending on the configuration, pulse shaper will be used to shape the pulse spectral content (figure 2.2b) or simply as a mirror (figure 2.2a).

In the measurements presented in Chapter 5 we adopt a slightly different configuration, where the incident pump is collinear with the probe beam. This choice is made to perform Multimode Heterodyne Detection of the pump, and in particular of its second harmonic.

[2] We have to work with a reduced repetition rate in order to overcome detection system limitations and perform a shot by shot pulse acquisition.

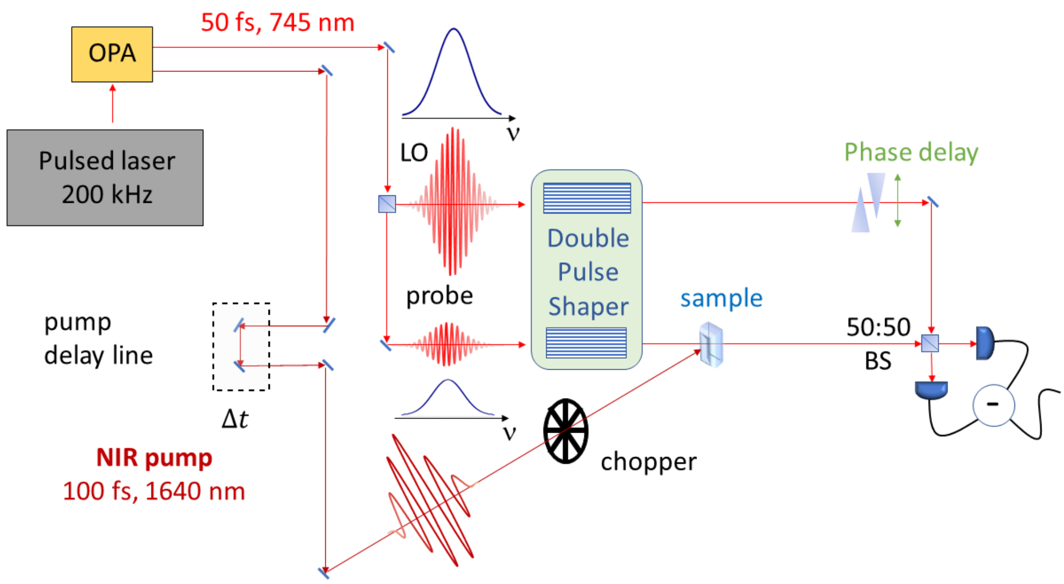

Figure 2.3: a schematic representation of the setup is presented. A laser + OPA system produces a signal with a wavelength of 745 nm and an idler, used as a pump, of 1640 nm. By means of a beam splitter, the signal is divided in two parts, the local oscillator and the probe. Both impinge on a pulse shaper: depending on the multimode configuration selected, the LO will be modulated or not. After the interaction with the sample, previously excited with the pump pulse, the probe is recombined with the LO in a 50:50 beam splitter and finally the differential photon current of the two outputs is measured. This current can be acquired for every pump-probe delay (controlled by a mechanical translation stage), every relative phase between probe and LO (using a movable wedge) and every pulse frequency. Reference quadratures of the equilibrium system are acquired for every point by means of a chopper.

2.2 Pulse shaping for frequency resolving a single channel detector heterodyne measurement

In section 2.1 we've seen that Multimode Heterodyne Detection can be performed in two different ways. The first one consists in spatially dispersing final beams in order to measure, with a multi channel detector, the various spectral components. However, this configuration is limited to multi channel detectors. Since we're interested in employing a single channel low noise detector for fluctuation studies (Chapter 5), we need a second method to perform a measurement frequency resolved.

For this purpose we developed a pulse shaper, that is a tool able to independently control the spectral amplitude and phase of each pulse component. In particular we use a commercial 2D Liquid Crystal Spatial Light Modulator (SLM), whose features we'll be discussed in the following paragraphs after an overlook of ultrafast pulse shaping principles.

2.2.1 Ultrafast Pulse-Shaping

With ultrafast pulse shaping we refer to all the techniques able to manipulate femtosecond pulses in both their amplitude and phase content. Here we will only discuss pulse shaping involving the spatial masking of the spatially dispersed pulse frequency spectrum. This is a widely employed approach that enables an independent control of the phase and the amplitude of each dispersed spectral component.

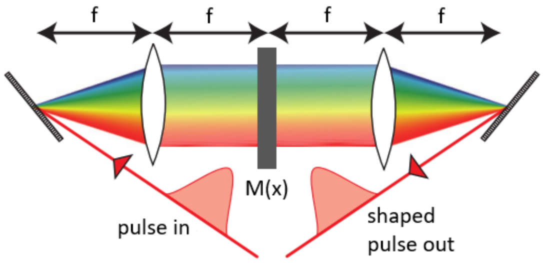

Figure 2.4: scheme of a 4f line pulse shaper. This configuration consists of a pair of diffraction gratings and cylindrical lenses equally spaced by the focal length *f*. Placing a mask between the two lenses enables an arbitrary control of the phase and the amplitude of the spectral components.

The most basic pulse-shaper adopting spatial masking is depicted in Figure 2.4 and it's commonly called *4f-line*. It consists of a pair of diffraction gratings and cylindrical lenses, arranged so that they are equally spaced by a distance *f*, corresponding to the focal length of the lenses. The frequency components within the incoming pulse are angularly dispersed by the first grating and are then focused by the first lens at its Fourier plane. By placing a spatial mask $M(x)$ in the Fourier plane we are able to selectively act on the dispersed frequency components and thus transfer a precise amplitude and phase pattern from the mask to the pulse spectrum. After the spatial shaping, a second pair lens-grating recombines the dispersed light, so that the final output is a shaped collimated beam.

The simplest type of mask is the static one, which performs a well defined shaping that can't be changed. However, to perform Multimode Heterodyne Detection with a signle channel detector, a scan of the LO frequencies is required and therefore we're interested in a more flexible tool. This task is accomplished by a Liquid Crystal Spatial Light Modulator (SLM), i.e. a programmable mask that enables dynamic changes of the pulse shaping features.

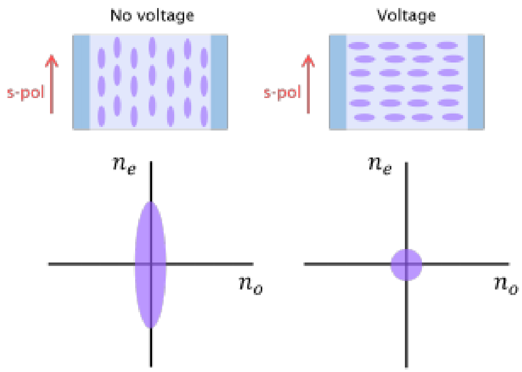

Figure 2.5: section of an SLM pixel. When a voltage is applied, the orientation of the liquid crystals changes determining different birifrangence conditions. Therefore a control of the orientation determines a control of the impinging beam optical path.

2.2.2 Two dimensional Liquid Crystal Spatial Light Modulator

An SLM is a pulse shaper that exploits the birefringent properties of liquid crystals to dynamically control the optical path (and hence the phase) of the light impinging on it. It consists of a pair of electrodes with a thin layer of nematic[3] liquid crystals placed between them in such a way that their director is parallel to the substrates when no voltage is applied between them [8].

Phase modulation

As shown in figure 2.5, if the incoming beam is linearly polarized along the direction parallel to the (no voltage) director of the liquid crystals, it experiences two distinct situations according to whether or not a voltage is applied between the electrodes. When no voltage is applied, the beam experiences the maximum difference between the extraordinary (n_e) and the ordinary (n_o) refractive index. On the contrary, when a voltage is applied, the molecules of the liquid crystal realign along the electric field that has been established. In this configuration, the impinging pulse experiences no difference between the two refractive indices along the two directions (figure 2.5).

Moreover, the SLM acts as a waveplate which is responsible for a voltage-dependent phase delay Φ equal to:

$$\Phi(V, \omega) = \frac{\omega \Delta n(V, \omega) d}{c} \tag{2.1}$$

where V is the applied voltage, ω the frequency of the impinging light, $\Delta n(V, \omega)$ the differential refractive index between the ordinary and the extraordinary axis and d the thickness of the liquid crystal layer [9]. Consequently to Equation 2.1, applying different voltages will determine different phase delays.

In a more general framework, by independently varying the voltages applied in distinct sections of the layer, we can imprint a specific phase delay for a light beam impinging on that specific section.

This possibility is shown in figure 2.6, where we present a side view of the SLM. The crucial difference between this general configuration and the simplified scheme presented in figure 2.6 resides in the pixelation of the bottom electrode. Therefore, we can think the simple representation of figure 2.5 as just one single pixel of the more general structure of figure 2.6. Moreover, the presence of a dielectric mirror suggests that a reflection geometry rather than a transmission one can be also employed [8].

[3] Liquid crystals are named *nematic* when their molecules have no positional order but tend to point towards the same direction, identified by the name *director*.

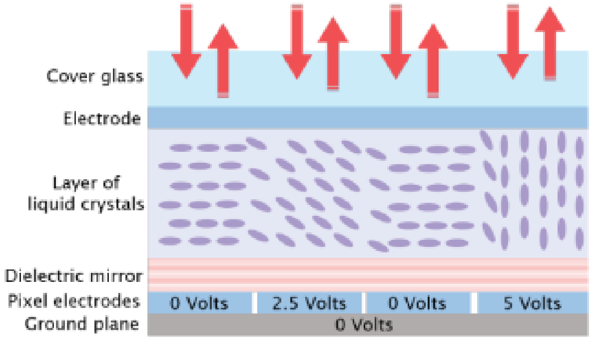

Figure 2.6: lateral section of the SLM. The pixelation of the electrodes allows us to imprint a different phase delay at every pixel. Impinging on the SLM with a dispersed light beam enables then the possibility of performing an independent phase shaping of the different spectral components.

Recalling the 4f scheme of figure 2.4, a reflection geometry (typically called *folded 4f scheme*) can be set up by using only the first grating-lens pair, which acts both as dispersive and collimating elements. Therefore, a simple SLM consists in a pixelated array on which the pulse spectrum is dispersed along the direction of pixelation (i.e. in the horizontal direction of Figure 2.6). By controlling the voltage applied at each pixel it is possible to control the phase of each dispersed spectral component impinging on it.

Amplitude modulation

Until now, we have only explored the capability of the LC-SLM of manipulating the phase of each pulse component. However, more complex tools based on a similar scheme can be used to achieve a simultaneous shaping of both phase and amplitude of the femtosecond pulse. We stress that having access to frequency-resolved amplitude shaping is crucial in our experiment since we need to control the spectral content of the local oscillator (LO). To achieve this experimental purpose we have exploited the method presented in [10], which is the basis of the pulse-shaper arrangement employed in our experiment (figure 2.3).

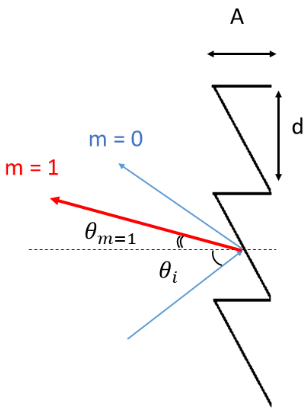

Figure 2.7: diffraction from a sawtooth profile grating.

The method relies on the use of a 2D SLM instead of a linear one. The SLM employed in our set-up[4] consists in a pixelated matrix of 1050 x 1440 pixels, which is placed at the focal plane of a folded 4f scheme. The fundamental advantage of using a 2D matrix relies in the fact that we have

[4]SLM-100 Santec

access to an additional degree of freedom, that is the choice of the voltages to be applied along the vertical direction.

The method proposed in [10] consists in choosing a proper combination of voltages, whose final effect results in the application, to each spectral component, of a sawtooth phase function along the vertical direction. The overall result of this method is that every frequency component impinging on the SLM sees a blazed phase grating (figure 2.7), by which it will be diffracted according to well known grating equation:

$$d[sin(\theta_m) - sin(\theta_i)] = m\lambda \tag{2.2}$$

In the previous equation, d is grating period, m the diffraction order, θ_m the angle at which the m-order beam is diffracted, θ_i the incidence angle and λ the wavelength of the impinging spectral component.

With a proper alignment of the SLM, it is possible to make the first order diffracted beam (figure 2.7) go back to the cylindrical lens, in order to eventually get a collimated beam out of the pulse-shaper (Figure 2.8).

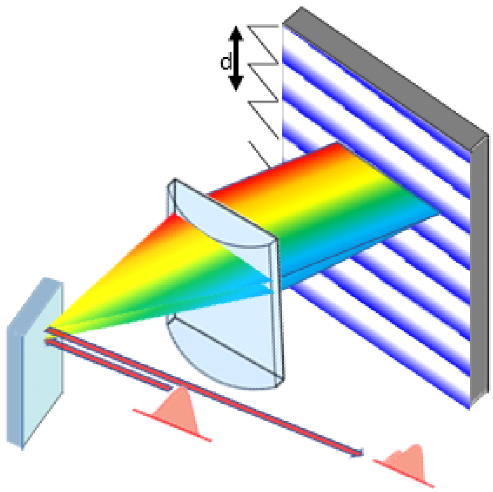

Figure 2.8: using the folded geometry configuration, the first order beam produced by the SLM pattern goes back to the cylindrical lens and, with a proper alignment, exits collimated from the pulse shaper.

2.2.3 Pulse shaping capabilities

In the experimental framework adopted (figure 2.8) the SLM mask can be hence regarded as a set of several blazed gratings, as many as the pixels along the horizontal direction. Therefore, a complete control on the first-order diffracted light can be achieved by modifying the parameters of each blazed grating. More precisely, the vertical position and the depth of each grating can be modified in order to modulate respectively the spectral phase and the amplitude of the first order diffracted beam.

Experimentally, these phase and amplitude manipulations related to the sawtooth grating parameters are obtained by applying a proper combination (a pattern) of voltages at each pixel within the 2D matrix [8]. Figure 2.9 shows some examples of SLM patterns and the first order shaped pulse they produce:

- in figure 2.9a the same blazed profile is applied along the entire horizontal axis. The effect is that every dispersed spectral component impinge on the same diffraction grating. Therefore, the outcoming spectral components will preserve their relative phase and amplitude. However, the absolute pulse amplitude will change, since only the first-order diffracted beam is analyzed.

- figure 2.9b depicts an example of amplitude shaping. In this case, the pattern applied shows a diffraction grating just for a selected region of pixels and no vertical modulation in the remaining part of the screen. Therefore, the diffraction will happen just for the frequencies impinging on the selected region. This results in an outcoming first order pulse with a narrow frequency band. In our experiment we perform this particular shaping on the local oscillator and then we scan the different modes of the LO pulse (and so of the emitted probe) by changing the SLM region where the blazed pattern is applied.

- a shaping of the spectral phase is presented in figure 2.9c. We apply a sawtooth profile along the horizontal axis with a change in its vertical position that follows a quadratic behavior. The shaped pulse exhibits a *chirp*, i.e. a quadratic modulation of the phase that results in a time broadening. In our experiment, we exploit the SLM capability of controlling the spectral phase to perform an accurate compression of the signal.

Multiple beams shaping

Until now we have only taken into account the situation in which a single beam impinges on the shaping matrix. However, our pulse-shaper can be easily adapted to perform multiple-beam shaping, that is a needed requirement to independently shape the signal and the local oscillator in our multimode heterodyne set-up. The multiple-beam shaping can be accomplished by applying a different pattern in distinct vertical portions of the SLM matrix.

In figure 2.10 we illustrate the double shaping configuration adopted in our set-up (figure 2.3). In order to perform a multiple-beam shaping, the local oscillator and the probe must proceed through the pulse shaper in a parallel vertical configuration[5]. The incoming local oscillator sees a grating pattern that enables its frequency selection. Conversely, the signal (probe) experiences a uniform pattern along the dispersion axis which does not modulate its spectral content[6].

[5]The alignment must ensure that a rotation of the diffraction grating causes the same effect on the two beams.

[6]This is the case if the signal pulse presents no temporal broadening. Otherwise, a correction of the phase can be performed.

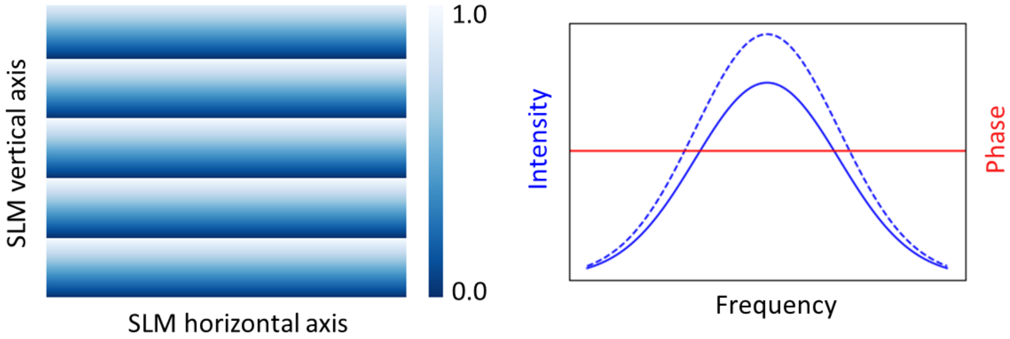

(a)

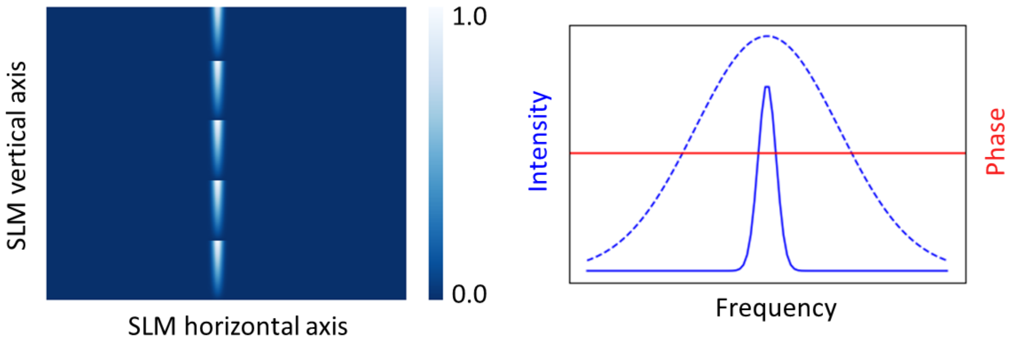

(b)

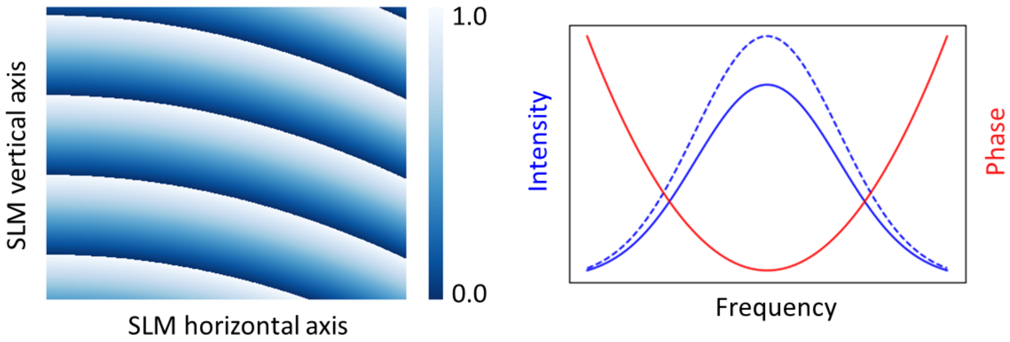

(c)

Figure 2.9: Some examples of SLM patterns and of the associated first order shaped pulses. The spectrum of the pulse impinging on the SLM is represented by the blue dashed line.

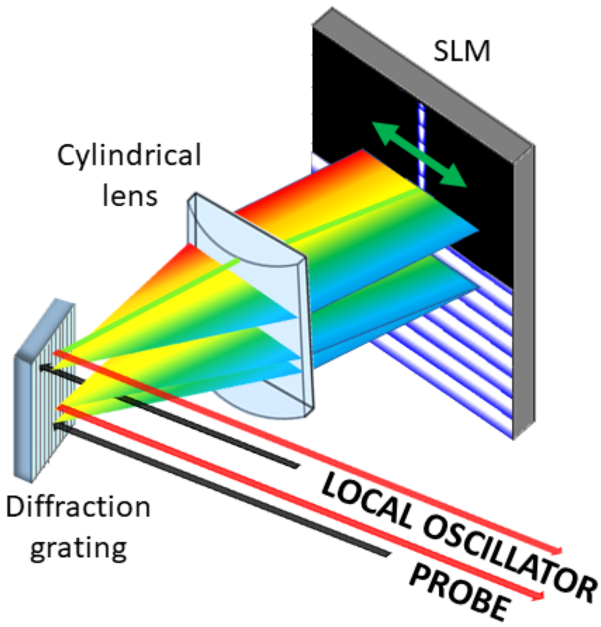

Figure 2.10: scheme of our multiple-beam pulse shaper. We impinge on the SLM with both the local oscillator and the probe. In order to perform an indipendent shaping of the two beams, we apply different patterns on the two vertical regions of the screen. In particular, the incoming local oscillator sees a grating pattern that enables its frequency selection, while the signal sees a uniform diffraction pattern.

2.2.4 Pulse shaper calibration

In order to introduce the previously mentioned spectral features in a controlled manner, a calibration of the pulse-shaper is required. In particular, the following calibration tests are needed:

- *Frequency calibration*, in order to retrieve the correspondence between the incoming pulse frequencies and the SLM horizontal pixels.
- *Calibration of liquid crystals phase*, in order to associate the voltage value to the phase shift induced by the liquid crystals (equation 2.1)
- *Amplitude calibration*, to obtain a relation between the blazed grating depth and the first-order diffracted amplitude.
- *Grating period calibration*: We notice that, according to equation 2.2, different frequencies would be diffracted in different directions by a grating having a fixed period. Since our purpose is to get a collimated beam in output of the 4f-folded-line, we linearly increase the period of the gratings on which higher frequency spectral components impinge.

The complete characterization of the SLM adopted in our set-up can be found in [11]. In the following, we discuss only the frequency calibration procedure, since it is linked to the choice of LO frequencies used in Multimode Heterodyne Detection.

The goal of the frequency calibration is associating to every pixel of the SLM horizontal axis a frequency of the spatially dispersed pulse impinging on it. To find this correspondence, we use a pattern that presents a diffraction grating just on a selected region (figure 2.11a). In this way, we produce a spectrally narrow band pulse peaked on a certain frequency. We then perform a scan through the SLM horizontal axis acquiring every spectrum produced by means of a commercial spectrometer . At the end of the acquisition, we obtain a plot that associates the central pixel of the selected regions to the peak frequency of the shaped pulses (figure 2.11b). With a $1/x$ like function fit of the data [11] we're able to associate a frequency to every SLM horizontal pixels.

Frequency resolution of the pulse shaper

The frequency difference between two neighbouring pixels determines the maximal spectral resolution $\Delta\omega$ of the pulse shaper and hence of our frequency resolved interferometer. Indeed, smaller frequencies modulations can't be obtained because it would mean applying two different voltages at the same pixel.

A quick test that investigates the frequency resolution of the setup consists in applying a sequence of gaussian profile patterns with a decreasing width σ and acquiring the correspondent shaped spectra. For σ values higher than the shaper resolution, we retrieve a narrowing of the pulse spectra. When, with the gaussian width σ, we approach and go below the frequency resolution, diminishing the pattern σ won't affect the shaped pulse. This happens because the shaper frequency resolution is determined by the pixel size, and hence applying patterns with $\sigma < \Delta\omega$ results in applying two different voltages at the same pixel.

Therefore, the smaller σ value that generates a narrowing in the pulse spectrum is the experimental frequency resolution. We estimated a maximal spectral resolution $\Delta\omega \sim 0.1$ THz.

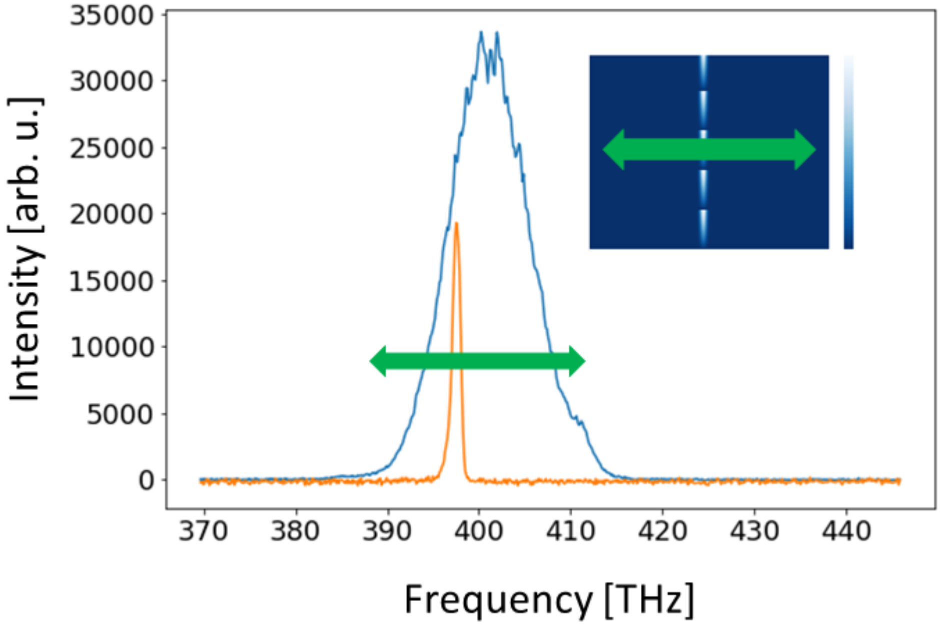

(a)

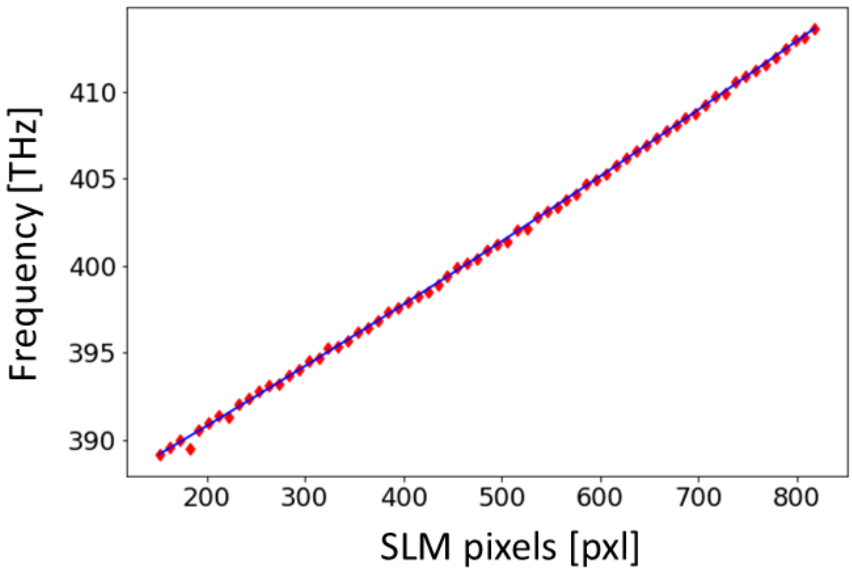

(b)

Figure 2.11: frequency calibration scans the pulse spectrum by means of gaussian profile patterns (a). The result is a plot (b) that associates a frequency to every SLM horizontal pixel.

2.3 Balanced Heterodyne detection using polarizing beam splitters

In Chapter 1 we highlighted that, by means of Balanced Heterodyne Detection (BHD), the classical noise can be killed and therefore the shot noise regime can be reached. This is crucial for achieving the best signal-to-noise ratio and for studying quantum fluctuations (Chapter 5).

The problem that arises with a common BHD setup (figure 1.1) is that achieving a perfect balancing is really difficult. Indeed, the beam splitter used to recombine the signal with the local oscillator will never perform an ideal 50:50 splitting, generating a non-zero balance between the two final channels.

As we proved by means of theoretical calculations in Appendix A, the presence of a non-zero balance determines a growth of the classical noise contribution. In order to correct this issue, the standard procedure consists in the addition of dissipating optical elements along the most intense channel. In this section, we present an alternative balancing configuration [12] that provides a finer tuning of the balance .

The setup we adopt replaces the 50:50 beam splitter with a system of two *polarizing beam splitters* (PBS), i.e. optical elements that split an incoming beam in two beams with orthogonal polarization. A scheme of the configuration is depicted in figure 2.12.

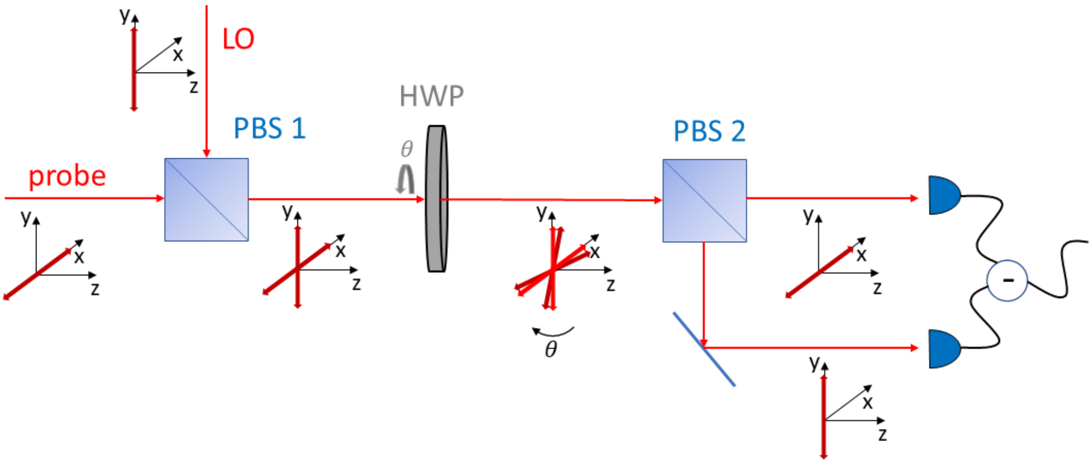

Figure 2.12: scheme of the configuration we use to do the Balanced Heterodyne Detection. The probe and the LO, with orthogonal polarization, are recombined with a polarizing beam splitter (PBS1). The polarization of the exiting beam is rotated by means of a Half Wave Plate (HWP) and then a second polarizing beam splitter (PBS2) divides the different polarization components. Finally the two outcoming beams are acquired. The rotation of the Half Wave Plate provides an accurate control of the balance between the two channels.

The local oscillator and the probe impinge with orthogonal polarizations[7] on the first PBS. Then, before the second PBS, a Half Wave Plate rotates of an arbitrary angle the polarization of the recombined beam. Finally, the last PBS divides the incoming beam in two beams (with orthogonal polarizations) that are sent to the detector.

We stress that, by rotating the Half Wave Plate, we're able to change the amount of light that resides in the two orthogonal polarizations and hence to control the balance of the two channels. This results in an actual tunable beam splitter that we control with the arbitrary rotation of the Half Wave Plate.

We underline that polarizing beam splitters do not provide a perfect balanced detection too. However, the fine tuning of the balance that we perform allows us to heavily reduce the non-zero balance and hence the classical noise contribution. A theoretical representation of the polarazing beam splitters balancing setup can be found in Appendix B.

[7]This can be easily achieved by placing a Half Wave Plate along one of the two optical paths.

2.4 Detection system

To perform Multimode Heterodyne Detection we need to measure the differential photon current of the two final beams (figure 2.3). The subtraction between the two channels can be performed in the data analysis acquiring independently the two signals or directly by the detector.

The first method enables us to use multi channel detectors, like photodiodes arrays. As we mentioned in previous sections, to perform a frequency resolved measurement with a multi channel detector it suffices to disperse each final beam with a prism (figure 2.13). Thus, each detector channel measures a different portion of the pulse spectrum and hence all frequencies are acquired independently at the same time.

However, performing the subtraction of the photon currents just in the data analysis has also a disadvantage. Indeed, photon currents measured on each of the two detectors are affected by an independent stochastic electronic noise. This electronic noise adds to the fluctuations, both classical and quantum, of the measurement and hence lowers the signal to noise ratio. Moreover, when we perform the subtraction of the two current values, the electronic noise of the two channels doesn't cancel but adds[8], enhancing the noise of the heterodyne trace.

A solution is offered by differential detectors, i.e. instruments that perform directly channels subtraction. The special feature of these tools is that subtraction occurs before the signal amplification. This is done in order not to amplify the intrinsic detector electronic noise and obtain a low noise measurement.

Importantly, multi channel differential detectors aren't already available and just single channel ones are provided. Therefore, to perform a Multimode Heterodyne Detection experiment with these detection systems, we have to shape the LO pulse and acquire one frequency at a time (figure 2.2b). We underline that performing a frequency scan for every pump and phase delay highly increases the acquisition times.

Because of the utility of both fast multi channel and low noise acquisitions, we implement a double detection system in our setup, with a differential detector and a pair of photodiodes arrays. The switch between the two configurations is done by means of a mirror with a magnetic mount.

Both configurations provide a shot by shot pulse acquisition, enabling the possibility of statistical studies (Chapter 5). In the following sections, a description of the two types of detector employed. Noise considerations are presented in Chapter 3.

[8]This happens because the electronic noise of each detector is independent and stochastic.

2.4.1 Fast acquisition system: photodiodes arrays

The first configuration we present is the that employs multi channel detectors. In this scheme each heterodyne channel is treated independently, leaving the subtraction between the two to the data analysis.

As previously mentioned, we perform single-shot frequency resolved measurements of the pulses. To achieve this goal, each beam exiting from the final beam splitter is routed to the detection area and diffracted by means of a prism. The spatially separated spectral components finally impinge on the detector, which consists of a linear array of 256 silicon photodiodes (*Hamamatsu*). With this scheme, reported in figure 2.13, every array pixel measures a different pulse mode. The result is a frequency-resolved measurement.

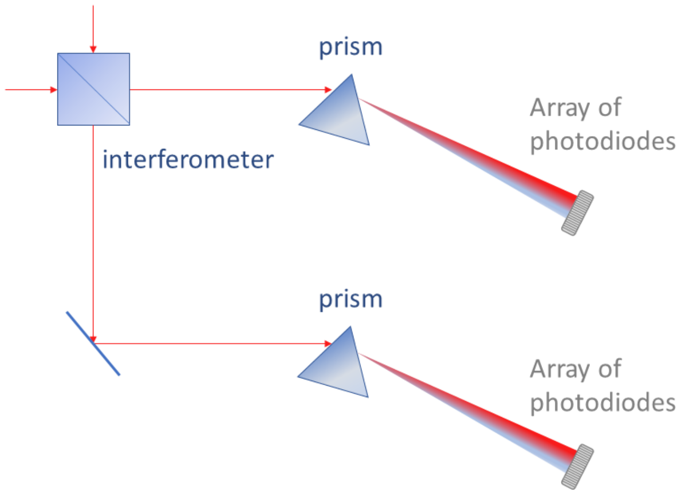

Figure 2.13: scheme of the arrays acquisition system. Each beam coming out of the interferometer impinges on a prism that spatially separates the different spectral components. The dispersed pulse is then detected by an array of silicon photodiodes.

In order to perform a measurement, we first have to calibrate each photodiode array, i.e. assign a frequency value to each pixel. For this purpose, we rely on the frequency calibratied pulse shaper. Indeed, we know exactly the matching between each horizontal pixel of the SLM matrix and each frequency within the pulse bandwidth (figure 2.11). So, to calibrate the arrays we just need to establish a relation between the 1050 SLM pixels and the 256 array ones.

To achieve this purpose, we apply a gaussian profile pattern on the SLM[9]. In this way, we produce a spectrally narrow band pulse peaked on a specific frequency. We then shift the gaussian pattern through the SLM horizontal axis acquiring every spectrum with the photodiodes array. As we've seen before (figure 2.11), this procedure results in a scan of the pulse modes. Performing a linear fit between the gaussian peak positions (in SLM pixel units) and the modes detected (in arrays pixel units) associates a frequency to each array pixel (figure 2.14).

We stress that SLM frequency calibration and array calibration are exactly the same measurement: the difference resides in the fact that for the former frequencies are known (by means of a commercial spectrometer) and their positions on the SLM aren't, whereas for the latter it is the opposite[10].

Once we have calibrated the two arrays, we can match their dispersions by means of interpolation and then perform the current subtraction. An example of unbalanced single channels with their differential signal is shown in figure 2.15.

[9] We recall that this is exactly the same pattern used for the SLM frequency calibration (figure 2.11a).

[10] We underline that SLM frequency calibration must have already been done in order to perform the array calibration.

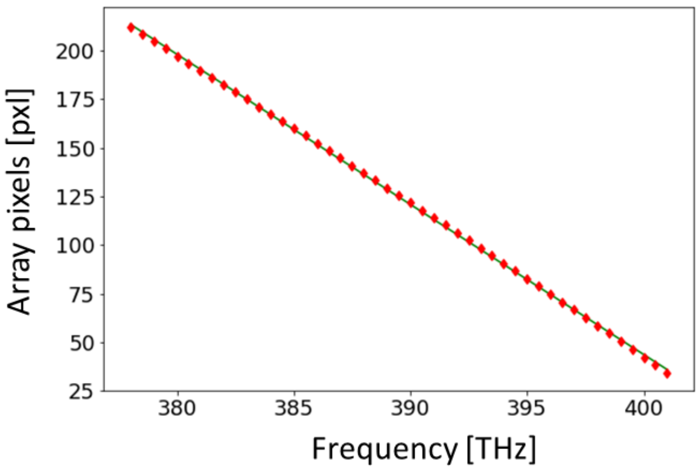

Figure 2.14: by scanning different pulse frequencies by means of SLM shaping we're able to associate a frequency to each pixel of the detector.

We underline that, with this configuration, there is no need to shape the local oscillator (figure 2.2) in order to perform Multimode Heterodyne Detection. In fact, all the probe frequencies are spatially dispersed by the prism and acquired independently by the detector. Therefore, we need no SLM frequency scan and consequently acquisition times are drastically reduced.

The reason we do not adopt exclusively this configuration is that our interest resides also in quantum fluctuations studies (Chapter 5). For this purpose, a very low electronic noise is needed and, as we'll see (Chapter 3), this requirement is fulfilled just by the differential detector. None the less, arrays detection system is fit for mean value measurements (Chapter 4) and in general for quick scans of the system dynamics.

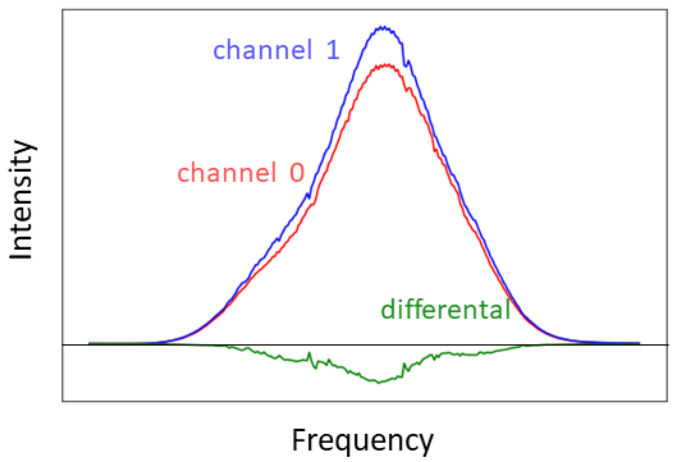

Figure 2.15: example of the unbalanced signal measured with photodiodes arrays. Single channel (red and blue) and differential spectra (green) are reported.

2.4.2 Low noise configuration: differential detector

Since we're intrested in low noise measurements for quantum fluctuation studies (Chapter 5), we implement in our setup a second configuration that provides a very high signal to noise ratio.

This configuration employs a differential detector consisting of two silicon photodiodes (*Hamamatsu S3883*) connected in reverse bias and followed by a low noise charge amplifier. Each photodiode measures the photon current of one of the two interferometer outcoming beams (figure 2.3). We stress that reverse bias linkage operates the physical subtraction of the two signals, while the amplification happens only at the final stage.

Performing the amplification after the physical subtraction permits not to increase the value of the noise produced by the electronic system. After the amplification, the differential signal is digitized by means of a high speed digitizer ADC card (*Spectrum M2i*) with a dynamical range of 16 bit [6].

Once the detector response has been digitized, we need a systematic way to convert the acquired signal to a number representative of the pulse intensity. This single number has been obtained by performing the scalar product between the digitized pulse and the detector response and by subsequently integrating the so obtained pulse. The detector response has been measured by digitizing the output voltage of a single diode and by normalizing its response (figure 2.16).

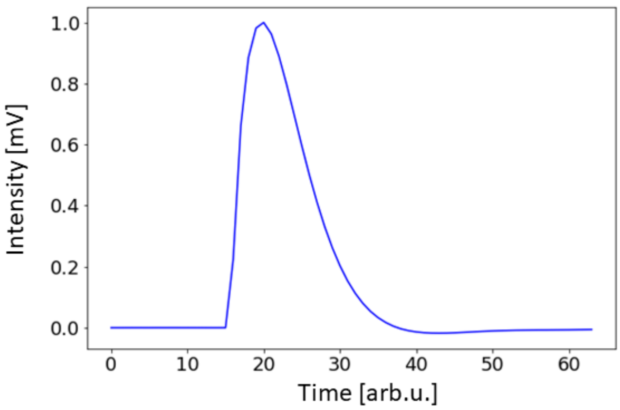

Figure 2.16: detector response measured by digitizing the output voltage of a single diode and by normalizing the outcome. We perform a scalar product between this reference response and the digitized pulse in order to apply different weights to different noise contributions. In particular, electronic noise present at negative times is drastically reduced.

The reason we do not perform directly the integration is that the scalar product enables to apply different weights to different noise contributions. In particular, the negative time current fluctuations (i.e. before the pulse arrival), related to electronic noise, can be strongly reduced.

In conclusion we underline that the disadvantage of performing low noise measurements with the differential detector resides in the long acquisition times. This is due to the fact that differential detector is single channel[11] and therefore, to perform a frequency resolved measurement, we have to acquire one frequency at a time (figure 2.2b). Quantitative noise estimations performed with this detector are reported in Chapter 3.

[11] Multi channel differential detectors aren't available yet.

2.5 Carrier-Envelope Phase stabilization system

The laser + optical parametric amplifier system we use guarantees a great stability and repeatability of the light pulses produced, both in intensity and spectral shape. The only feature that changes pulse by pulse is the absolute phase[12] of the electric field. In order to perform some phase-stable measurements (see Chapter 5) we implemented a commercial Carrier-Envelope Phase stabilization system[13] (CEP) in our experimental setup. In the following, the description of its working principle.

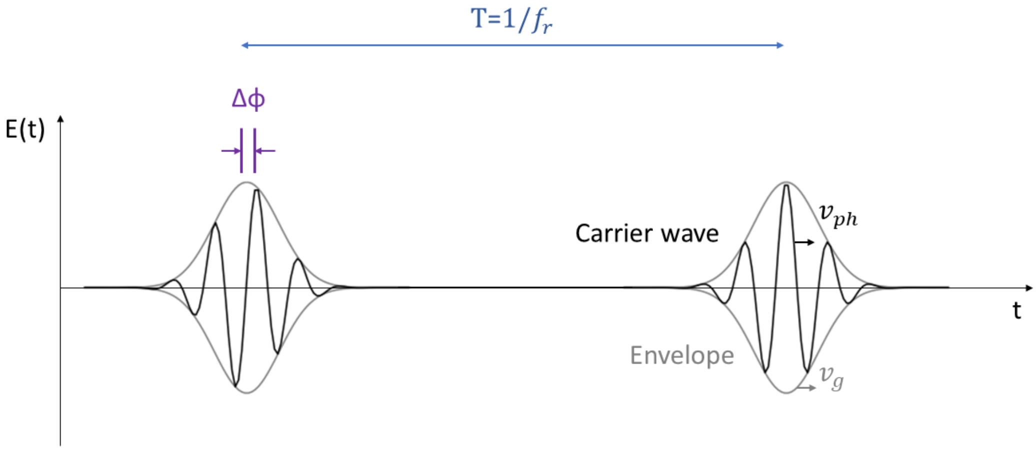

Figure 2.17: a light pulse electric filed can be seen as a product between an oscillating function, the *carrier wave*, and a modulating function, the *envelope*. Because of the different travelling speeds of these two components, respectively v_{ph} and v_g, every pulse will accumulate a phase shift $\Delta\phi$ determining a change in the absolute phase of the electric field.

The electric field of a laser pulse is the product of an oscillating function, *carrier wave*, for a modulating function called *envelope*. Its mathematical representation is:

$$E(t) = A(t)e^{2\pi i f_c t} \tag{2.3}$$

where $A(t)$ is the generic envelope function and f_c is the oscillation frequency of the electric field. For laser sources, the time dependent amplitude $A(t)$ presents a periodicity determined by the laser repetition rate f_r. We can exploit this periodicity to express $A(t)$ as a Fourier series:

$$A(t) = \sum_{n=1}^{\infty} A_n e^{2\pi i n f_r t}$$

Thus, the electric field becomes:

$$E(t) = \sum_{n=1}^{\infty} A_n e^{2\pi i t(f_c + n f_r)} \tag{2.4}$$

The spectrum of equation 2.4 represents a comb of laser frequencies precisely spaced by the pulse repetition rate f_r, where the coefficients A_n, that contain the spectral intensity and the relative phases of the modes, do not depend on time. In general, the oscillation frequency f_c is not a multiple of the repetition rate f_r. This is because the carrier wave travels with the phase velocity $v_{ph} = \omega/k$, whereas the envelope propagates with the group velocity of the electric field $v_g = \partial\omega/\partial k$. Thus, the carrier phase will be shifted after each round trip with respect to the pulse envelope by say $\Delta\phi$ (figure 2.17). This results [13] in a shift of the comb of laser frequencies by an offset frequency f_0 given by:

$$f_0 = \frac{\Delta\phi}{2\pi} f_r \tag{2.5}$$

[12] i.e. the phase of the electric field in the correspondence of the pulse peak.
[13] *MenloSystem XPS800-E*

We can rewrite the laser pulse frequency comb as a function of the offset f_0 in the following way:

$$f_n = f_0 + nf_r \tag{2.6}$$

The instability of the laser pulse absolute phase is due to the change of $\Delta\phi$ (and so of f_0) that happens at every pulse. The Carrier-Envelope Phase stabilization system fixes the offset frequency by mean of an f-$2f$ interferometer combined with a feedback loop [14]. In order to explain the CEP working principle, we first introduce the f-$2f$ interferometer.

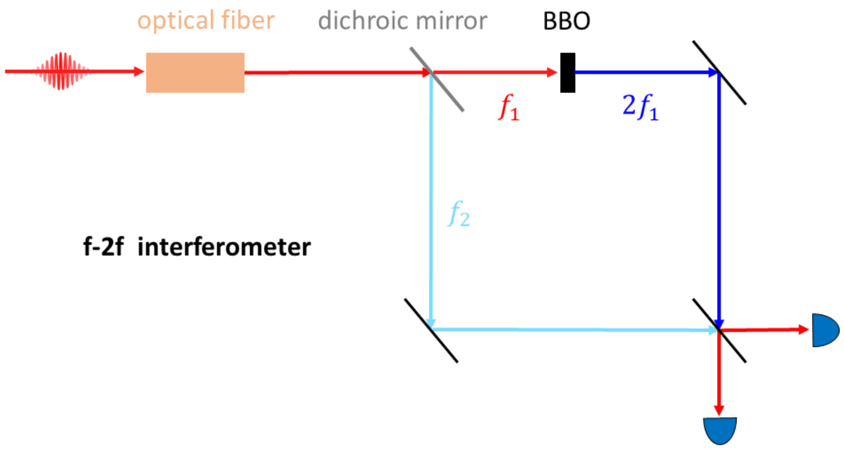

Figure 2.18: scheme of the f-$2f$ interferometer used to measure the offset frequency f_0. Pulse spectrum is broadened by a zero dispersion optical fiber in order to span at least an octave. Then, a dichroic mirror splits high an low frequencies and directs them onto different optical paths, where low frequencies experience Second Harmonic Generation in a BBO crystal. The produced second harmonics are finally recombined with the pulse high frequencies, giving rise to a beat note at the frequency f_0.

In an f-$2f$ interferometer, low frequencies of a broadband light pulse interfere with the high frequencies of the same pulse (figure 2.18). Moreover, the interference occurs between all couples of frequencies f-$2f$. If the pulse spectrum isn't wide at least an octave[14], it can be broadened by means of an optical fiber [15].

The broadened pulse impinge on a dichroic mirror, i.e. an optical element that reflects a well determined range of frequencies and transmits the others. Thanks to this element, we separate high and low frequencies of the pulse.

The low frequency beam impinges on a Barium Beta Borate crystal (BBO) where second harmonic generation occurs[15]. In this process, a low frequency photon $f_1 = f_0 + n_1 f_r$ is upconverted into a doubled frequency one $2f_1 = 2f_0 + 2n_1 f_r$.

Subsequently, the beam that experienced second harmonic generation is recombined with the high energy branch. If we consider the interference between the doubled frequency mode $2f_1 = 2f_0 + 2n_1 f_r$ and the high frequency one $f_2 = f_0 + n_2 f_r$ with $n_2 = 2n_1$ [16], we see that it gives rise to a beatnote (figure 2.19):

$$f_{beatnote} = 2f_1 - f_2 = 2f_0 + 2n_1 f_r - f_0 - n_2 f_r = f_0$$

Therefore, a measurement of the beat note returns us exactly the frequency offset of the frequency comb (equation 2.6). In a CEP system, the measured value f_0 is then sent to a feedback loop that moves the cavity mirrors in order to change the v_g/v_{ph} ratio [14, 15] and thus lock the offset frequency.

[14] i.e. the highest frequency is the second harmonic of the lowest frequency.
[15] We underline that second harmonic generation occurs just for the modes residing in the phase matching region.
[16] We stress that this process doesn't occur necessarily just for two modes. Every couple of modes that goes under this condition will contribute enhancing the signal.

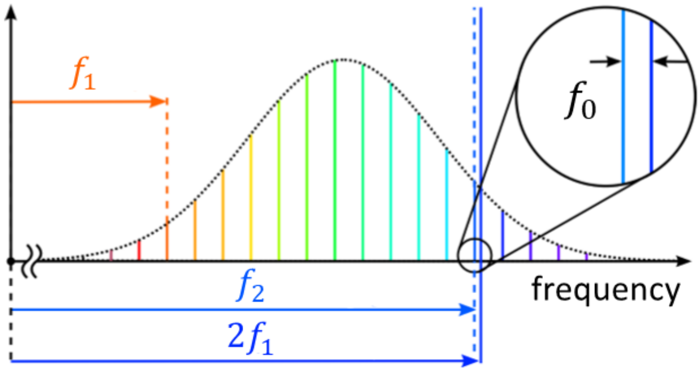

Figure 2.19: to perform a measurement of the offset frequency f_0 we generate, with a non linear process, the second harmonic of a pulse low energy mode $f_1 = f_0 + n_1 f_r$. Then, we look at the beat note produced by the interference of $2f_1$ with a high energy mode $f_2 = f_0 + 2n_1 f_r$: the outcome is precisely f_0. We finally send this information to a feedback loop in order to lock the value of f_0.

Chapter 3

Characterization of the interferometric setup for optical tomography with short pulses

Now that we have presented the experimental setup (Chapter 2), we need to perform some preliminary studies on it. In particular, we want to characterize the acquisition system in the absence of pump excitation. We refer to this situation as *equilibrium system*.

The first study that we perform is centered on measurement noise. This is done in order to understand if we effectively kill classical fluctuations with balanced detection and hence reach the shot noise regime. We also provide a characterization of the noise introduced by interferometer instabilities.

In the second part of the Chapter we focus on quadrature measurements. In particular, we present a rescaling procedure to obtain, from the measured photon currents, the quadrature trace in photon units. As a conclusion of the Chapter, some quantitative photon number estimations are presented.

3.1 Characterization of the photonic noise

In order to perform fluctuation studies on the non-equilibrium system, we first need a preliminary characterization of the noise. The most important information that we look for is shot noise, i.e. a noise regime where the fluctuation in the measurements are dominated by the intrinsic fluctuations of the photon number. Indeed, measuring under shot noise conditions enables the possibility of studying quantum fluctuation dynamics (Chapter 5).

In next paragraphs, after a brief theoretical introduction, the behavior of our two detection systems (see section 2.4) is compared, in order to understand which is more suited for measuring quantum fluctuations.

As a conclusion of the noise study, some considerations about the interferometer stability and how it affects the measurement noise are presented.

3.1.1 Propagation of classical noise: a Beam Splitter Model

In this section we develop a formalism to distinguish intrinsic (quantum) and extrinsic (classical) fluctuation in time domain experiments. In Chapter 1 we saw that if we measure the differential photon current between the two beams coming out of a beam splitter, the noise has two contributions: a classical one, depending on the incoming beam noise, and a quantum one, related to the initial number of photons.

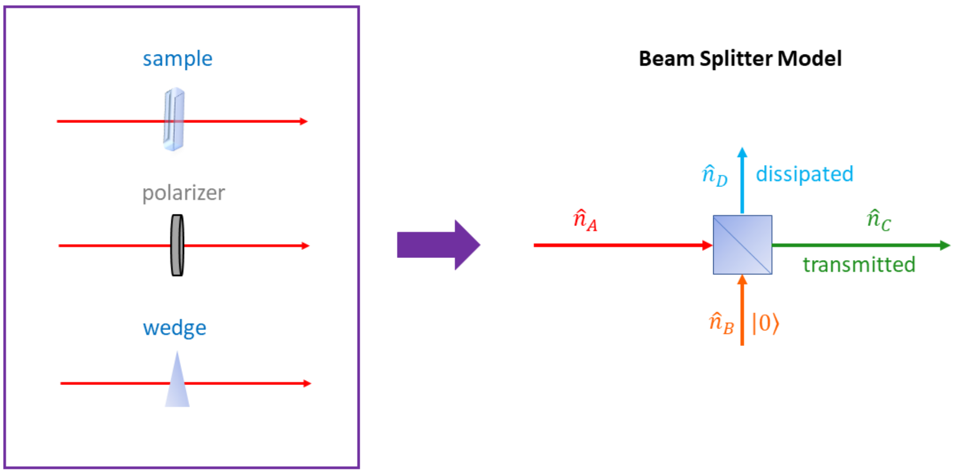

Figure 3.1: the basic principle that underlies the Beam Splitter Model is substituting every optical element (polarizers, lenses, etc.) with a beam splitter. Doing so, we're able to simulate the dissipation that occurs on the optic and the presence of quantum noise.

In order to predict the weight of these two contributions for a generic optical setup, we need a theoretical model that propagates noise through optical elements. For this purpose, we adopt the so called *Beam Splitter Model* [6].

This theoretical model describes the dissipation of every optical element in the setup by means of a lossless beam splitter (figure 3.1). Recalling that a beam splitter has two entering and two exiting beams, the model attributes the following meanings to the various branches:

- the entering beam ($\hat{n}_A$ in figure 3.1) is the beam impinging on the optical element.
- similarly, the transmitted beam $\hat{n}_C$ represents the optical element exiting beam.
- the reflected beam $\hat{n}_D$ is seen as the radiation dissipated on the optic. This term includes both the reflected photons as well as the absorbed ones.
- the second entrance $\hat{n}_B$ is empty and so introduces quantum noise into the measurement. Therefore, this term accounts for the stochastic nature of all dissipative processes.

Summarizing, the Beam Splitter Model provides an intuitive representation that accounts for both optical losses and quantum noise.

We performed the calculation for a Balanced Heterodyne Setup (more details can be found in Appendix A) and we retrieved the following formulae for the differential photon current $\hat{n}_f$:

$$\langle \hat{n}_f \rangle = |T_1||T_2||R||T|cos(\Phi_{T1} - \Phi_{T2} + \pi)\langle \hat{n}_i \rangle \tag{3.1}$$

and for the related variance σ_f^2:

$$\sigma_f^2 = \frac{\sigma_i^2 - \langle \hat{n}_i \rangle}{\langle \hat{n}_i \rangle^2}\langle \hat{n}_f \rangle^2 + \left(|T_1|^2|R|^2 + |T_2|^2|T|^2\right)\langle \hat{n}_i \rangle \tag{3.2}$$

where $\langle \hat{n}_i \rangle$ indicates the mean photon number of the incoming beam, σ_i^2 its related fluctuation, $|R_j|$ and $|T_j|$ the reflection and transmission coefficients of the j-beam splitter and Φ_{Tj} the phase shift induced on the transmitted beam by the j-beam splitter. Labels refer to elements of figure 3.2.

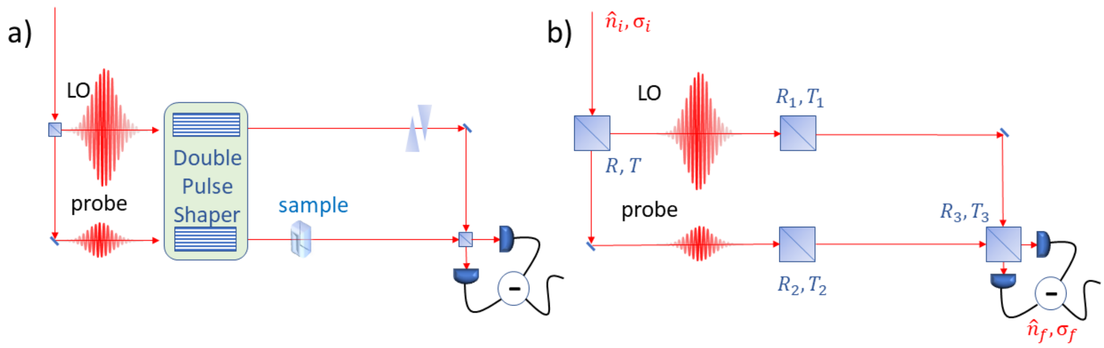

Figure 3.2: representation of our experimental setup (a) according to the Beam Splitter Model (b). A first beam splitter divides the initial beam into local oscillator and signal, then two beam splitters simulate the dissipation experienced along the optical paths and finally the last beam splitter recombines the two beams in order to measure the heterodyne current.

The differential photon current intensity (equation 3.1) shows a sinusoidal dependence from the relative phase between the two beams, that is the behavior expected for the quadrature[1]. Moreover, the variance expression 3.2 is clearly divided in two parts:

- the first term depends both on the differential photon current measured with a quadratic dependence and on the statistical distribution of the initial beam. For example, if the incoming photons have a super-poissonian distribution, i.e. $\sigma_i^2 > \langle \hat{n}_i \rangle$, then the coefficient of $\langle \hat{n}_f \rangle^2$ is positive, giving rise to an increment of the measured noise. Therefore, this term accounts for the classical fluctuation of the incoming laser source.

- the second term depends linearly on the incoming beam photon number and hence is linked to the particle nature of light. So, this term accounts for the intrinsic fluctuations of light.

Having access to the shot noise regime means performing a measurement where the largest noise contribution comes from quantum fluctuations. This means that the second term of equation 3.2 must be greater then the first one. In the following, we investigate the weight of the two contributions for both photodiodes array and differential detector detection systems.

[1]This formula is valid for a perfectly balanced setup, i.e. with a perfect final 50:50 beam splitter. Other terms appear if a small unbalance is present (see Appendix A).

3.1.2 Shot noise linearity test

Since BHD provides a way to drastically reduce the differential photon current measured, and hence the classical noise[2], we're interested in investigating if we have access or not to the shot noise regime, where just quantum noise is present.

To understand how classical fluctuations of the local oscillator enter in the final noise, we can set up an experiment where the signal is blocked and so, in our framework, local oscillator amplifies the vacuum state (figure 3.3). Measuring fluctuations of vacuum heterodyne trace for various LO powers allows us to build a map variance vs photon number.

If shot noise regime is reached, then a linear dependence[3] between variance and photon number should be present.

We perform this shot noise test on both the arrays detection system and the differential detector. The resulting plots[4] are presented in figure 3.4.

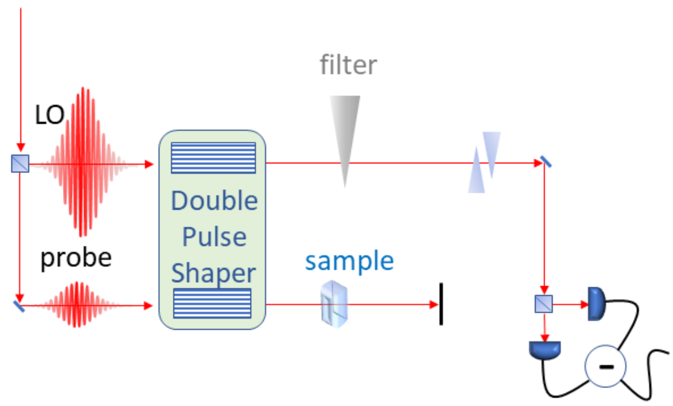

Figure 3.3: to perform the shot noise array test we block the signal in order to measure the fluctuation of the vacuum state for different LO powers. To tune the local oscillator number of photons we insert a graduated filter along its optical path.

Starting from the arrays detection system (figure 3.4a), we can see that the variance growth isn't linear but much faster. This evidence suggests that the dominant noise of the measurement isn't the quantum one. On the contrary, differential detector (figure 3.4b) shows a clear linear behavior, supporting the hypothesis of being in the shot noise regime.

Since the balancing process is done in both cases according to what we explained in section 2.3, we do not expect the great difference of the two plots to be caused by a bad balancing procedure. We rather attribute it to a different behavior of the two detectors and in particular to their electronic noise. This noise is independent on local oscillator intensity and is due to any non-desirable ambient noise, dark current noise from the diodes and to the intrinsic noise of the charge amplifier.

Recalling what we presented in section 2.4, differential detector operates the two channels subtraction before the occurring of signal amplification in order not to amplify electronic noise. This procedure doesn't take place for photodiodes arrays and therefore their electronic noise enters in the amplification process. Thus, we expect the array electronic noise to be much higher then the differential detector one.

[2]Represented by the first term of equation 3.2.

[3]In equation 3.2 we can see that the second term, which corresponds to the quantum noise, depends linearly on the number of photons of the incoming beam.

[4]For this analysis we removed low periodic noises from the data by employing FT filters.

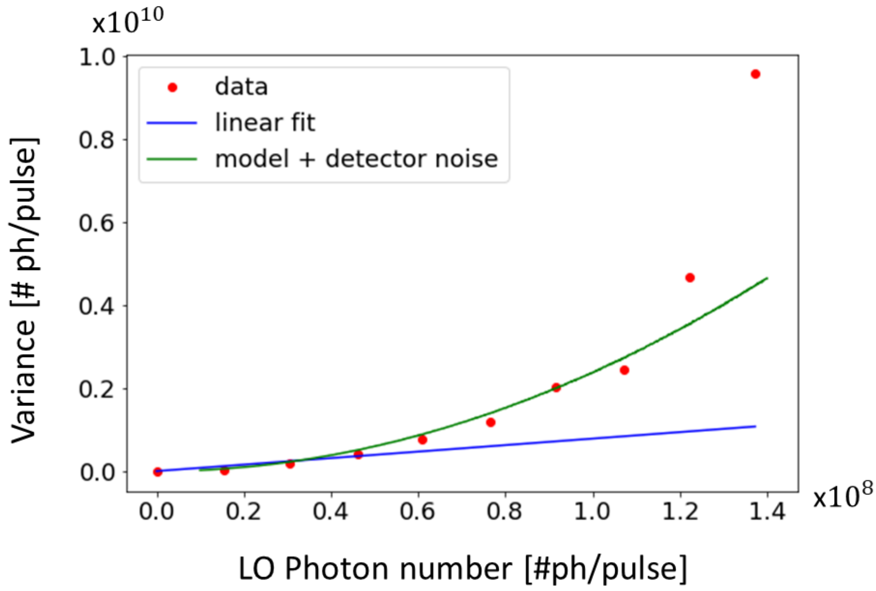

(a)

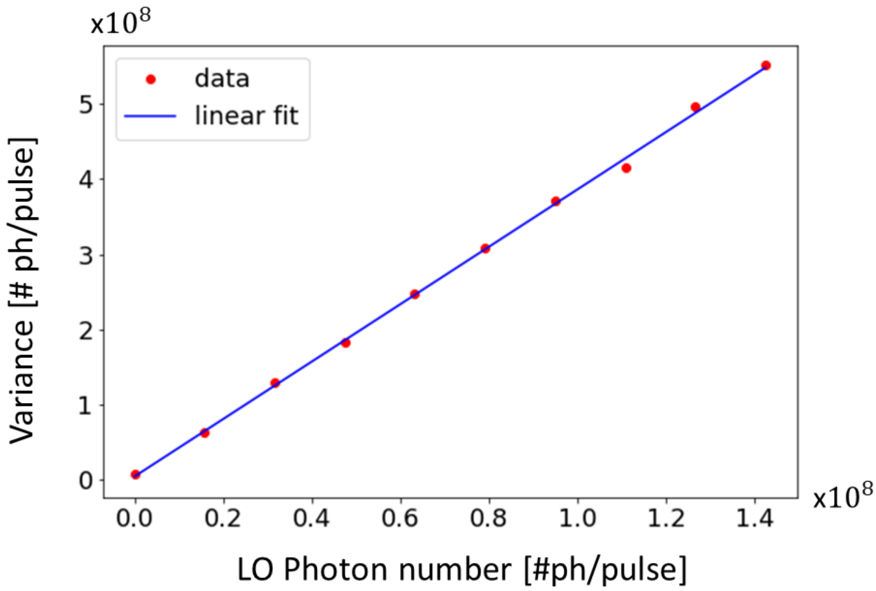

(b)

Figure 3.4: The resulting plots from the shot noise test for the arrays detection system (a) and the differential detector (b). We notice that in the first case, due to the electronic noise, the variance grows much faster than linearly: therefore, quantum fluctuations aren't the dominant noise. An extension of the Beam Splitter Model to the case of noisy detectors shows that electronic noise is the most relevant contribution (green line). On the contrary, the differential detector shows a regular linear behavior, suggesting that with this configuration the shot noise regime is reached.

Electronic noise estimation

Electronic noise can be estimated by measuring the variance of the differential current with the two channels blocked, which corresponds to the detected noise before the arrival of each pulse. In order to compare this noise background for the two detection systems, we estimate the ratio S between the shot noise and the electronic noise. Moreover, according to [16], the electronic noise effect is equivalent to an optical loss channel with equivalent transmission efficiency:

$$\eta = 1 - \frac{1}{S} \tag{3.3}$$

Shot to electronic noise ratio S and equivalent transmission efficiency η of the two detectors are compared in table 3.1.

	arrays	diff. detector
S	1.69	14.46
η	0.41	0.93

Table 3.1: the shot to electronic noise ratio S and the equivalent transmission efficiency η of the two detection systems are compared. We see that the differential detector provides a better shot to electronic noise ratio and a very high transmission efficiency, whereas the arrays transmits less then a photon every two. This confirms that the differential detector is a better choice for low noise measurements.

Differential detector provides a very high transmission efficiency of 0.94/1.0, indicating that the loss of signal caused by electronic noise is the 6%. On the contrary, the arrays have a much lower shot to electronic noise ratio that reflects in a lower transmission efficiency of 0.41/1.0. Thus, electronic noise in the two systems is significantly different.

Electronic noise in Beam Splitter Model

We apply the extension of the Beam Splitter Model presented in [7] to take into account the detector noise. In this framework, electronic noise is treated as an independent stochastic variable that adds a random value to every current measurement. Therefore, its variance is additive with the photon one. The result of Beam Splitter Model + electronic noise prediction is the green line depicted in figure 3.4a.

We see a good agreement between the experimental data and the theoretical prevision. A discrepancy occurs just for high photon numbers of the local oscillator beam. This can be explained by some approximations that we used to integrate detector noise into the noise propagation model. For example, considering the electronic noise independent by the number of photons is a strong assumption that could be violated with high photon numbers.

In conclusion, the shot noise test proved us that we can have access to shot noise regime, but only if employing the differential detector. In fact, photodiodes arrays detection system is affected by an important electronic noise contribution (figure 3.4a) that dominates quantum fluctuations.

3.1.3 Interferometer stability

In this section we discuss the effect of the interferometer instability on the heterodyne traces and in particular on the quadrature noise.

Recalling what we saw in Chapter 2, we use a system of wedges mounted on a piezo translator to have an arbitrary control over the relative phase between the signal and the local oscillator beam (figure 2.2). However, air fluxes, mechanical movements of the optics and other effects can determine a change in the pulses optical paths. This results in an instability of the interferometer and hence in a phase uncertainty. Considering the single mode quadrature $X = X_0 cos(\Delta\phi)$ with X_0 and $\Delta\Phi$ the quadrature amplitude and the relative phase, we can write the quadrature uncertainty σ_X^2 as:

$$\sigma_X^2 = cos^2(\Delta\phi)\sigma_{X_0}^2 + X_0^2 sin^2(\Delta\phi)\sigma_\phi^2 \tag{3.4}$$

where $\sigma_{X_0}^2$ and σ_Φ^2 denote respectively the uncertainty over the quadrature amplitude and phase. We distinguish two noise contributions:

- the first term is related to the uncertainty of X_0 and oscillates with $cos^2(\Delta\phi)$
- the second term is due to the phase uncertainty, its oscillation is $\pi/2$ shifted with respect to the first term and depends on the quadrature amplitude X_0

Because of the quadrature amplitude dependence, we expect the second term to be dominant in the case of high photon number pulses.

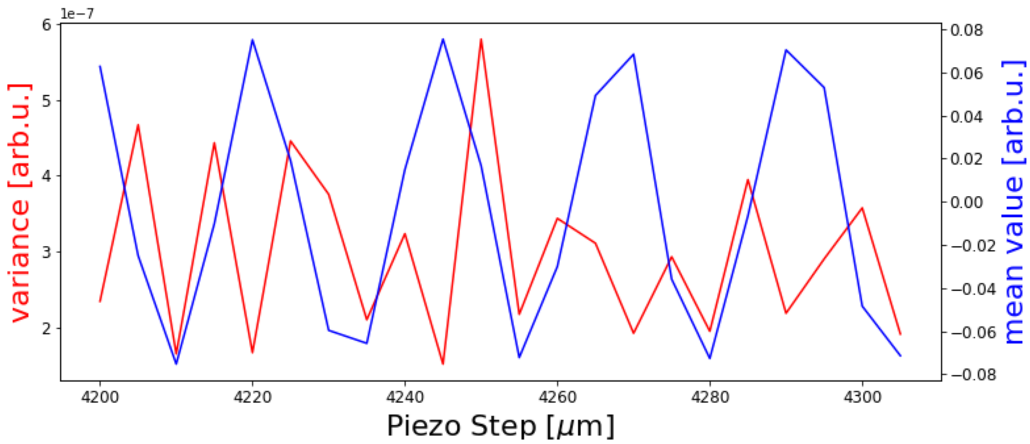

Figure 3.5: comparison between a single mode quadrature (400 THz) and its variance. We retrieve a double frequency oscillation in the variance that can be explained by the uncertainty of the quadrature phase.

An example of quadrature and variance comparison with high photon number pulses is presented in figure 3.5. We see that the variance oscillates with a frequency that is twice the quadrature one. This oscillation can be described by a sinusoidal function squared behavior of the noise. Moreover, the variance exhibits minima where the quadrature has a maximum (in absolute value). Thus, the variance follows a $sin^2(\Delta\phi)$ behavior, confirming our hypothesis of a dominating phase noise.

Such effect is observable also for traces in quantum regime (i.e. with low photon number). In that case, the variance modulation becomes less evident as the number of photons diminishes. In order to quantify this behavior, we perform the Fourier Transform of the variance.

Figure 3.6 shows the Fourier Transformed variance vs pulse frequencies in three different photon number regimes. The peak corresponding to the quadrature second harmonic clearly decreases as

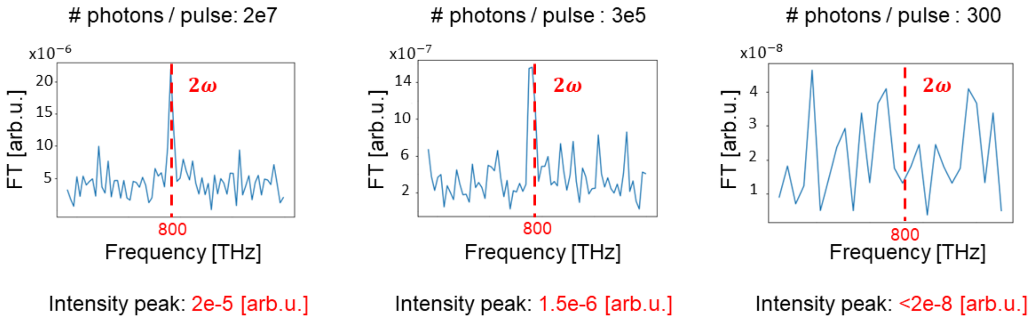

Figure 3.6: plot of the Fourier Transformed variance (of a 400 THz single mode quadrature) in different photon number regimes. In the case of 2 10^7 photons per pulse, the peak corresponding to the frequency twice the quadrature one is clearly visibile. The same occurs in the 3 10^5 plot. In the last case, with just 300 photons per pulse, we can't retrieve a peak at the expected frequency. Comparing the three photon number regimes, we see that the intensity of the second harmonic peak decreases with the number of photons per pulse, as expected.

the number of photons per pulse is reduced. This is explained by the dependence of the phase noise by the quadrature amplitude (equation 3.4).

In conclusion, interferometer instability determines an uncertainty of the quadrature phase. Confirming the prediction of equation 3.4, the phase instability generates a noise that oscillates at a frequency that is twice the quadrature one. This double frequency oscillation diminishes if the number of photons per pulse is reduced.

3.2 A rescaling procedure for the quadrature field for photon number estimations

In Chapter 1 we showed that heterodyne detection provides a measurement proportional to the expectation value of the quadrature X_ϕ, where ϕ is the relative phase between the signal and the LO. However, the measurement we perform returns us a current value for a given piezo step[5], and not directly the quadrature field in unities of photons. Moreover, we have to convert also piezo steps into phase delays.

In the following paragraphs we present the rescaling procedure of heterodyne traces proposed in [17] to obtain from the measured currents data pairs of the type $(x_{\phi_j}; \phi_j)$.

From rescaled heterodyne traces, we then estimate the expectation value of the number operator and we compare it with the mean number of photons estimated by means of beam power considerations. In addition, we will show how the detector inefficiencies can be taken into account.

3.2.1 Rescaling procedure

When we perform a Multimode Heterodyne Detection experiment, we acquire, for every pulse frequency, the differential photon current for every pulse. All the considerations that we'll do in the next paragraphs are referred to a single mode quadrature and are valid for all the frequencies.

Estimation of the conversion factor

When we measure a single mode quadrature, we obtain a current value $I^{meas}_{\phi_j}$, corresponding to a certain piezo position p_j. This value is proportional to the quadrature value x_{ϕ_j}:

$$I^{meas}_{\phi_j} = \gamma' x_{\phi_j} \tag{3.5}$$

We need to evaluate the proportionality factor γ' in order to obtain the quadrature values from the heterodyne trace data. At this point the heterodyne trace of the vacuum state plays a very important role in the rescaling procedure, since it is used as a reference.

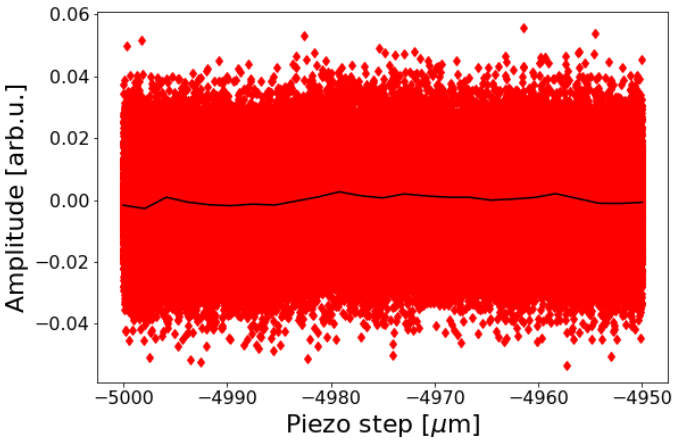

Figure 3.7: heterodyne trace of the vacuum state, acquired blocking the signal beam. The black line represents the mean value, whereas the statistic of the measurement is depicted in red.

When we block the signal beam in a heterodyne measurement, this corresponds to measuring the quadrature values of the vacuum state $|0\rangle$ (figure 3.3). The quadrature expectation value for the vacuum state is expected to be zero for all phases:

$$\langle \hat{x}_\phi \rangle_{|0\rangle} = Tr\left[\hat{x}_\phi |0\rangle\langle 0|\right] = \langle 0| \frac{\hat{a}e^{-i\phi} + \hat{a}^\dagger e^{i\phi}}{2} |0\rangle = 0 \qquad \forall\, \phi \tag{3.6}$$

[5] We recall that the relative phase ϕ between signal and LO is controlled by means of a wedge mounted on a piezo translator.

while the variance is expected to have constant value 1/2:

$$\sigma^2[\hat{x}_\phi]_{|0\rangle} = \langle \hat{x}_\phi^2 \rangle_{|0\rangle} - \langle \hat{x}_\phi \rangle_{|0\rangle}^2 = Tr\big[\hat{x}_\phi^2 |0\rangle\langle 0|\big] = \langle 0| \frac{\hat{a}^\dagger \hat{a}}{2} |0\rangle = \frac{1}{2} \qquad \forall\, \phi \tag{3.7}$$

Thus, we can use the experimental data of the vacuum heterodyne trace (figure 3.7) to evaluate the proportionality factor γ'. To do so, we combine equation 3.5 with the condition 3.7 for the vacuum state variance. The result is:

$$\gamma' = \sqrt{2(\sigma_0^{meas})^2} \tag{3.8}$$

where $(\sigma_0^{meas})^2$ is the variance of the 10^5 experimental data in the vacuum heterodyne trace (figure 3.7).

Now, in order to obtain the rescaled vacuum heterodyne trace, we divide all these data by the calculated factor γ'. Similarly, to obtain the rescaled trace x_{ϕ_j} for quadratures with signal, we have just to divide the measured current $I_{\phi_j}^{meas}$ for the conversion factor γ'.

In figure 3.8 the rescaled vacuum state quadrature is depicted. The dotted blue lines mark out the root mean squared deviation of the rescaled data : $\sqrt{(\sigma_0^{meas})^2/\gamma'} = 1/\sqrt{2}$.

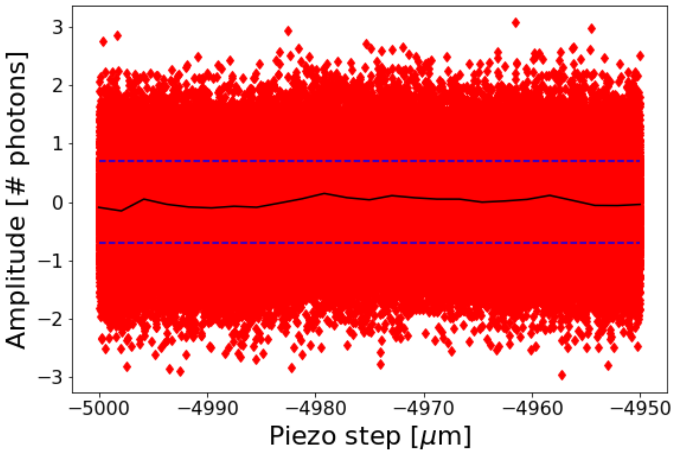

Figure 3.8: rescaled vacuum state trace. The blue dashed lines indicate the root mean squared deviation of the rescaled data.

Rescaling procedure

We underline that measuring only the vacuum state doesn't allow us to establish the exact relation between phase ϕ and piezo position p_i because vacuum quadrature doesn't exhibit a phase dependence. However, we can retrieve this information from the quadrature with opened signal.

Supposing the signal under investigation is in a coherent state $|\alpha\rangle$ with $\alpha = |\alpha|e^{i\theta}$, the field quadrature expectation value will be:

$$\langle \hat{x}_\phi \rangle_{|\alpha\rangle} = Tr\big[\hat{x}_\phi |\alpha\rangle\langle \alpha|\big] = \langle \alpha| \frac{\hat{a}e^{-i(\phi-\theta)} + \hat{a}^\dagger e^{i(\phi-\theta)}}{2} |\alpha\rangle = \sqrt{2}|\alpha| cos(\phi - \theta) \tag{3.9}$$

while quadrature variance results:

$$\sigma^2[\hat{x}_\phi]_{|\alpha\rangle} = \langle \hat{x}_\phi^2 \rangle_{|\alpha\rangle} - \langle \hat{x}_\phi \rangle_{|\alpha\rangle}^2 = \frac{1}{2} \qquad \forall\, \phi \tag{3.10}$$

As mentioned before, we can obtain the value x_{ϕ_j} from the $I_{\phi_j}^{meas}$ by dividing the latter by γ'; further, we can find the phase value ϕ associated to each piezo position p_i exploiting the periodicity of the trace. The whole rescaling procedure is now summarized:

- We divide all the experimental data $I_{\phi_j}^{meas}$ by the factor γ'.
- We perform a fit of the rescaled data with the function :
$$f(p) = f_0 + Acos(\omega p + \phi_0) \tag{3.11}$$
taking f_0, A, ω and ϕ_0 as free parameters.
- Using the parameters values obtained from the fit, we plot the rescaled data, subtracted by the offset f_0, versus the values $\theta_i = \omega p_i + \phi_0$, calculated starting from the measured piezo positions p_i.
- Being Δ the distance between two consecutive θ values for which the fit function has a maximum, we define the variable ϕ such that $\phi = \frac{2\pi}{\Delta}\theta$.
- Finally we plot the rescaled data versus the values $\phi_i = \frac{2\pi}{\Delta}\theta_i$.

Electronic noise treatment

Untill now, we haven't taken into account the electronic noise of the detector. In order to obtain an accurate conversion also for noisy quadratures, we extend the rescaling procedure previously described.

The effect of electronic noise is to add a random quantity to each field quadrature measurement. In [16], Appel at al. demonstrate that this effect is equivalent to an optical loss channel with equivalent transmission efficiency:

$$\eta = \frac{SN}{SN + EN} \tag{3.12}$$

where SN identifies the pure shot noise component and EN the electronic noise[6]. A representation of these two quantities is reported in figure 3.9. We see that the eletronic noise acts as a background that enhances the overall variance. Since our rescaling procedure is based on the vacuum state variance (equation 3.7), that is the pure shot noise contribution of the measurement, we need to take into account electronic noise and consequently obtain a new rescaling factor γ.

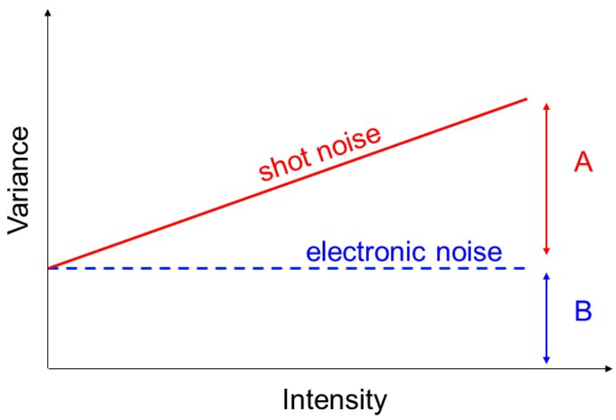

Figure 3.9: representation of the shot noise and electronic noise contribution to the variance as a function of the pulse intensity.

To achieve this goal, we follow the treatment of [16, 17] and, using equation 3.12, we obtain the expression:

$$\gamma' = \sqrt{2(\sigma_0^{meas})^2} = \frac{\gamma}{\sqrt{\eta_{eq}}} \tag{3.13}$$

[6]We point out that equation 3.3 and equation 3.12 are just the same formula written in a different way.

where γ is the conversion factor that considers just the pure shot noise contribution. Actually, inside η_{eq} we considered also the photodiodes inefficiencies. The latter are quantified by their nominal quantum efficiency: $\eta_{pd} = 0.94$. Contemplating also this loss channel, we get: $\eta_{eq} = \eta\eta_{pd}$.

In conclusion, to rescale correctly the experimental data in presence of electronic noise it is sufficient to replace the conversion factor γ' with γ.

3.2.2 Photon number estimation

Once we have the rescaled quadratures, we can use them perform photon number estimations. We know that for a coherent state holds:

$$\langle\hat{n}\rangle_{|\alpha\rangle} = Tr\left[\hat{n}|\alpha\rangle\langle\alpha|\right] = \langle\alpha|\hat{a}^{\dagger}\hat{a}|\alpha\rangle = |\alpha|^2 \tag{3.14}$$

Recalling equation 3.9, we can link the number of photons to the amplitude of the quadrature. Moreover, we retrieve quadrature amplitude in the parameter A obtained from the fit of equation 3.11. With these considerations, the number of photons is:

$$\langle\hat{n}\rangle = \frac{|A|^2}{2} \tag{3.15}$$

In order to do a comparison, we estimate the photon number also by means of power considerations. In particular, given the average energy of a photon produced by our laser, we can measure the power of the signal beam blocking the local oscillator just before the detection system. From this information, known the laser repetition rate, we can retrieve the energy of a laser pulse and hence the pulse total photon number:

$$n_{ph\ tot} = \frac{P_{tot}[J/s]}{6.2\ 10^{18} R\ E_{ph}[eV]} \tag{3.16}$$

where P_{tot} indicates the power of the signal beam expressed in J/s, R the laser repetition rate and E_{ph} the average energy of a photon in eV.

Anyway, this is the total amount of photons in the laser pulse and the quadratures we measure are the single mode ones. Therefore, we estimate the number of photons of the pulse central mode by shaping the pulse. For this purpose, we send to the SLM a gaussian pattern[7] in order to obtain a narrow band pulse. With this shaping we're able to measure the power of the single central mode P_{peak} and then retrieve the central number photon peak:

$$n_{ph\ peak} = \frac{P_{peak}}{P_{tot}} n_{ph\ tot} \tag{3.17}$$

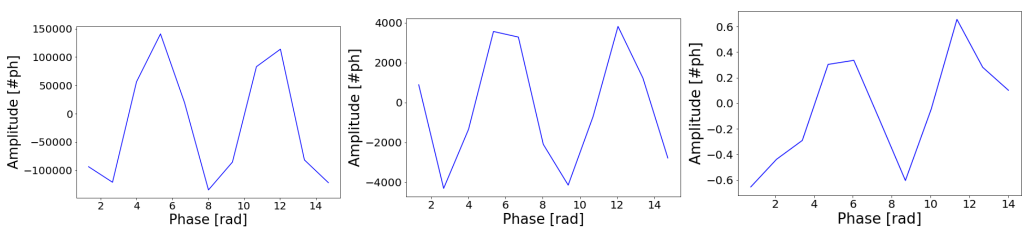

(a) filtering 1 10^3 (b) filtering 3 10^4 (c) filtering 3 10^7

Figure 3.10: single mode quadratures acquired in different filtering conditions.

In order to perform some photon number estimations, we acquire heterodyne data with various filtering configurations. In particular, we use a combination of filters to reduce the signal by 10^3, 3 10^4 and 3 10^7 times. Table 3.2 rpesents the comparison of the photon number estimations obtained with the two methods. Data were acquired with the photodiodes arrays detection system.

[7] We recall that this is the pattern we used for the SLM frequency calibration (figure 2.9b).

filtering	Power method	Quadrature method ($\eta_{eq} = 1$)	Quadrature method ($\eta_{eq} < 1$)
1x10^3	123024	2594	7202
3x10^4	2156	62	117
3x10^7	1.11	0.16	0.47

Table 3.2: estimations performed on quadratures acquired with the arrays detection system for three different filtering configurations. We notice that the quadrature method returns always a smaller value than the one provided by the power method. Moreover, that value gets closer to the power method one if the real η_{eq} is taken into account. As pointed out in [7], this effect can be explained by the presence of a photon dependent electronic noise.

The results of table 3.2 show that the estimations performed with the quadrature fit are always lower than the ones obtained from the power measurements. This happens both in the case of an ideal detector with $\eta_{eq} = 1$ and of a real one with $\eta_{eq} = \eta\eta_{pd}$. We notice that the latter returns a higher value compared to the ideal case. This underestimation with the quadrature method was already observed in [7] and was explained by the presence of a photon dependent electronic noise. Considering what we obtained with the shot noise linearity test (figure 3.4a), we find this hypothesis reasonable also in our case.

Moreover, we compare the estimation in the case of high filtering[8] for datasets acquired with different detection systems. Results are reported in table 3.3.

detector	Power method	Quadrature method ($\eta_{eq} = 1$)	Quadrature method ($\eta_{eq} < 1$)
arrays	1.11	0.16	0.47
diff. detector	1.30	1.06	1.20

Table 3.3: comparison of the mean photon number estimations of two equal quadratures acquired with different detection systems. We retrieve that differential detector data, due to the low electronic noise, have a better agreement with the estimations obtained from power considerations.

We see that the differential detector estimations performed with the quadrature fit are in good agreement with the ones obtained from the powers. As expected, the case with $\eta_{eq} < 1$ returns a higher value, since the electronic noise dissipation is taken into account. The comparison with the arrays estimation suggests that electronic noise affects heavily the quadrature fit estimation, even when the real value of η_{eq} is used.

[8] i.e. with the filtering configuration of 3 10^7.

Chapter 4

Multimode time domain heterodyne detection study of coherent phononic oscillations in $\alpha-$quartz

In Chapter 2 we have shown the potentiality of our set-up to retrieve the full structure of an optical pulse, in both its phase and amplitude features for each spectral component.

In this Chapter we want to exploit this peculiar feature to address the coherent evolution of lattice vibrations in solid state systems. The typical approach in this sense is the pump-probe one that consists in injecting in the system a large number of vibrational excitations by means of an ultrashort light pulse (pump). Subsequently the system optical response is investigated with a second pulse (probe) impinging at a variable time delay. The modification of the probe spectral features as function of the delay from the sudden excitation will carry information on the evolution dynamics of the excited modes.

We underline that the time resolution of the pump-probe experiment is shorter than the intrinsic phonon period[1]. Therefore our technique is phase-resolved for what concerns atomic coherent oscillations.

While in standard pump-probe spectroscopy the optical observable is the probe intensity, with our innovative set-up we are able to retrieve each probe mode response in both its phase and amplitude. This is important because amplitude and phase can encode qualitatively different information.

We underline that, thanks to the shot by shot pulse acquisition, we also have access to the full statistics of the emitted field. However, in this Chapter we will only focus on probe phase and amplitude mean value dynamics. The latter are obtained by averaging the heterodyne currents acquired on $2\ 10^3$ repetitions.

By means of this mean value approach, we will investigate the presence of coherent phonons in the time domain response of $\alpha-$quartz. We use this crystal since no electronic transitions are dipole allowed within the pump or probe bandwidth. This enables us to treat probe–matter interaction as an effective photon–phonon coupling and hence to find in the probe spectral features direct signature of the phonon.

Since we focus on mean values, we do not need to achieve the best signal to noise ratio possible[2] and hence photodiodes arrays suffice for our purposes.

[1] Our experimental resolution is determined by the pump translation stage step (approximately 10 fs), while phonons we study present periods of hundreds of femtoseconds.)

[2] That we recall, we obtain when employing differential detector.

4.1 Mean value maps

In this section we present mean value maps that we obtain from Multimode Heterodyne Detection of the probe pulse. This is done in order to study excitation[3] dynamics in an $\alpha-$quartz crystal.

In particular, we recall that we acquire an heterodyne trace for a certain pump delay, phase delay and pulse frequency, and all these parameters are independent. For every values combination of these three parameters, we acquire the entire pulse train. However, in this Chapter we treat only the responses averaged over the pulse train. Fluctuation studies, where the data statistics is taken into account, are presented in Chapter 5.

Single frequency maps

As we mentioned in previous paragraph, after exciting an $\alpha-$quartz sample with a pump pulse, we acquire a set of heterodyne currents as a function of pump delay, phase delay and pulse frequency. The independent variation of these parameters allows us to study different features:

- varying the pump delay (that we recall, represents the time interval between the system excitation and its investigation), we reconstruct the excitation temporal evolution
- varying the phase delay between signal and local oscillator (figure 2.2a) enables us to measure quadrature oscillations and hence to retrieve both amplitude and phase of the electric field
- acquiring independently each pulse frequency allows us to address different behaviors of the single mode quadratures across the pulse spectrum

Before we present some mean value results, we have to recall that a chopper is inserted along the pump optical path (figure 2.3). This is very important because it enables us to have a reference response, that is the equilibrium system[4] one. Indeed, tuning properly the chopper rotation frequency, we are able to selectively stop the pump pulse and hence acquire, for every probe pulse that interacted with the excited system, also a reference heterodyne current of the equilibrium one.

We now present some typical maps obtained for a fixed pulse frequency. In particular figure 4.1 reports the time evolution of a single mode quadrature for the equilibrium system (a), for the excited one (b) and the difference of the two responses (c). Each of the obtained maps exhibits the temporal evolution along the horizontal axis and the different quadrature phases along the vertical one. We underline that similar mean value maps are obtained for the whole pulse spectrum frequencies.

It is interesting to notice that the difference map (c), a part from an increasement of the response in correspondence of the overlap, at positive times[5] exhibits some oscillating features that gradually vanish. As we'll see with further analysis, these oscillations are a signature of the phonon presence.

[3] We recall that we induce excitation in the system by means of a pump pulse.

[4] i.e. a system where no pump pulse impinged.

[5] So after the pump excitation of the sample.

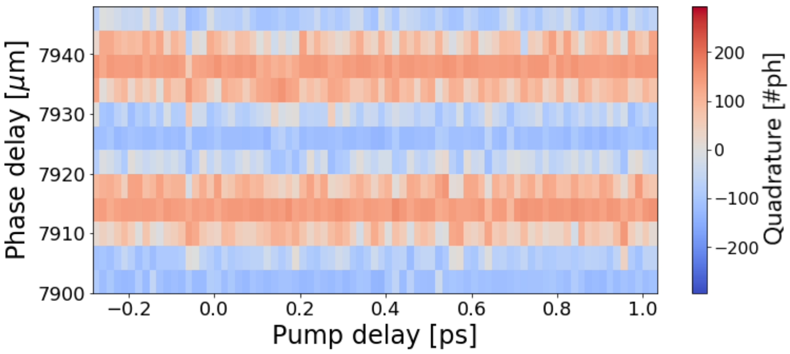

(a) equilibrium

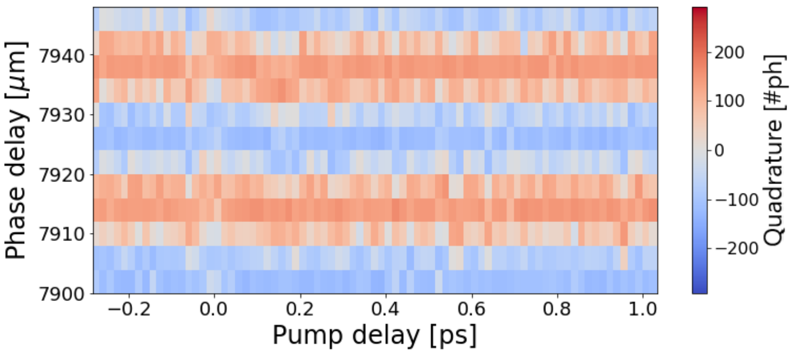

(b) pumped

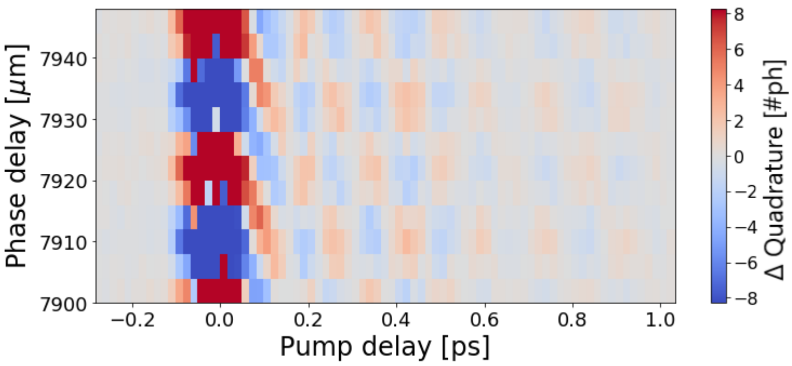

(c) pumped - equilibrium

Figure 4.1: mean value maps, for a fixed frequency, of the equilibrium system (a), of the excited one (b) and the difference between the previous two (c). Looking at the difference map (c), we retrieve the presence of oscillating features at positive times. As we'll see, this is a signature of the phonon.

4.2 Amplitude and Phase maps

In previous paragraphs we presented mean value maps of the single mode quadrature temporal evolution. We addressed some oscillating features (figure 4.1c) subtracting the equilibrium response from the excited system one, but we need a more practical way to retrieve the phonon presence. Moreover, we want to display separately quadrature phases and amplitudes, in order to appreciate a possible different response of the two observables.

For all these reasons, we introduce the so called *Amplitude* and *Phase maps* (figure 4.2). To obtain these maps we start from the of equilibrium and pumped mean value maps (figure 4.1). For each of these two maps, we perform a fit of the single mode quadratures[6]. Then, since maps 4.1a and 4.1b refer to a single frequency, we iterate the procedure for all the different pulse frequencies. The result is that we perform a fit of the single mode quadratures for every pump delay and every pulse frequency, both in the equilibrium and pumped case.

The reason we do these fits is that each fit returns us a value for the amplitude and for the phase of the single mode quadrature. So, we obtain a pair of amplitude and phase values for every frequency and pump delay. Finally, we subtract reference equilibrium amplitude and phase values from the pumped ones in order to address independently system variations for the two observables.

Figure 4.2 presents amplitude and phase maps obtained on an $\alpha-$quartz sample. Data were obtained employing pump and probe with linear parallel polarization [7].

Both maps present the periodic oscillation at positive times that we observed before (figure 4.1c). However, the two maps are qualitatively different. Indeed, phase map (figure 4.2b) shows a uniform oscillation for the whole frequency spectrum, whereas amplitude map unveils a different behavior between high and low frequencies. The fact that amplitude and phase provide different responses underlines the importance of acquiring both of them, and hence the utility of our phase resolved experimental setup.

In next sections, we investigate the origin of the different behavior encountered in the two maps.

[6]That, we recall, correspond to vertical slices of maps 4.1a and 4.1b.

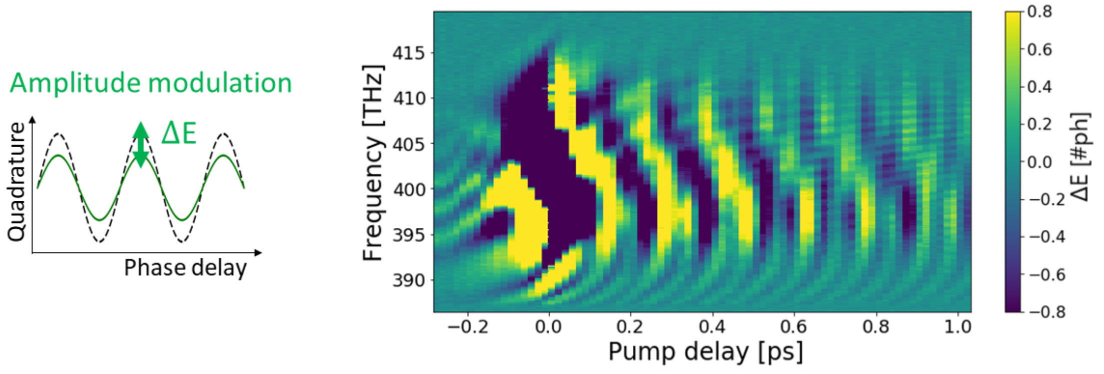

(a) Amplitude map

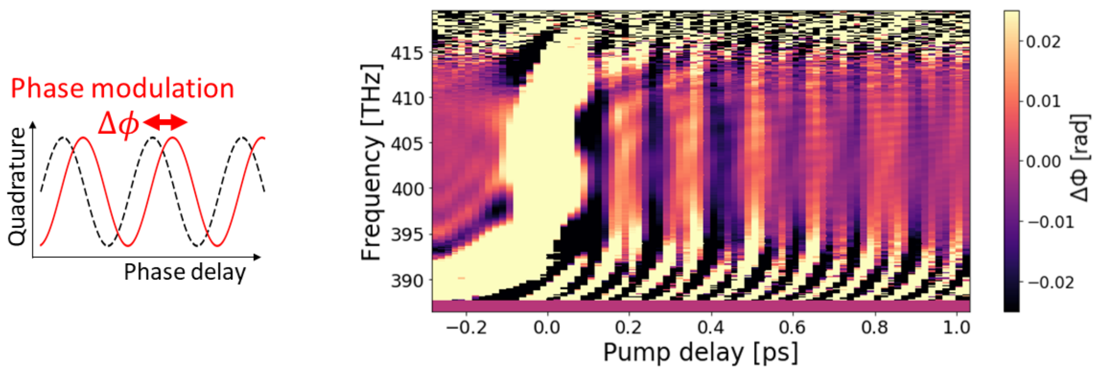

(b) Phase map

Figure 4.2: amplitude (a) and phase maps (b) obtained for an $\alpha-$quartz crystal. Both maps exhibit a periodic oscillation along the time axis that, as we'll see, is related to the presence of the phonon. However, amplitude and phase maps are qualitatively different. Indeed, phase map shows a uniform oscillation for the whole pulse spectrum, whereas amplitude exhibits different features between high and low frequencies.

4.3 Amplitude map: Impulsive Stimulated Raman Scattering

We start our analysis from the amplitude mean value map obtained with an $\alpha-$quartz sample (figure 4.2a). Amplitude map behavior can be summarized in the following way:

- we retrieve a periodic oscillation along the temporal axis for positive times, i.e. after the excitation of the pump.
- not all the frequencies behave in the same manner. Indeed, high and low frequencies oscillations are in anti-phase, i.e. when high frequencies exhibit a maximum, low frequencies have a minimum and vice versa

In next paragraphs we perform some studies of the Fourier Transformed map in order to link the periodic oscillation observed to the presence of phonons. Then we focus on the weight redistribution that occurs along the frequency axis.

4.3.1 Periodic oscillation: a phonon signature

In amplitude map we retrieve a periodic oscillation along the horizontal axis. In order to characterize this oscillation, we first perform some slices of the map to compare oscillations of different pulse spectrum regions. This is shown in figure 4.3.

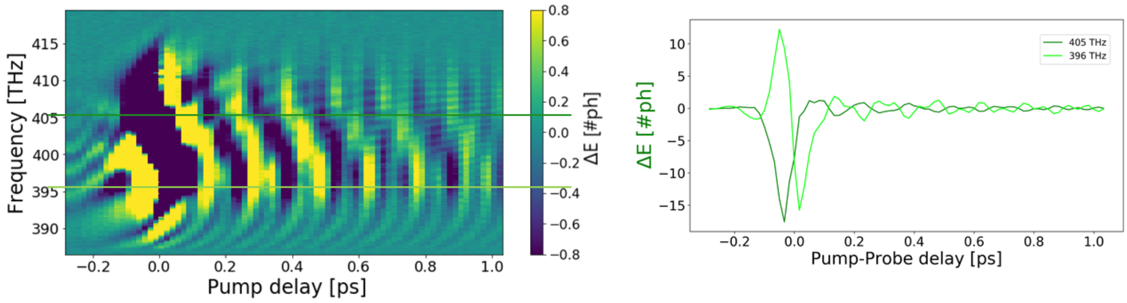

Figure 4.3: along the time axis we retrieve a periodic oscillation for both high and low frequencies. Performing some horizontal cuts unveils that the period of the oscillation is the same for the whole pulse spectrum and what changes is the phase of the oscillation. In particular, high and low frequencies oscillate in anti-phase

Horizontal cuts presented in figure 4.3 show that, even if the frequency behavior isn't the same for the whole pulse spectrum, the oscillation period doesn't change. Moreover, the feature that changes for high and low frequencies is the phase of the oscillation. In particular, high and low frequencies oscillations are in anti-phase.

Focusing on the oscillation period, we can exploit it to retrieve how much energy is stored in the oscillation and hence to address if it is linked to the presence of a phonon. For this purpose, we perform the Fourier Transform of the amplitude map along the horizontal axis. The result is depicted in figure 4.4.

Figure 4.4 shows the Fourier Transform amplitude map (left) and the FT mean graph obtained averaging spectra over pulse frequencies (right). In both cases, we clearly distinguish a peak at 6.2 *THz* and a smaller one around 15 *THz*. These values are in good agreement with characteristic phonon frequencies of the $\alpha-$quartz crystal [18], represented by black dashed lines in figure 4.4.

Therefore, the periodic oscillation that we retrieve in the amplitude map is nothing but the phonon generated in the $\alpha-$quartz crystal by the pump pulse. We underline that FT amplitude map (figure 4.4) exhibits the same peaks for the whole frequencies of the pulse spectrum. This confirms that the difference we retrieved in amplitude map resides in a phase shift and not in a different period of the oscillation.

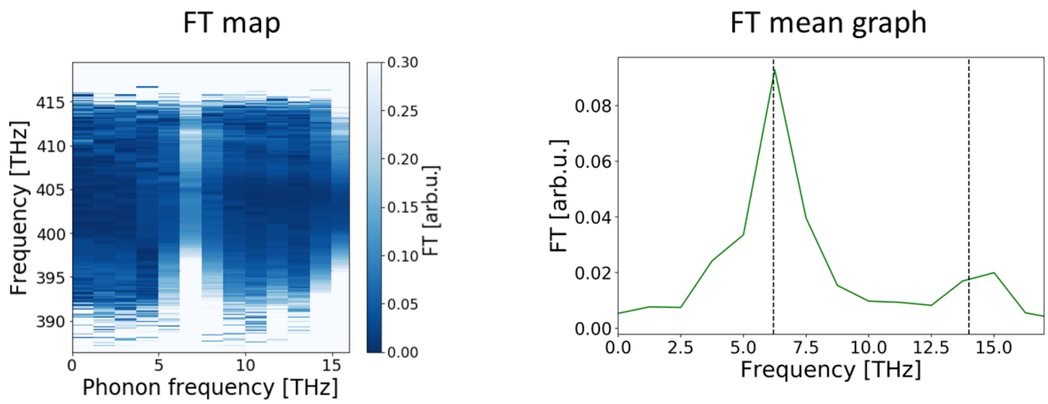

Figure 4.4: FT amplitude map (left) and graph of the FT averaged over pulse frequencies (right). We clearly see two peaks at 6.2 THz and 14 THz that match with $\alpha-$quartz phonon frequencies (black dashed lines). Thus, the periodic oscillation we saw in amplitude map can be attributed to the phonon generated inside the crystal by pump pulse.

4.3.2 Spectral weight redistribution via ISRS

Now that we have addressed periodic oscillations to the presence of phonons, we can focus on different behaviors retrieved between high and low pulse frequencies. In particular, we showed that the two pulse spectral regions oscillate in anti-phase (figure 4.3). This reflects in a redistribution of the pulse spectral content, as we can see performing vertical slices of amplitude map (figure 4.5).

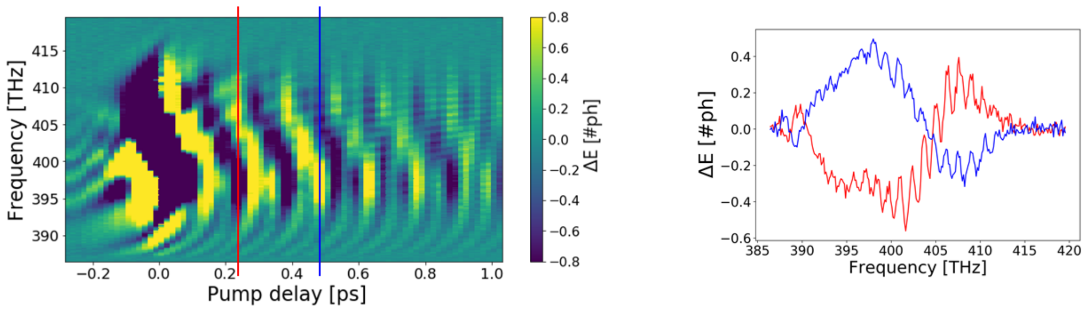

Figure 4.5: the anti-phase oscillations of high and low frequencies determines a redistribution of the pulse spectral content.

We underline that amplitude map is built doing the difference between quadrature amplitudes of the pumped system and of the equilibrium one. Thus, vertical cuts reported in figure 4.5 tell us that when low frequencies amplitude of the pumped system is lower than the equilibrium one[7], high frequencies amplitude is bigger (red line) and vice versa (blue line).

Therefore, the process that is taking place determines a redistribution of the spectral content inside the pulse. Moreover, this process is dependent on the phonon phase, since at different pump delays we see opposite redistributions (figure 4.5).

Impulsive Stimulated Raman Scattering

The physical process that explains the behavior retrieved is the so called *Impulsive Stimulated Raman Scattering* (ISRS) [19]. This phenomenon takes place when a spectral broadband light pulse impinge on a *Raman active medium*, i.e. a material that can absorb/release energy in order

[7] That means that map amplitude assumes values below zero.

to create/destroy a phonon. In particular, all photons couples that exhibit a difference in energy that matches phonon energy contribute to the process.

What happens is that a low/high energy photon is up-converted/down-converted into a high/low energy photon, destroying/creating a phonon. When a phonon is created, the process is called *Stokes*, while when the phonon is destroyed, the process is dubbed *Anti-Stokes*. A qualitative representation of ISRS is depicted in figure 4.6.

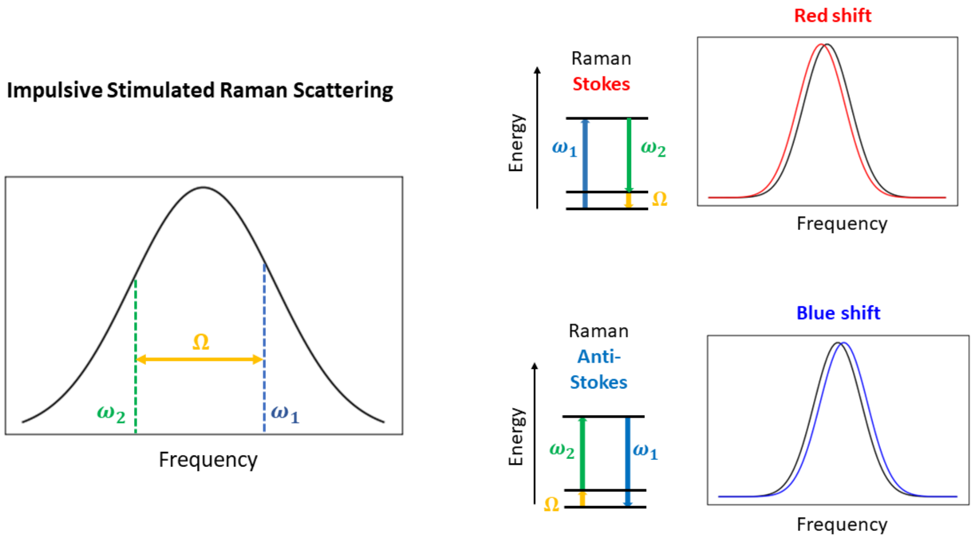

Figure 4.6: Impulsive Stimulated Raman Scattering (ISRS) occurs in Raman active media when the difference in energy of two pulse photons matches the excitation energy of a phonon. What happens is that a high/low energy photon is down-converted/up-converted into a low/high energy one, creating/destroying a phonon in the material. If the phonon is generated, the process is dubbed *Stokes* and determines a red shift of pulse frequencies. Otherwise, when a phonon is destroyed, the process goes under the name *Anti-Stokes* and is characterized by a blue shift of the pulse spectrum.

Moreover, photons up-conversion/down-conversion that occurs in ISRS Anti-Stokes/Stokes processes determines a shift of the pulse frequencies. In particular, when a phonon is created (Stokes process), pulse spectrum exhibits a red shift. On the contrary, when the phonon is destroyed, pulse frequencies experience a blue shift (figure 4.6).

ISRS to enhance/quench phonon oscillation

Spectral weight redistribution retrieved in figure 4.5 can be explained by blue/red shifts experienced by probe pulses that interact with the excited system with respect to the ones that impinge on the equilibrium one. This suggests that ISRS of probe pulses is occurring. However, spectral weight redistribution changes along the time axis, according to phonon oscillations. This is explained by the picture of ISRS depicted in [18].

When we impinge on the equilibrium system with the pump pulse, we create a phonon via ISRS. This phonon, characterized by atoms position and momentum, evolves as a quantum harmonic oscillator.

If probe interacts with the coherent vibrational state at a time when the atoms have the maximum momentum, the Stoke process dominates and high frequency photons are down-converted. On the contrary, if probe impinges when atoms are coherently moving with minimum momentum, a partial quench of the atomic motion can be triggered and the probe-phonon interaction is dominated by the Anti-Stokes process.

In conclusion, we address the different amplitude map behavior for high and low frequencies to the photon-phonon interaction that occurs between probe pulse and excited sample. The interaction

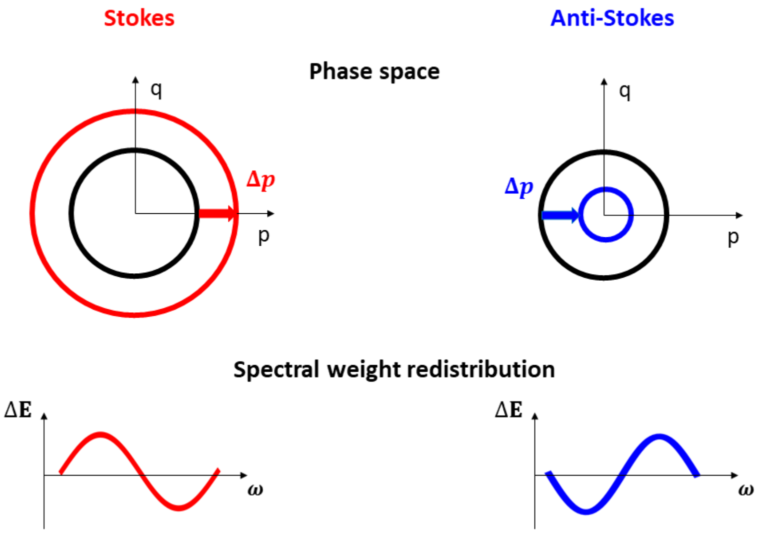

Figure 4.7: the occurrence of a Stokes/Anti-Stokes process depends on the phonon momentum when the interaction probe-phonon takes place. In particular, if the phonon momentum is maximum, then lattice vibration is favoured and a Stokes process occurs. This reflects into a red shift of the probe spectral content. On the contrary, if at the interaction time phonon momentum is minimum, lattice vibration is quenched by the Anti-Stokes process. This results into a probe blue shift.

is mediated by ISRS. Moreover, phonon oscillation can be enhanced (Stokes) or quenched (Anti-Stokes) according to the moving atoms momentum when the probe pulse impinges.

4.4 Phase map: Linear Refractive Modulation

After treating amplitude map, we can now focus onto the phase one. We recall the latter plots the difference in phase between the quadrature maps of the pumped system and of the equilibrium one.

As in the case of amplitude map, phase map exhibits periodic oscillations along time axis at positive times[8]. However, in this case[9] horizontal cuts of the map unveil that the periodic oscillation is uniform for different pulse frequencies (figure 4.8).

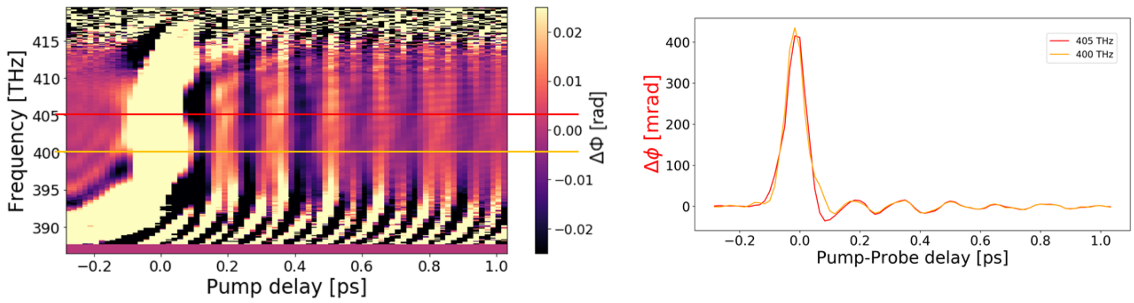

Figure 4.8: performing horizontal cuts of the phase map unveils that all the frequencies oscillate with the same period an phase.

Since amplitude map unveiled that periodic oscillations were linked to phonon presence, we decide to proceed with a Fourier Transform analysis also on phase map. Results are depicted in figure 4.9.

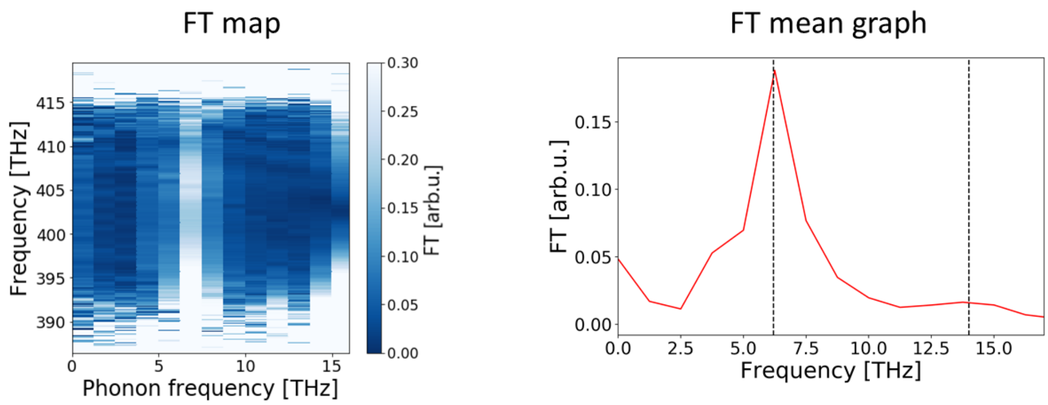

Figure 4.9: Fourier Transformed phase map and FT spectrum averaged over pulse frequencies. We retrieve a high peak at 6.2 THz ans a small one at 14 THz. They both match with characteristic $\alpha-$quartz phonons (black dashed lines).

Figure 4.9 presents the Fourier transformed phase map (left) and the FT spectrum obtained averaging over pulse frequencies (right). We clearly retrieve a peak in correspondence of 6.2 THz and a smaller one at 14 THz. As for amplitude map oscillations, these frequencies values match with the characteristic phonons of an $\alpha-$quartz crystal [18]. Therefore periodic oscillation along time axis is again a signature of the phonon presence.

[8]i.e. after the pump excitation occurred.

[9]We recall that amplitude map exhibits a non uniform behavior between high and low frequencies. The spectral weight redistribution that determines this asymmetry is caused by Impulsive Stimulated Raman Scattering.

4.4.1 Linear modulation of the refractive index (LRM)

Since oscillations retrieved in phase maps are uniform for the whole pulse spectrum, we expect a phenomenon different from ISRS to rule quadrature phase dynamics[10]. This phenomenon is the so called *Linear Refractive Modulation*.

Linear refractive Modulation (LRM) indicates the variation of a material refractive index due to a change in atoms position. Indeed, we can write refractive index, according to classical formalism [7], as:

$$n = \sqrt{n_0^2 + \frac{\delta \chi}{\delta q}\Big|_{q=q_0} q} \tag{4.1}$$

where n_0 and q_0 indicate respectively refractive index and atom position at equilibrium, χ is the electronic susceptibility and q is the position coordinate.

In our case, the position change is given by lattice phononic oscillations. Therefore, refractive index changes according to the lattice position coordinate.

We recall that ISRS driven amplitude map oscillation is related to the momentum of the phonon. Indeed, impinging probe enhances or quenches phonon oscillation when atoms momentum is respectively maximum and minimum (figure 4.7).

Since amplitude map oscillation depends on phonon momentum while phase map oscillation is ruled by phonon position, we expect a phase shift between amplitude and phase oscillations of $\pi/2$. We compare horizontal cuts performed on the two maps in figure 4.10.

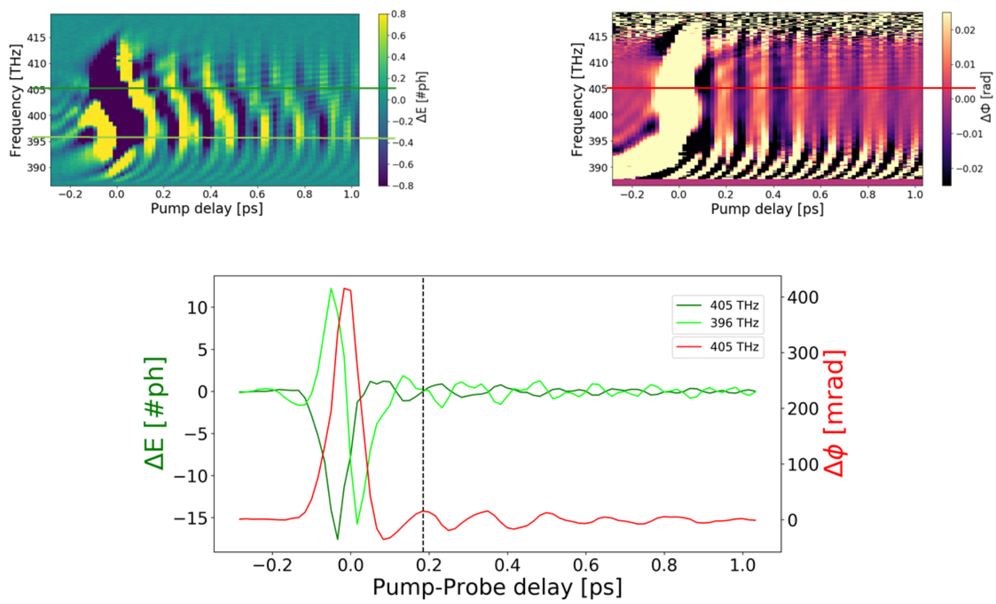

Figure 4.10: comparison of periodic oscillations retrieved in amplitude an phase maps. Recalling that in amplitude map high and low frequencies oscillate in antiphase, we see that amplitude and phase oscillations are $\pi/2$ shifted. This is linked to different phenomena observed. In amplitude map we observe ISRS effects on the probe pulse, while in phase map the most dominant effect is LRM. We underline that ISRS is determined by phonon momentum, while LRM is ruled by atoms position. Therefore, oscillations result $\pi/2$-shifted

Figure 4.10 shows that time dependence of the quadrature phase is $\pi/2$ shifted with respect to the amplitude oscillation. Since amplitude map is dominated by ISRS, and hence amplitude oscllations depend on phonon momentum, the $\pi/2$ shift confirms that phase response is ruled by phonon position. Therefore, what we observe is the effect of the linear modulation of sample refractive properties.

[10]Indeed, in previous section we saw that ISRS causes a spectral weight redistribution inside the pulse.

To end the Chapter, we provide a global picture of the phenomena observed [18]. A scheme is reported in figure 4.11.

First, when pump pulse impinges on the crystal, a phonon is created via ISRS. This phonon evolves in time like a quantum harmonic oscillator and hence is characterized by momentum and position coordinates. Subsequently, the probe pulse impinges on the excited sample. Since the phonon is evolving, different impinging times of the probe pulse will determine different scenarios:

- if at interaction time phonon has maximum momentum, the probe pulse interferes constructively with the lattice oscillation and amplifies it via ISRS. This results in a spectral weight redistribution of probe pulse towards low frequencies (red shift)
- if phonon momentum is minimum, probe interaction results in a quenching of the phonon oscillation. The energy that the light pulse subtracts at the excited system shifts pulse spectrum towards high frequencies (blue shift)
- if phonon momentum is null, energy transfer between probe pulse and phonon is negligible. In this case, the relevant effect is the modulation of the refractive index that we recall does not change the pulse spectral content

In this Chapter we exploited the capability of our setup to perform a phase and frequency resolved pump and probe experiment to study phonon dynamics in an $\alpha-$quartz crystal. In particular, we retrieved a different behavior between amplitude and phase dynamic response. Amplitude map exhibited a temporal oscillation characterized by a spectral weight redistribution, whereas phase map showed a uniform oscillation for the whole pulse spectrum. We addresed these features to respectively Impulsive Stimulated Raman Scattering and Linear Refractive Modulation.

We underline that amplitude and phase behavior proved to be ruled by different phenomena. Therefore, amplitude and phase carry qualitative different information. This highlights the importance of performing a measurement that resolves both the amplitude and the phase of the electric field, as provided by our setup.

In next Chapter, we will also exploit the shot by shot pulse acquisition of our setup. Indeed, this feature gives us access to the statistical degrees of freedom of the measurements and enables us to perform studies of fluctuation dynamics.

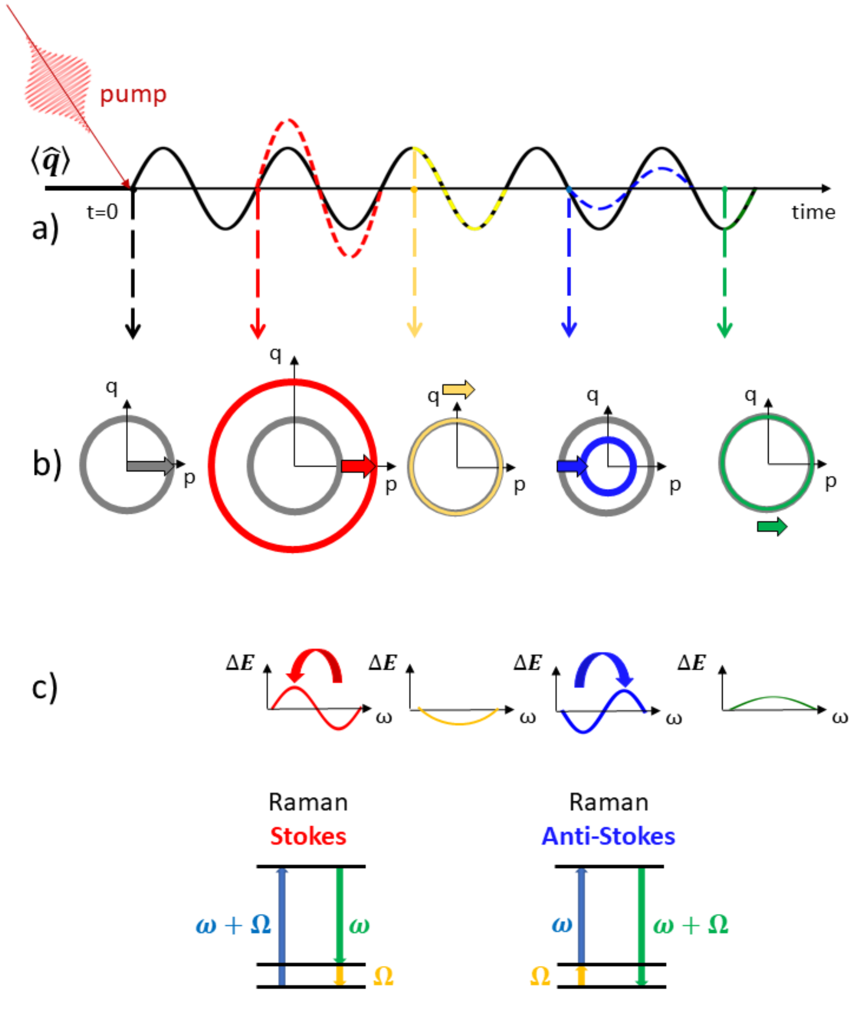

Figure 4.11: theoretical picture of the experiment. In a) we depict the mean phonon oscillations induced through ISRS by the pump at t = 0. In (b) we illustrate the modification of the phonon phase space trajectory due to the probe-target interaction. The ISRS probing effect is maximum when the phonon carries the maximum momentum modulus. Depending on the probing time, ISRS can either force (Stokes process) or dump (Anti-Stokes process) phonon oscillation. The first occurs when the probe interacts at the maximum phonon momentum, while the latter when the phonon exhibits at the interaction time the minimum momentum. As depicted in (c) Stokes and Anti-Stokes probing processes result respectively in a red shift or blue shift of the probe pulse. Conversely, at the extremes of the phonon oscillations the ISRS-driven amplitude shift is negligible and no change of the spectral weight occurs. In this case the dominating probing effect is the Linear Refractive Modulation.

Chapter 5

Generation of an incoherent superposition of quantum states

In the previous Chapter we exploited the capability of our experimental setup to perform phase sensitive and frequency resolved measurements to study the excitation dynamics in an $\alpha-$quartz sample. The results presented were obtained averaging every heterodyne trace (for each frequency, phase and pump delay) over many repetitions and looking at the mean values. By the way, our detection system provides a shot by shot pulse acquisition that enables us to study the fluctuations of the measurement (see section 3.1).

In this Chapter we present an experiment where the analysis of the fluctuation dynamics unveils a non trivial behavior. Moreover, the information encoded in the statistics isn't directly observable in the mean values, suggesting the importance of a study of the measurement fluctuations.

The experiment we present consists in a study of the *Second Harmonic Generation* (SHG) of the pump pulse in condition of resonance with the local oscillator (LO) pulse. We exploit these experiment to prove the statistical properties of light. In particular, we exploit the random relative phase between signal and idler to generate a superposition of phase randomized quantum states. Moreover, we exploit the phase stabilization system (CEP) to fix the phase relation between signal and idler and hence to remove the phase uncertainty of these quantum states.

In the following, we describe the experiment principles and some mean value results obtained. Then, we move to the fluctuation analysis, where we study the distribution of the measurement as a function of the quadrature phase, of the pulse frequency and of the pump time delay. Subsequently, we provide a model that explains the experimental evidences and we test it by employing the CEP. Finally, in order to perform some quantitative estimations, we introduce the *Pattern Function Quantum Tomography* technique and we apply it to the data acquired.

5.1 Second Harmonic Generation with a collinear resonant pump.

In Chapter 2 we described the setup that we use to perform a Multimode Heterodyne Detection experiment. Briefly summarizing, an initial beam splitter divides the laser beam into signal and local oscillator. The first impinges on the sample, previously excited by means of a pump pulse, and is then recombined with the local oscillator by a beam splitter. This is done in order to amplify the probe signal according to the relative phase between the LO and the probe. The two outcoming beams, arranged in a balanced configuration (section 2.3), are finally detected and the differential photon current is acquired. Focusing on the excitation process, we use as a pump pulse the idler produced by the OPA. Pump pulses have a tunable wavelength in the range of near-infrared.

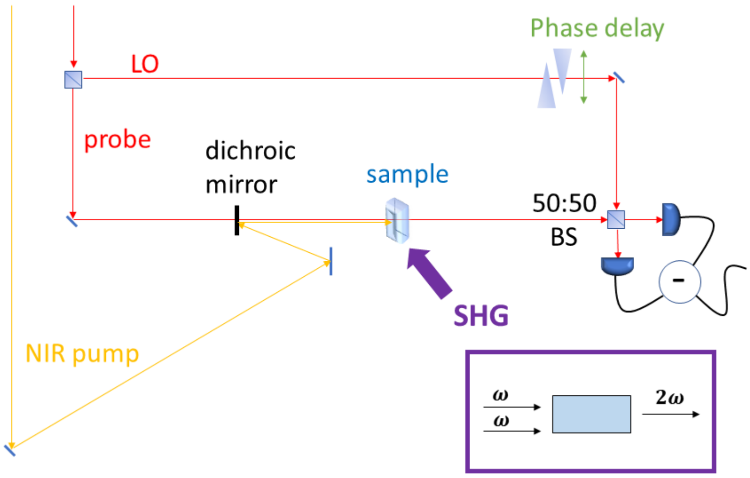

Figure 5.1: scheme of the setup with the collinear pump configuration used to perform Multimode Heterodyne Detection of the pump second harmonic. A dichroic mirror is used in order to reflect the pump beam and transmit the probe one. With this arrangement, pump and probe beams share the same optical path after the sample and can both be recombined with the LO in order to perform an heterodyne detection measurement. The pump second harmonic is generated in the sample by means of Second Harmonic Generation (SHG). As explained in section 1.2, heterodyne amplification process happens just for the frequencies residing in the range of the LO spectral band. Therefore, we tune the pump wavelength in order to have its second harmonic in resonance with the LO frequencies.

In figure 2.3 we showed a scheme where the pump impinges on the sample with an arbitrary angle of incidence. This isn't the only possible configuration. Indeed, for the measurements presented in this Chapter we use the so called *collinear configuration*, where the pump beam and the probe one impinge with the same angle on the sample (figure 5.1). For this purpose we use a dichroic mirror[1], i.e. an optical element that selectively reflects some colours and transmits the others. In particular, we employ it to transmit the probe beam and to reflect the pump beam determining its orientation. With the collinear configuration, two goals are achieved:

- the interaction between the probe and the excited sample is maximized
- the pump pulse shares the same optical path of the probe beam after the sample

We underline that, in standard pump and probe experiments, it is preferable to send the pump beam far away from the probe optical path in order to block it and avoid it to enter in the detector. Otherwise, if some pump light is detected, the measurement would be affected by an unpredictable noise possibly creating some artifacts. However, relying on the different wavelengths of pump and local oscillator/probe pulses, we can send the pump on their same optical path and subsequently block it with a proper filter.

[1]We use the commercial dichroic mirror *dmsp1000* produced by Thorlabs.

In this experiment we're interested in performing a Multimode Heterodyne Detection measurement of the pump, and in particular of its second harmonic. This interest resides in the random phase relation between the pump pulse and the LO one. As we'll see, this feature, intrinsic in the pulse creation process, gives rise to a superposition of random phase states that can be unveiled just by fluctuation studies.

To generate the pump second harmonic, we exploit the Second Harmonic Generation that occurs in the sample. SHG is a process that occurs in non linear crystals where two photons of energy $\hbar\omega$ are upconverted in a photon of energy $2\hbar\omega$ (figure 5.1). Moreover, we're able to generate the second harmonic also with low conversion efficiency[2] samples (for example $\alpha-$quartz).

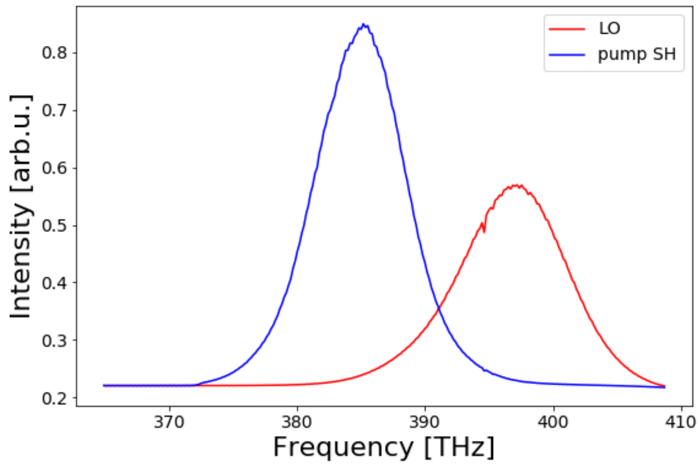

Figure 5.2: plot of the LO pulse spectrum and of the pump second harmonic one acquired with a commerical spectrometer. We tuned the pump pulse frequency in order to have an overlap region (visible between 387 *THz* and 395 *THz*) with the LO spectrum. In this way, we're able to perform Multimode Heterodyne Detection of the pump second harmonic.

To perform Multimode Heterodyne Detection of the pump second harmonic, some other conditions must be fulfilled. In particular, we saw (Chapter 1) that the amplification process operated by the LO occurs just for the frequencies in the range of the LO spectral band. Therefore, we have to tune properly the pump wavelength so that its second harmonic is resonant with the LO. In figure 5.2, the intensity spectra of the LO and of the pump second harmonic are plotted. We see that in the region of 387-395 *THz* there is an overlap between the two pulses. Therefore, we expect the heterodyne amplification to occur in this region.

[2]With *conversion efficiency* we indicate the ratio between the number of second harmonic photons 2ω produced and the number of incoming photons ω.

5.2 Mean value study on a Beta Barium Borate crystal (BBO)

In the previous section we introduced the basic principle of the experiment, that is performing Multimode Heterodyne Detection of the pump pulse second harmonic, where the latter is generated by means of Second Harmonic Generation (SHG) in the sample. To achieve this goal, we use a Beta Barium Borate crystal (BBO), a widely employed material for SHG processes because of its high conversion efficiency. Moreover, we stop the signal (similarly to what we did for the vacuum state measurements, figure 3.3) right before the sample in order to study the heterodyned pump second harmonic alone.

As a preliminary study, we look at the set of 200 heterodyne traces acquired for fixed pump and phase delay with the arrays detection system. In figure 5.3a, the heterodyne traces of two consecutive pulses are reported. We clearly see that the differential current exhibit some interference fringes, linked to the interaction between the pump second harmonic and the LO pulse mediated by the sample. Comparing the two traces, we see that these fringes heavily change their position, giving rise to a completely different current profile. If we look at the whole data set (figure 5.3b), the same behavior is encountered. In fact, the coloured dotted background, representing every single heterodyne trace, covers almost uniformly a large range of values. This indicates that interference fringes experience a random shift at every pulse, resulting in randomly shaped differential currents. Looking just at the heterodyne trace averaged over the 200 pulses set (black line in figure 5.3b), we see that it's almost zero for every frequency (as expected for a balanced configuration). Moreover, we can't retrieve the presence of fringes and most importantly we loose completely the random shift information.

We underline that the random shift of the fringes is qualitatively different from a standard detector noise. In fact, the latter determines a change in the differential current values preserving the general shape, and hence the fringes positions. On the contrary, the measured heterodyne traces experience a fringe shift at every pulse.

The evidence of information loss suggests that a mean value analysis, like the one adopted in Chapter 4, isn't suited for this kind of data. Therefore, we move towards a statistical approach, looking at the fluctuation dynamics of the experiment.

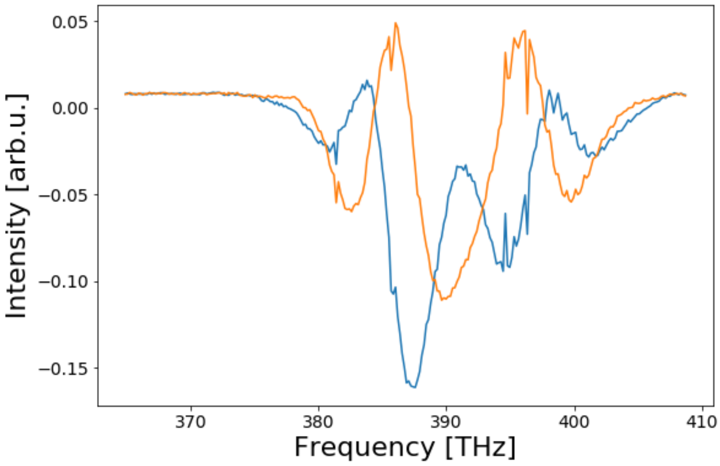

(a)

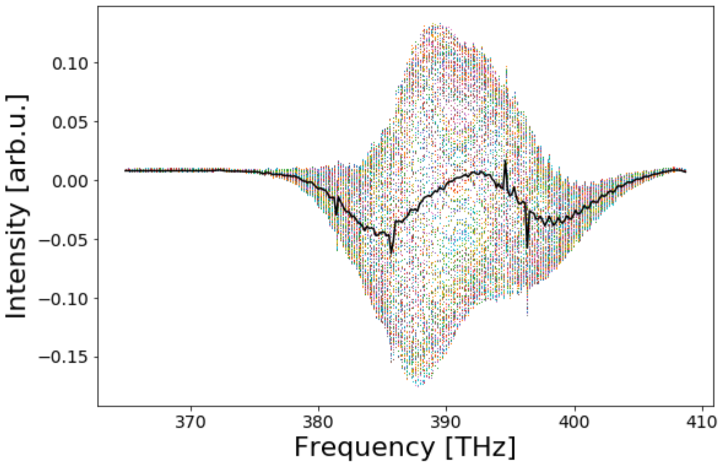

(b)

Figure 5.3: this panel summarizes the macroscopic heterodyne trace behavior encountered in the experiment. The first picture (a) shows the measured heterodyne trace of two consecutive pulses (blue and orange) for given pump and phase delays. We clearly see that there are some interference fringes that heavily change in the two cases. Moreover, if we look at figure (b) we see that the dotted background, representing the heterodyne traces of the whole 200 pulses train, covers almost uniformly a great range of values. Therefore, there is a sort of random shift of the fringes that occurs for every pulse. If we look at the resulting mean trace (black line), we see that it's almost zero and definitely doesn't describe the shifting fringes. This evidence proves the necessity of moving towards a fluctuations study.

5.3 Distribution Study of the pump second harmonic heterodyne trace

The standard approach adopted to analyze a Multimode Heterodyne Detection experiment consists in studying the heterodyne traces averaged over the entire pulse train. We presented an example of mean value study in Chapter 4. However, this approach isn't fit for every measurement. In the previous section, we presented the results obtained for Multimode Heterodyne Detection of the pump second harmonic (figure 5.1). In particular, we showed that each single pulse heterodyne trace exhibits interference fringes that are randomly shifted at every acquisition (figure 5.3). Of course, an average over the pulse train cancels completely this behavior, causing a loss of information. For this reason, we perform a statistical analysis of the measurement.

Since our setup provides the arbitrary control of many different parameters (pump delay, phase shift, pulse frequency), in the following paragraphs we present the results obtained varying the parameters one by one. In particular, we study the measurement distribution as a function of the quadrature phase, of the pulse frequencies and of the pump time delay.

We study both a BBO and an $\alpha-$quartz sample. We underline that $\alpha-$quartz crystal has a low conversion efficiency for the Second Harmonic Generation process. However, our low noise detection configuration is so powerful that we're able to perform a fluctuation study of the pump second harmonic. Therefore, the BBO data were acquired with the arrays detection system, while the $\alpha-$quartz ones with the differential detector. In the end, we study the effects on the distribution determined by a change in the pump power and by the employment of the pulse phase stabilization system (CEP).

5.3.1 Distribution vs quadrature phase

The first parameter that we vary is the relative phase between the signal and the local oscillator[3]. In order to discriminate the features introduced in the measurement distribution by the pump second harmonic, we need a reference distribution. For this purpose, we start our analysis from a study of the local oscillator alone. To do so, we stop both the pump and the signal. The result is what we call a vacuum state measurement (figure 3.3).

Vacuum state

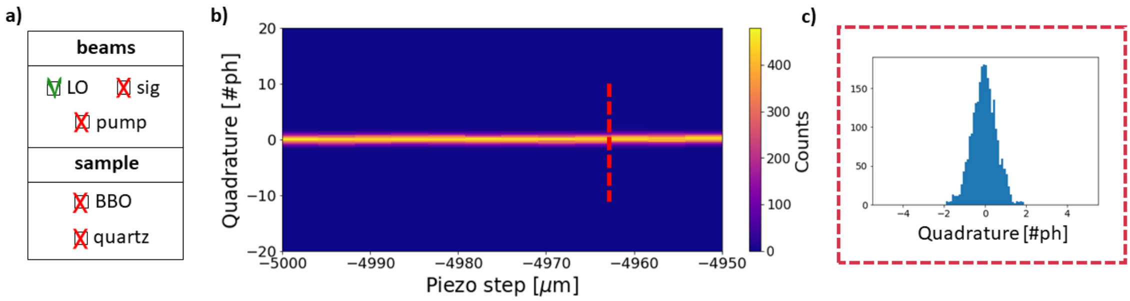

Figure 5.4: Table (a) summarizes the experimental conditions in which the heterodyne trace is acquired. In particular, it specifies the beams that are measured and the sample used. The histogrammatic plot of the vacuum state trace is presented in (b). On the horizontal axis the different quadrature phases are displayed, while on the vertical axis the measurement distribution is presented by means of histograms (c). We see that the measurement distribution of the vacuum state is peaked on the zero value and has a gaussian profile that doesn't change with the phase.

In figure 5.4 we present the measurement distribution of the LO alone acquired with the differential detector. Figure (b) is what we call a *histogrammatic plot*. The horizontal axis shows

[3]We recall that acquiring the heterodyne traces for fixed frequency and pump delay means measuring a single mode quadrature.

the quadrature phase[4], whereas the vertical axis plots the quadrature value distribution. This is achieved by building an histogram of the measured values for every piezo step (b).

The first thing we notice in the vacuum state distribution (figure 5.4) is that, for each piezo step, the distribution is peaked on the zero value and has a gaussian shape (c). The zero value peak is determined by the fact that vacuum state trace is nothing but a quadrature with zero amplitude, while the distribution profile is linked to the random photon number fluctuations. Moreover, the measurement distribution exhibits no phase dependence. This seems reasonable since both vacuum state trace and its variance exhibit no phase dependence (equation 3.7). Summarizing, the LO measurement distribution has a gaussian profile peaked on zero with a constant width.

Pump second harmonic heterodyne trace

Now that we have a reference measurement distribution, we add the pump to the experiment, leaving the signal beam closed. This is done in order to isolate the pump second harmonic effects. The results discussed in the following are obtained with an $\alpha-$quartz sample[5] and using the differential detector.

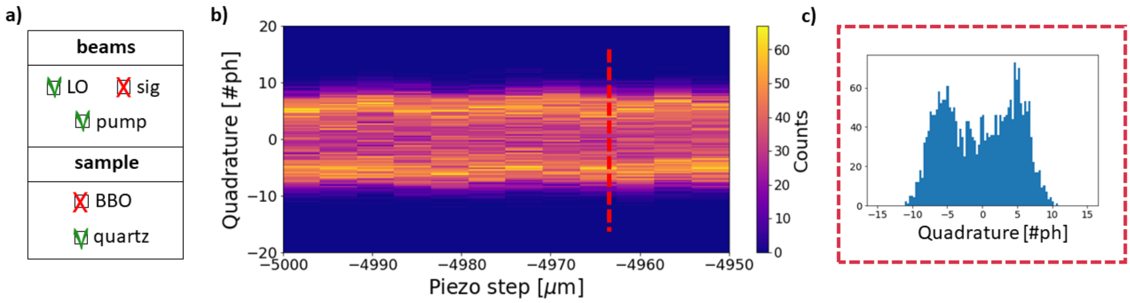

Figure 5.5: distribution of the pump second harmonic heterodyne traces (a) acquired for different phases (b). The frequency is fixed at 396 THz, a value that lays in the overlap region between the pump second harmonic and the overlap. The pump delay is chosen to be in the proximity of the temporal overlap between the pump and the signal. The measurement distribution obtained exhibits a pair of symmetrical peaks, with a valley in correspondence of the values around zero (c).

Figure 5.5 shows the histogrammatic plot of the pump second harmonic heterodyne measurement. To obtain it, we chose a pump delay in proximity of the temporal overlap and a frequency residing in the LO-pump second harmonic overlap region (figure 5.2). In particular, we select the frequency of 396 THz. What we see in figure 5.5 is qualitatively different from the gaussian distribution of the vacuum state (figure 5.4). Indeed, the heterodyne measurement of the pump second harmonic exhibits a bimodal distribution, with two symmetrical peaks and a valley in correspondence of values around zero. Even if there seems to be a modulation, deeper analysis didn't unveil a clear phase dependence of the distribution.

Signal + pump second harmonic heterodyne trace

Since we have seen the effect of the pump second harmonic alone on the heterodyne trace, we can now add the signal in order to see how the contributions combine[6].

Figure 5.6 shows the measurement distribution of the signal+pump second harmonic heterodyne trace. Same frequency and pump delay of figure 5.5 are used. We see that the two symmetrical peaks of the bimodal distribution are still present. The only sensible change from the pump second harmonic alone heterodyne trace is the presence of a phase oscillation. This is due to the signal and the oscillation that we see is the quadrature one. In conclusion, opening the signal doesn't change the bimodal feature of the distribution, but just shift it according to the phase delay.

[4]We recall that every piezo step is associated to a different quadrature phase.

[5]We underline that the vacuum state measurement is independent from the sample choice, since no beam interacting with the sample enters in the heterodyne current

[6]Measurements are also in this case performed on the $\alpha-$quartz sample.

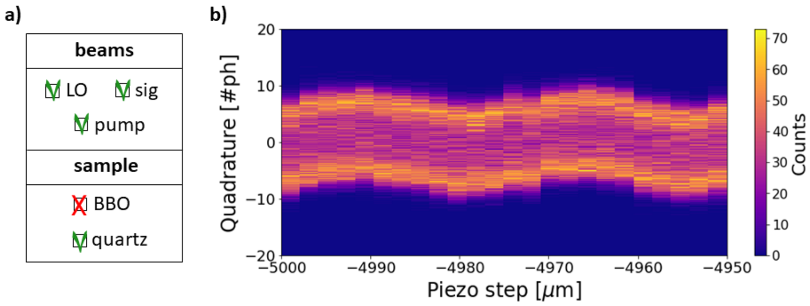

Figure 5.6: distribution of the signal+pump second harmonic heterodyne trace (a-b). The choice of the frequency and pump delay parameters is the same as in figure 5.5. We retrieve also in this case the presence of a bimodal distribution, characterized by two symmetrical peaks. The difference resides in the phase oscillation of the data that we link to the quadrature oscillation.

BBO sample

All the previous results were obtained with an $\alpha-$quartz sample, a material that we've already characterized with mean value measurements (Chapter 4). However,the Second Harmonic Generation process we use to generate the pump second harmonic can occur in a more efficient way in many other crystals, like a Beta Barium Borate (BBO) one.

To discriminate if the bimodal distribution is linked to the sample choice, we then generate the pump second harmonic with a BBO crystal and we perform heterodyne detection of the pump alone (i.e. no signal). Since BBO sample provides an efficient Second Harmonic Generation process, differential detector isn't necessary. Therefore, data are acquired with the arrays detection system.

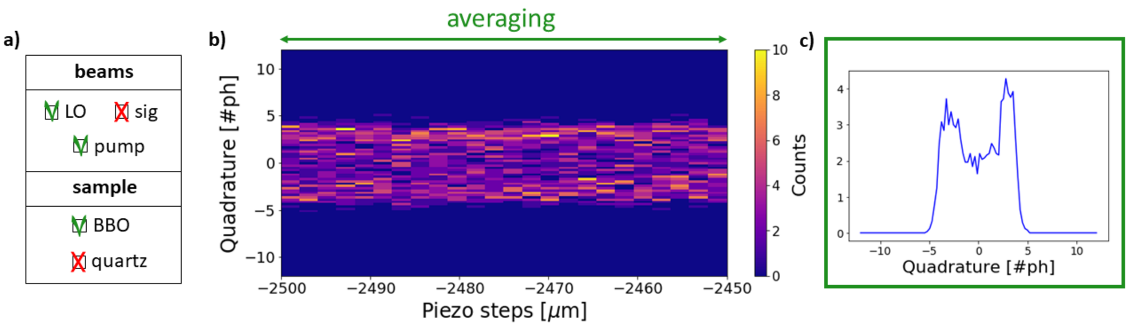

Figure 5.7: distribution of the pump second harmonic heterodyne trace generated by a BBO crystal (a-b). Data are acquired with the photodiodes arrays. With respect to the $\alpha-$quartz data, the histogrammatic plot shows a less clean bimodal distribution. However, averaging over the different phases (since no phase dependence is detected in the absence of signal) we can unveil the presence of the two peaks (c). We attribute the worse visibility of the bimodal distribution to the high electronic noise characteristic of the arrays detection system.

Figure 5.7 shows the histogrammatic plot of the pump second harmonic heterodyne trace (same as in figure 5.5). We notice that the presence of the bimodal distribution is less evident for the single phase histograms with respect to the $\alpha-$quartz data. However, if we average histograms over the different phases, we clearly see that the two peaks are still present (c).

We attribute the different visibility of the peaks to the arrays detection noise, that we recall is heavily affected by electronic noise (figure 3.4).

Pump second harmonic distribution

Until now we have always looked at the measurement distribution of the heterodyne traces, i.e. in the presence of the local oscillator reference beam. However, we haven't still characterized the pump second harmonic distribution alone. This has to be done in order to understand if the characteristic bimodal distribution of the pump second harmonic heterodyne trace is due to the second harmonic distribution or to something else. Therefore, we stop both the signal and the local oscillator and measure the pump second harmonic generated by the $\alpha-$quartz sample[7]. We underline that, since the LO is blocked, no phase dependence could be present.

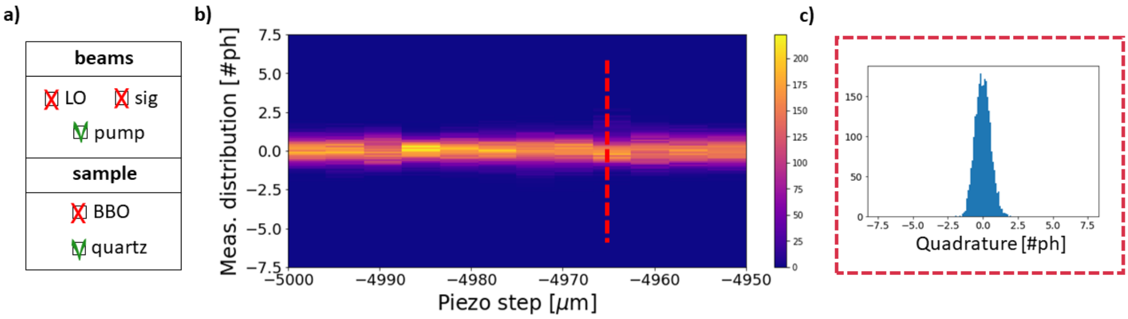

Figure 5.8: distribution of the pump second harmonic alone (a-b). The distribution exhibits a single peak on the zero value and has a gaussian profile (c). Therefore, we can't link the bimodal distribution of the pump second harmonic heterodyne trace to the one of the second harmonic alone. We underline that no phase dependence is retrieved: this is reasonable, since the LO oscillator is stopped and therefore the concept of phase delay looses its meaning.

The histogrammatic plot of the pump second harmonic trace is presented in figure 5.8. The measurement distribution is definitely single peaked on the zero value and has a gaussian profile. According to what we expected, no phase dependence is detected. Importantly, we can't attribute the bimodal feature of the pump second harmonic heterodyne trace to the second harmonic distribution.

In conclusion, when we measure the pump second harmonic heterodyne trace we find a bimodal distribution. This distribution exhibits two symmetrical peaks and has a valley in correspondence of the central values. On the contrary, if we measure the LO or the pump second harmonic alone, we get a gaussian shaped distribution peaked at the center. The addition of the signal doesn't affect the shape of the double peak, but just shifts it according to the quadrature oscillation. Finally, the presence of the bimodal distribution occurs with both the $\alpha-$quartz and the BBO samples.

[7]Since we use the $\alpha-$quartz sample, we acquire the data with the differential detector.

5.3.2 Distribution vs pulse frequencies

In the previous section we unveiled a bimodal distribution in the pump second harmonic heterodyne measurement. This double peaked distribution arises in the presence of the pump second harmonic but isn't determined by the second harmonic distribution itself. In order to understand the origin of this behavior, we decide to perform the following analysis. Since the distribution, in the absence of signal, seems to be phase independent, we can fix an arbitrary phase and vary other parameters. In this section we present the results obtained varying the frequency for both the $\alpha-$quartz and the BBO samples.

Vacuum state

In order to have a reference result, we first look at the measurement distribution of the vacuum state (i.e. the LO alone). To study the distribution, we choose an arbitrary phase, since no phase dependence is present, and a pump delay in proximity of the temporal overlap. The vacuum state histogrammatic plot as a function of frequency is depicted in figure 5.9.

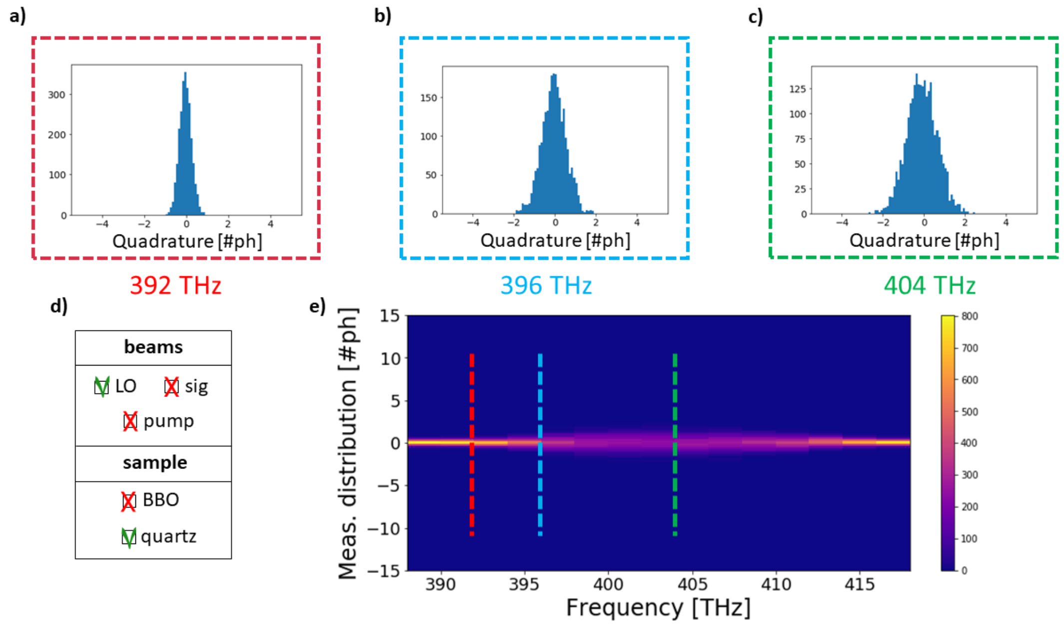

Figure 5.9: distribution of the vacuum state trace (d-e). The distribution preserves a gaussian profile for the whole frequency scan. The only clear change is an enlargement of the distribution in the correspondence of the LO pulse central frequencies (a-b-c). This behavior is explained by the dependence of the shot noise from photon number of the LO modes.

The measurement distribution of the vacuum state, as expected, remains single peaked with a gaussian profile for the different frequencies (figure 5.9). The feature that clearly changes through the frequency scan is the width of the distribution. In particular, the gaussian FWHM exhibits a maximum around 402-404 THz and then gradually decreases, both in the higher and lower frequencies directions. If we compare the region of frequencies were the distribution spread has an enhancement with the LO spectral content (figure 5.10), we see that there is match: the highest distribution spread is in correspondence of the LO pulse central frequencies.

This can be easily explained if we look back at the shot noise measurements performed in Chapter 3. In fact, we showed that the variance of the vacuum state depends on the LO number of photons, and in particular grows if the photon number increases. Moreover, variance is an indicator of the measurement distribution width. Combining these two considerations, we can attribute the enlargement of the measurement distribution for the LO pulse frequencies to the typical shot noise behavior.

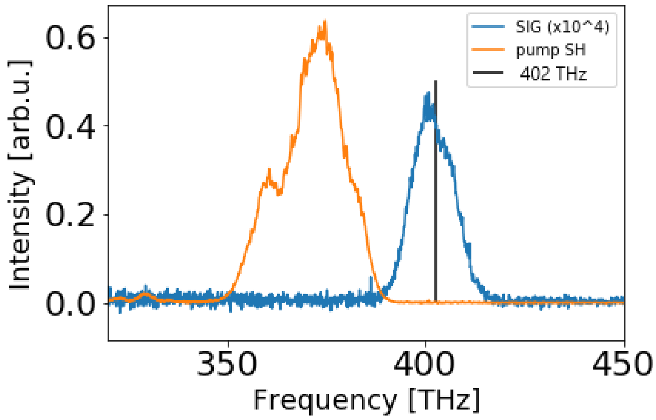

Figure 5.10: spectra of the pump second harmonic and of the signal. We recall that signal and LO come from the same beam and therefore have the same spectral content. In addition, we underline that the frequencies of the two pulses are slightly different from the ones used for the BBO measurement (figure 5.2).

Pump SH + LO using an $\alpha-$quartz crystal

Since we have characterized the vacuum state distribution, we can add the pump in order to study the pump second harmonic heterodyne trace.

We start the analysis from the $\alpha-$quartz sample. We recall that, due to the low conversion efficiency of this crystal, we have to use the differential detector in order to measure the pump second harmonic heterodyne trace. Moreover, we're interested in characterizing the bimodal distribution and not the signal quadrature. Therefore, from now on, we consider only measurements with the signal beam stopped.

The histogrammatic plot[8] of pump second harmonic + LO is depicted in figure 5.11. Starting from the low frequencies, a principle of bimodal distribution is distinguishable (see the 392 THz histogram). Then, at 394 THz, an abrupt enlargement of the distribution occurs. The region of 394-398 THz exhibits the most clear double peaked feature. For higher frequencies the distribution width reduces and finally, over 404 THz, assumes a standard gaussian profile.

If we compare this behavior with the spectra of the two pulses (figure 5.10), we see that the rise of the bimodal distribution occurs in correspondence of the overlap between the LO and the pump second harmonic spectral content. This evidence supports the hypothesis that bimodal distribution is related to the interaction between LO and pump second harmonic. The asymmetry of the enlargement is linked to the overlap shape: LO and pump second harmonic have different gaussian profiles (due to their different time durations) and therefore their superposition is asymmetric.

[8]The histogrammatic plot is obtained with the same phase and pump delay of the vacuum state trace.

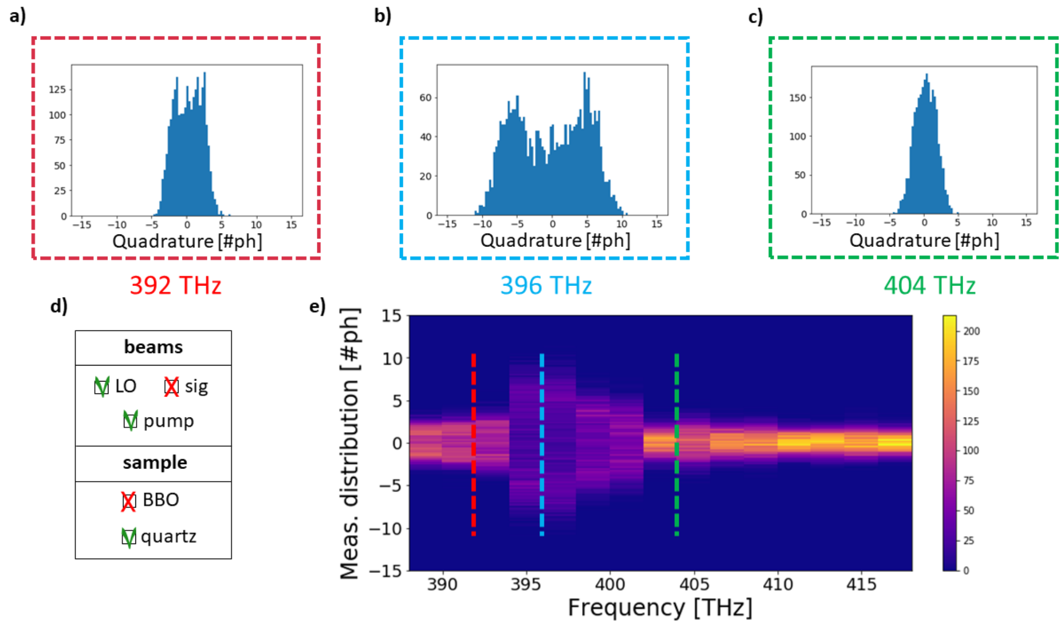

Figure 5.11: distribution of the pump second harmonic heterodyne trace (d-e). Already at low frequencies the bimodal distribution can be observed (a). Suddenly, there is an abrupt enlargement of the distribution in correspondence of the overlap between the LO and pump second harmonic spectral content. In this region, we appreciate the bimodal distribution at its best (b). Finally, for higher frequencies, the width of the distribution diminishes and approaches the standard gaussian profile (c).

Pump SH + LO using a BBO crystal

We now change sample and study the pump second harmonic heterodyne trace produced with a BBO crystal. Since the second harmonic generation process is far more efficient in this sample, we use the arrays detection system. The advantage of using photodiodes arrays consists in having 256 channels to sample different pulse frequencies at the same time. Therefore, compared to the data acquired with the differential detector (where we can acquire just one frequency at a time), the histogrammatic plot will have many more frequency steps.

Figure 5.12 depicts the histogrammatic plot of the acquired heterodyne trace. We definitely retrieve the rise of the bimodal distribution observed in the previous paragraph (figure 5.11). Also in this case, an enlargement of the distribution occurs in correspondence of the overlap between the pump second harmonic and LO spectral content (figure 5.2). Thanks to the arrays photodiodes, we better appreciate the asymmetry of the enlargement. We underline that the overlap region for $\alpha-$quartz and BBO samples are slightly different. This is because the wavelength of the two pulses were tuned on different values for the two experiments (compare figure 5.2 to figure 5.10).

In conclusion, the bimodal distribution arises in the correspondence of the spectral overlap between the LO and the pump second harmonic pulses. This happens if we generate the pump second harmonic with both the $\alpha-$quartz and the BBO crystal. For frequencies out of the range of the spectral overlap, we retrieve a gaussian shaped distribution. Therefore, the bimodal distribution must be linked to the recombination of LO and pump SH that occurs in order to perform heterodyne detection.

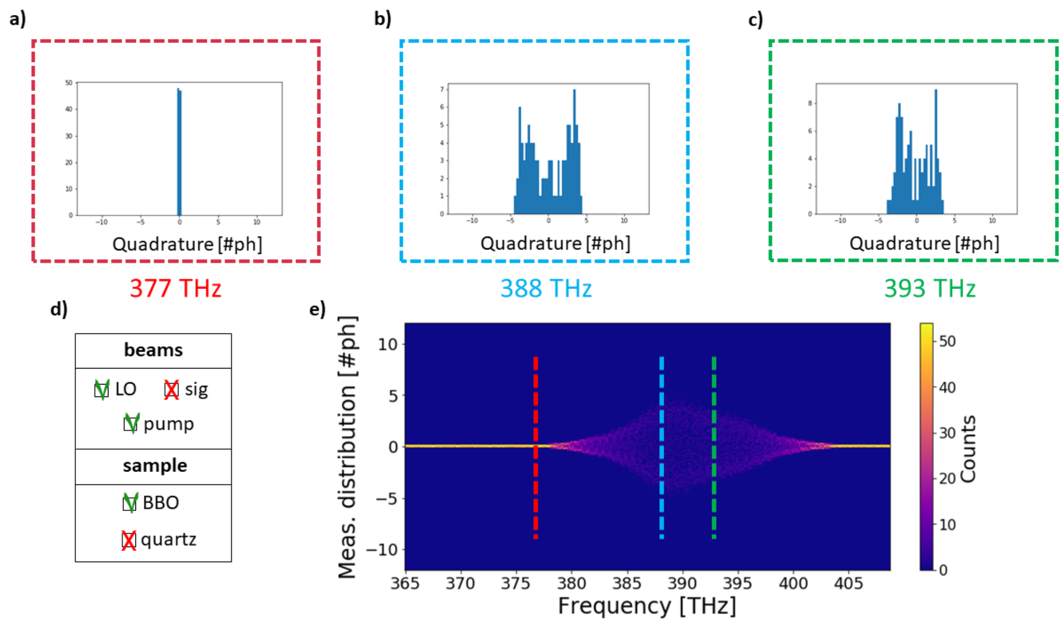

Figure 5.12: distribution of the pump second harmonic (produced with a BBO crystal) heterodyne trace (d-e). Data were acquired with photodiodes arrays. We retrieve the double peaks presence in correspondence of the distribution enlargement. As in figure 5.11, the rise of the the enlargement occurs on the overlap between the LO and the pump second harmonic spectral content (b-c).

5.3.3 Distribution vs pump delay

In order to characterize the bimodal distribution of the pump second harmonic heterodyne measurement, we perform a time-resolved study. In particular, we're interested in varying the pump delay and studying the distribution behavior. We perform this experiment on both the $\alpha-$quartz and the BBO crystals, acquiring the data respectively with the differential detector and the photodiodes arrays. Since we're not interested in the signal contribution, we consider only the pump SH + LO system.

Starting from the $\alpha-$quartz sample, we study its histogrammatic plot for an arbitrary phase (since there is no phase dependence) and a fixed frequency. We choose the frequency corresponding to the maximal splitting, that for the $\alpha-$quartz sample corresponds to 396 *THz* (figure 5.11). The result is plotted in figure 5.13a.

We retrieve the presence of the bimodal distribution for the whole 2.5 *ps* interval of values scanned. The splitting of the two peaks is maximum in coincidence with the temporal overlap of the two pulses and then slowly decreases in both positive and negative times directions. We recall that the original temporal duration of the pump and the signal/LO pulses is rescpetively 100 and 50 *fs*. Therefore, we wouldn't expect a persistence of the bimodal distribution for these long times. Anyway, pump and LO time duration can be different from their starting values. In particular, the pump second harmonic could be not compressed. According to this consideration, the persistence of the bimodal distribution for long times would be explained by a long time duration of the pump second harmonic. However, we would expect this type of time broadening to be not on a picoseconds time scales.

Alternatively, we have to consider the LO temporal length. We recall that, since we're using the differential detector, the LO is shaped in order to select a specific frequency. For the Heisenberg uncertainty principle $\Delta\nu\Delta t \geq 1$ and so a shortening of the spectral band reflects into a broadening of the pulse time duration. Considering a time duration of 3 *ps*, this would correspond to a pulse with a spectral bandwidth of 0.33 *THz*. This is in line with the spectral width of the LO shaped pulse (figure 2.11a).

We now analyze data acquired with photodiodes arrays using the BBO sample. We recall that, with this acquisition system, we perform the frequency resolved measurement without shaping the LO spectral content. Therefore, time duration of the LO pulse before the detector is expected to be consistent with the nominal value of 50 *fs*.

The measurement distribution is depicted in figure 5.13b. The plot is obtained fixing an arbitrary phase and choosing the frequency of maximal splitting, that for the BBO experiment is 402 *THz*[9]. Also in this case, we retrieve the bimodal distribution with a maximal splitting in coincidence with the temporal overlap of the two pulses. Moreover, the splitting persists at positive and negative times on a picosecond time scale.

We recall that, when we use the photodiodes arrays acquisition system, each pixel of the two detectors measures a small region of the pulse spectrum. Since the Heisenberg relation $\Delta\nu\Delta t \geq 1$ has a general validity, measuring a small spectral region determines in the detector a time elongation of the measured pulse. Therefore, the persistence of the bimodal distribution on picosecond time scales is determined by the actual shaping we perform frequency resolving the measurement on the detector. We underline that arrays frequency resolution ($\Delta\omega \sim 0.2$) is comparable with a picosecond time scale.

In conclusion, a comparison between the $\alpha-$quartz and the BBO data shows that in both cases there is a double peak feature that lasts more than 2 *ps*. We attribute this behavior to a time broadening of the pulses due to the Heisenberg uncertainty principle. In particular, for the $\alpha-$quartz data (figure 5.13a) we link the bimodal time duration to the shaping we perform on the LO, while in the BBO case (figure 5.13b) to the time broadening of the final pulses that occurs inside the detector.

[9] We remark that the different value of maximal splitting is determined by the different tuning of the two pulses performed in the two experiments.

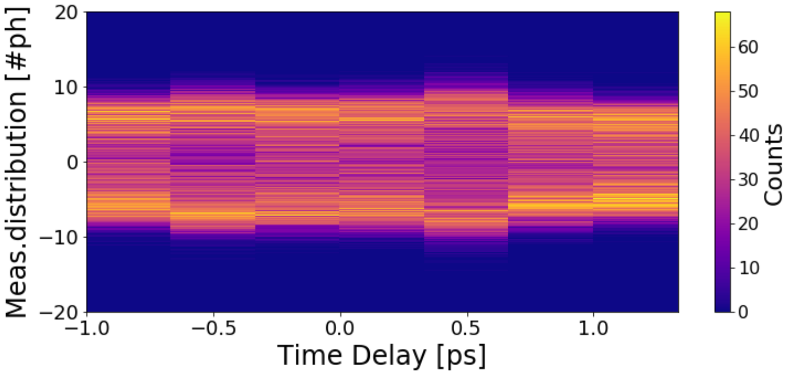

(a) $\alpha-$quartz sample

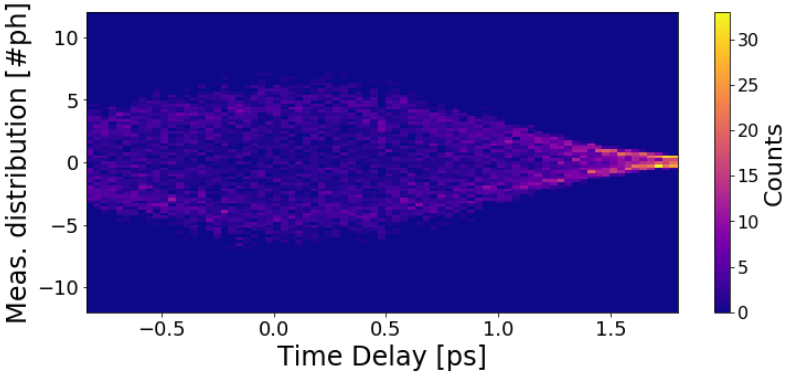

(b) BBO sample

Figure 5.13: histogrammatic plots of the pump second harmonic heterodyne trace for different samples. We build these plots fixing an arbitrary phase (since there is no phase dependence) and choosing the frequency of maximal splitting. Both for the $\alpha-$quartz (a) and BBO data (b) we retrieve a bimodal distribution that persists for picoseconds time scales. We attribute this behavior to the temporal broadening of the pump second harmonic that could occur in the SHG process.

5.3.4 Pump power test

In the previous sections we characterized the bimodal distribution retrieved in the pump second harmonic heterodyne trace. Briefly summarizing, we saw that a pair of symmetrical peaks arises when both the pump second harmonic and the local oscillator are present. Moreover, just the frequencies laying in the overlap region of the two pulses spectra exhibit the bimodal distribution. Checking different pump delays unveiled that the double peak feature persists for times longer then 2.5 ps. We attribute this behavior to a long time duration of the pump second harmonic pulse. Now that we have checked all these parameters, we can move to other characterizations. In particular, we want to see how the bimodal distribution is affected by a change in the pump photon number.

To build histogrammatic plots of the measurements, we fix a pump delay in proximity of the temporal overlap (we saw that bimodal distribution survives for long time delays, so it suffices to be close to the center) and a frequency in correspondence of the maximal splitting. For this power study[10], we use the $\alpha-$quartz crystal to generate pump second harmonic and therefore we acquire data with the differential detector as a function of the phase. In order to obtain different pump powers, we use a graduated filter.

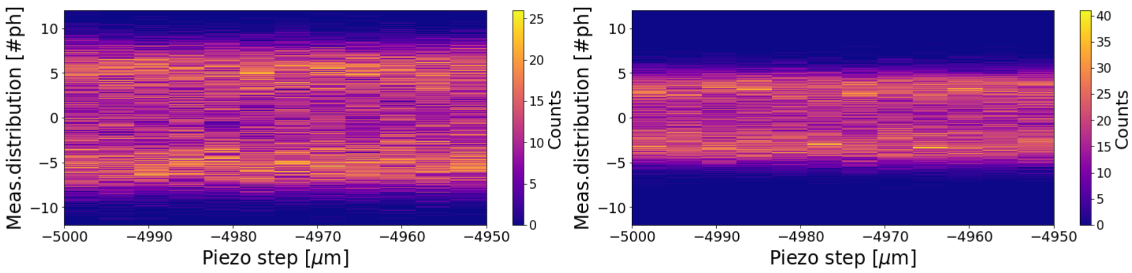

(a) Pump power = 1.1 mW

(b) Pump power = 0.7 mW

Figure 5.14: histogrammatic plots of the pump second harmonic heterodyne trace for two different pump powers. We see that diminishing the number of photons in the pump pulse determines a reduction in the two peaks distance.

Figure 5.14 shows two histogrammatic plots acquired with different pump powers. We see that reducing the photon number in the pump pulse determines a shortening of the two peaks distance. This behavior is confirmed also considering a wider range of pump photon numbers.

Figure 5.15 plots on the same graph the different distribution profiles obtained with various pump powers. Very low photon numbers determine a single peaked gaussian profile. Then, if we gradually enhance the pump photon number, a splitting of the central peak arises. Moreover, the two symmetrical peaks become more and more distant as we continue increasing the pump power.

Under the light of these results, in the next section we're going to present a model to describe the system we're looking at.

[10]We recall that power beam is directly related to the pulse photon number (equation 3.16)

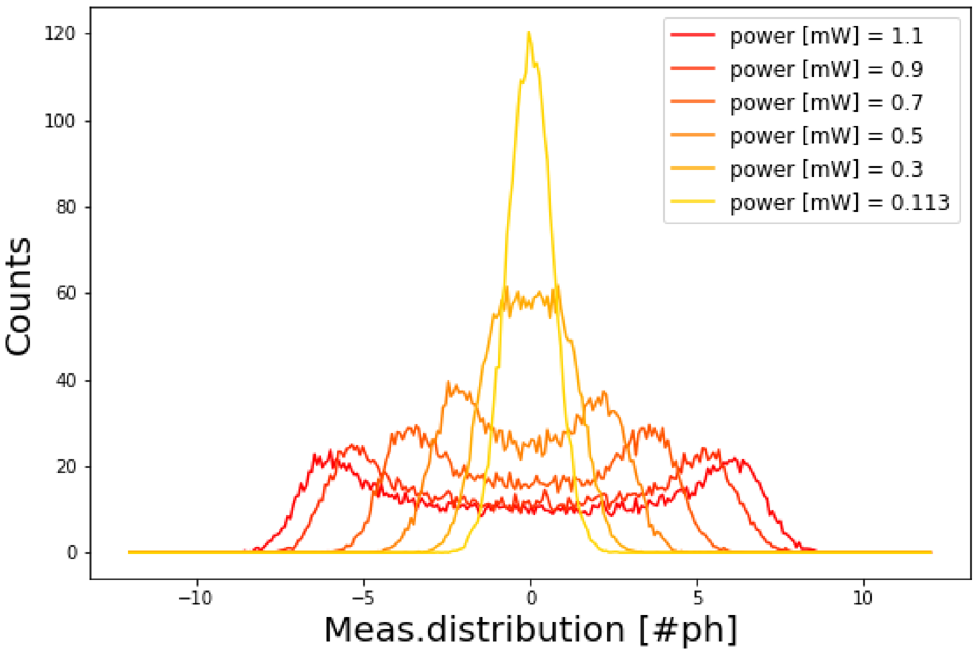

Figure 5.15: multiple distribution profiles obtained for different pump powers. Starting from low photon numbers, the distribution is a gaussian with a central peak. A gradual increasement of the pump power gives rise to a splitting of the main peak into a pair of symmetrical ones. Moreover, the higher is the pump photon number, the wider is the splitting of the distribution.

5.4 The origin of bimodal distribution: phase uncertainty

Until now, we have performed many characterizations of the bimodal distribution arising in pump second harmonic heterodyne trace. In particular the last one, where we investigated the change in the distribution shape related to the pump number of photons, unveiled two important features:

- the distribution, for low photon numbers, is a gaussian peaked on the zero value.
- increasing the number of photons of the pump (and hence of the pump second harmonic) changes the shape of the distribution. Thus, the central peak splits in a pair of symmetrical peaks. Moreover, the bigger is the number of photons, the wider is the separation between the two peaks.

If we think of the coherent state state representation in the phase space, we can figure out some important correspondences with our system.

Vacuum state

First of all, we consider a vacuum state $|0\rangle$, i.e. a state with zero photons. In chapter 3 we proved that the vacuum state of the quadrature field has a zero mean value (equation 3.6) and a constant variance value of 1/2 (equation 3.7). This is represented in the phase space by a spot with a size determined by the Heisenberg uncertainty principle $\sigma_X^2 \sigma_P^2 = 1/4$ (figure 5.16). Moreover, if we measure the vacuum state quadrature, we retrieve a gaussian distribution peaked on the zero value [4]. We underline that we retrieved this behavior in our measurement distribution studies (figure 5.4).

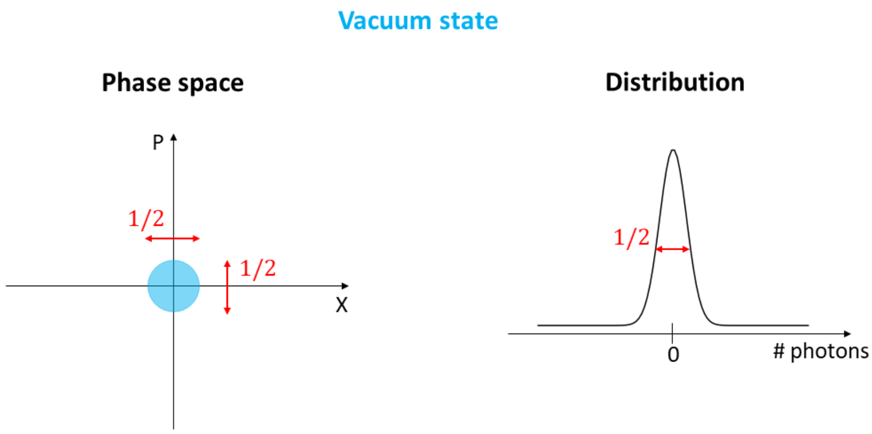

Figure 5.16: vacuum state is represented in the phase space by a spot of fixed size centered on the axis origin. Vacuum state distribution is a gaussian peaked on the zero value.

Coherent state

The coherent state is a rigid shift of the vacuum state in the phase space. This is formally described [4] by the action of the displacement operator $\hat{D}(\alpha) = exp(\alpha\hat{a}^\dagger - \alpha^*\hat{a})$:

$$\hat{D}(\alpha)|0\rangle = |\alpha\rangle \tag{5.1}$$

Since α is in general a complex quantity, we can express it in polar coordinates $\alpha = |\alpha|e^{i\theta}$. Though, the position of the coherent state in the phase space is characterized by a radius $|\alpha|$ and a phase θ.

As we've seen, the radius of the displacement $|\alpha|$ is equal to the square root of the state photon number (equation 3.9). Therefore, the higher is the displacement, the higher is the photon number

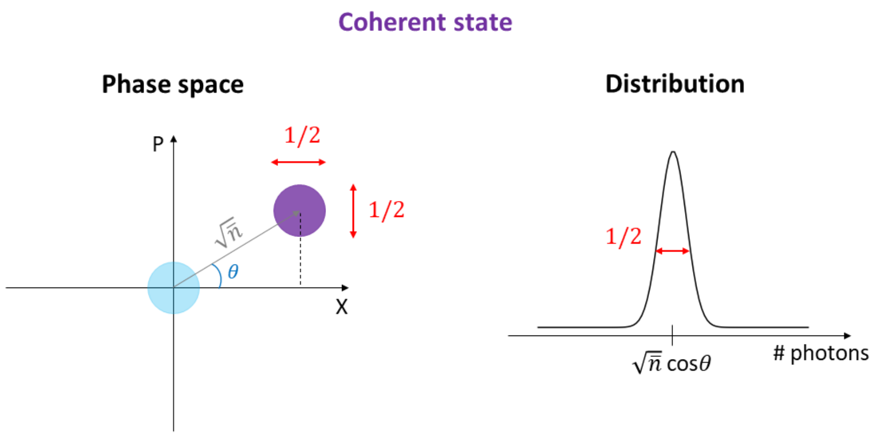

Figure 5.17: the phase space representation of a coherent state is obtained by applying a rigid shift to the vacuum state. Therefore, the coherent state distribution still has a gaussian profile. We underline that, for a given photon number (that is proportional to the radius of the displacement), a multitude of coherent states characterized by different phases θ exists.)

associated to the state (figure 5.17). As for the vacuum state, also the coherent state exhibits a gaussian distribution where the central peak depends on the number of photons.

We underline that photon number doesn't determine uniquely a coherent state. Indeed, every coherent state is characterized not just by the radius of the displacement $|\alpha|$ but also by the phase θ. So, for a fixed photon number, a multitude of coherent states with different phases exists.

Phase-averaged coherent state (PHAV)

Starting from this evidence, more complex states can be built. In particular we're interested in the so called *phase-averaged* or *phase-randomized coherent state* (PHAV). This state consists in a superposition of coherent states with random phases [20]. We're interested in this kind of states because the representation of a PHAV in the phase space is a ring whose radius is proportional to the mean photon number. Moreover, the probability function that describes a PHAV is a bimodal distribution characterized by a pair of symmetrical peaks (figure 5.18).

This matches the distribution observed in our pump second harmonic heterodyne experiment (figure 5.15). Indeed, the ring radius, and hence the peaks distance, is related to the state photon number. So, for the PHAV as for our experimental data, an increment in the photon number causes a widening of the two peaks distance (figure 5.19). Moreover, if we reduce drastically the number of photons approaching the zero value, the two peaks collapse into a single gaussian peak, that corresponds to the vacuum state[11].

Origin of the phase uncertainty in pump second harmonic heterodyne detection

Until now, we have just explained the analogies between a PHAV and the state that we create in our pump second harmonic heterodyne experiment. However, if we're really dealing with a phase-randomized state, we have to understand where the phase uncertainty origins.

We use as a reference PHAV generation process the method proposed in [20]. Briefely summarizing, Allevi et al. split an initial beam in two parts and then insert a delay line along one of the two optical paths. Introducing random delays for every pulse and then recombining the two initial beams enables Allevi et al. to obtain a superposition of phase randomized states.

We can retrieve a similarity between their PHAV generation process and our pump second harmonic heterodyne measurement, that is the final recombination of the beams. The difference

[11] We underline that vacuum state has no phase, since it is centered on the origin of the phase space axes.

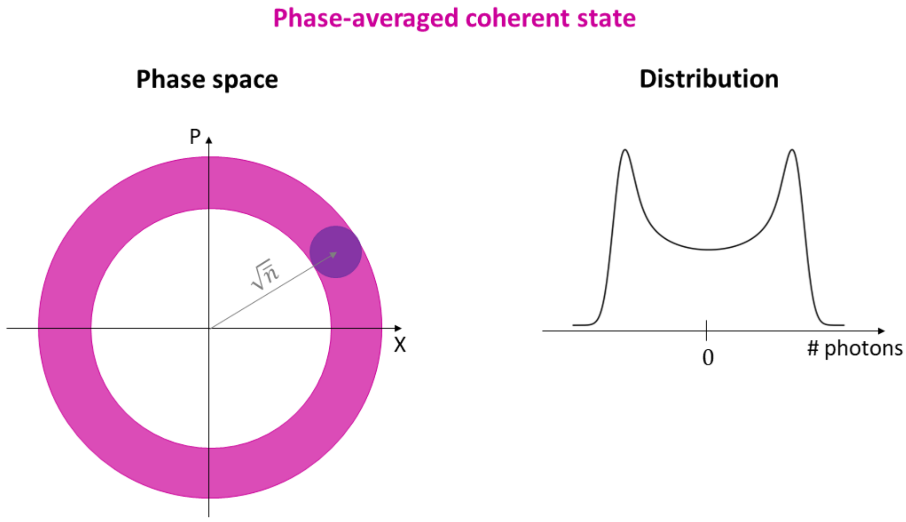

Figure 5.18: a phase-randomized or phase-averaged coherent state is a superposition of coherent states with random phases. This state is represented by a ring in the phase space and has a double peaked symmetrical distribution.

resides in the fact that we're not using an initial beam split in two parts[12]. On the contrary, we combine two different beams, one generated from the signal (local oscillator) and one from the idler (pump second harmonic.) of the laser + OPA system.

In order to understand the origin of the phase uncertainty, we recall a peculiar feature of the laser pulses generation process. As we mentioned in section 2.5, each laser pulse consists in a comb of frequencies equally spaced. Therefore, laser modes can be written as $f_n = f_0 + nf_r$, where f_0 is the frequency offset of the spectrum and f_r is the laser repetition rate.

However, every laser pulse exhibits a random absolute phase (see section 2.5) and this, in the frequency domain, reflects into a random value of the offset f_0 for every pulse. This effect occurs just for the laser + OPA signal (i.e. the local oscillator), since the idler (i.e. the pump) experiences a self stabilization process [21].

We write the two pulses frequency combs as:

$$\begin{aligned} f_{LO} &= f_0 + n_1 f_r \\ f_{pump} &= f_0' + n_2 f_r \end{aligned}$$

where f_0' represents a fixed frequency offset. Moreover, the pump second harmonic will exhibit a spectrum:

$$f_{pump\ SH} = 2f_0' + 2n_2 f_r$$

It is crucial to notice that LO and pump second harmonic do not have the same frequency offset. Indeed, local oscillator has a starting frequency f_0 while the pump second harmonic has a fixed offset $2f_0'$. Therefore, because of the random nature of f_0, we expect the recombination of the two beams to occur with a random phase relation. In conclusion, we address the phase uncertainty of our state to the random absolute phase of the signal (i.e. the local oscillator) produced by the laser + OPA system.

We can test our model looking at the measurement distribution when the phase stabilization system (section 2.5) is switched on .

[12] We recall that this would be the case if the signal was opened. However, we proved that the presence of the signal beam doesn't affect the nature of the bimodal distribution (figure 5.6).

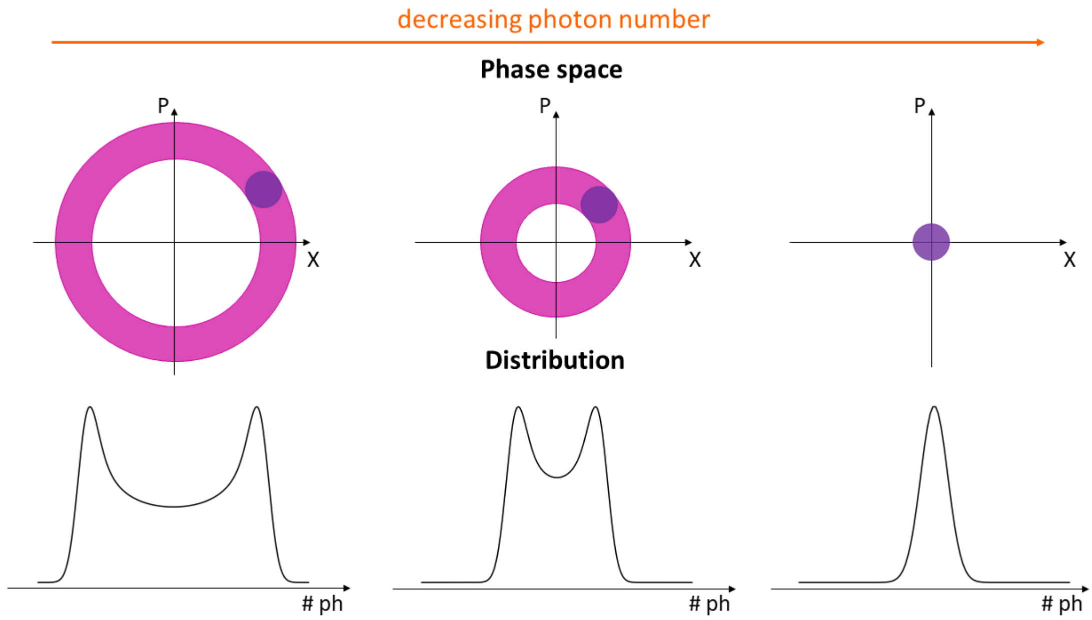

Figure 5.19: representation of the phase-averaged coherent state behavior as the photon number is changed. Reducing the photon number of the state diminishes the radius of the ring in the phase space and hence the distance of the two peaks in the distribution. For very low photon numbers we retrieve a single peaked distribution that matches the vacuum state one. We underline that this behavior is the same that we retrieved varying the power of the pump (figure 5.15).

5.4.1 CEP test

In the previous paragraph we proposed a model that explains the bimodal distribution retrieved in the pump second harmonic heterodyne measurements. In particular, we think that we're measuring a superposition of phase randomized states, where the phase uncertainty is determined by the random absolute phase of each laser pulse.

Since we have a system to stabilize the laser pulses absolute phase (CEP)[13], we can test this theory switching on the stabilization system and looking at the obtained measurement distributions.

The histogrammatic plots are obtained fixing the frequency of maximal splitting and a pump delay in proximity of the temporal overlap. To produce the pump second harmonic we use the $\alpha-$quartz crystal and therefore we acquire the data with the differential detector.

Figures 5.20 (a)-(b) show a comparison of the pump second harmonic heterodyne trace with and without the employment of the phase stabilization system. Figures 5.20 (c)-(d) reports the vacuum state traces with and without CEP in order to prove that the system is working well and isn't affecting the standard gaussian distribution.

We clearly see that the double peak feature disappears when the phase stabilization system is working. Moreover, the distribution becomes a gaussian with a single central peak. We can even appreciate the quadrature oscillation. However, we retrieve an instability of the central peak position for different phases. This happens because the CEP system fixes properly consecutive pulses but lacks in long range stability. Since we acquire thousands of pulses for every piezo step, we attribute the small shifts of the distribution to this intrinsic defect of the stabilization system.

Figures 5.21 (a)-(b) present pump second harmonic traces in presence of the signal. Signal + LO are reported in figures 5.21 (c)-(d) to prove that CEP is correctly working. Also in this case, when the pulses absolute phase is stabilized, the bimodal distribution disappears. Moreover, in the pump SH + signal data, we can retrieve quadrature oscillations. Small shifts of the distribution are due to the long range instability of the stabilization system.

In conclusion, we proved that both in the presence and in the absence of the signal, bimodal distribution is cancelled when the phase stabilization system is switched on. Moreover, the distribution assumes a gaussian profile and unveils quadrature oscillations previously hidden. These results support heavily the hypothesis that pump second harmonic combined with local oscillator gives rise to a superposition of phase randomized states, where the phase uncertainty is determined by the local oscillator random frequency offset [21].

[13]see section 2.5.

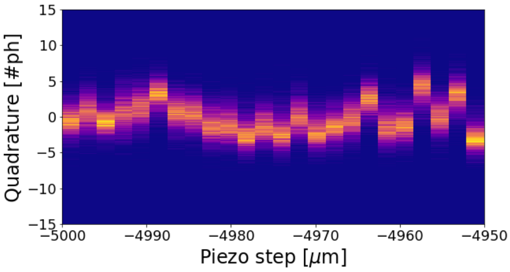

(a) CEP + pump

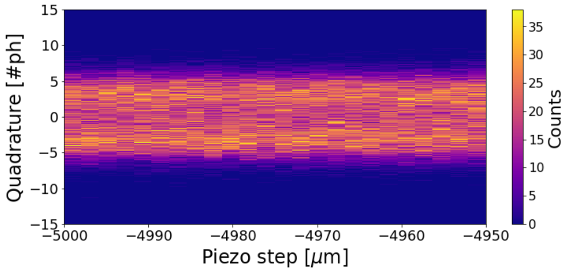

(b) no CEP + pump

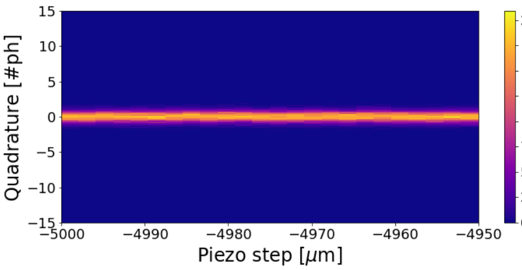

(c) CEP + no pump

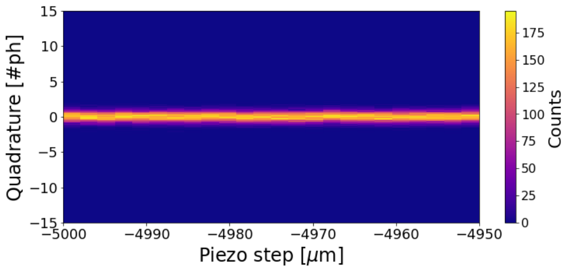

(d) no CEP + no pump

Figure 5.20: in this panel we present histogrammatic plots obtained when signal beam is stopped. In particular, figures (a)-(b) present the pump second harmonic heterodyne trace distribution when the stabilization system is respectively switched on/off. Figures (c)-(d) present the same plots when also the pump beam is blocked (therefore what we see is the vacuum state distribution). Looking at the pump second harmonic heterodyne trace (figures (a)-(b)), we notice that stabilizing pulses phase transforms the bimodal distribution in a gaussian centrally peaked. We can even retrieve a quadrature oscillation. On the contrary, figures (c)-(d) show that CEP isn't affecting the vacuum state distribution.

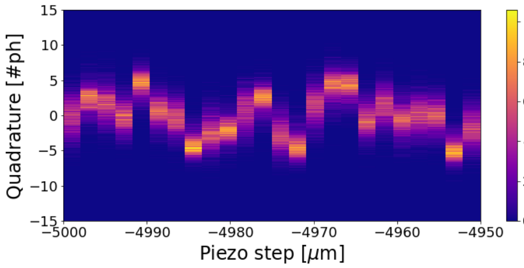

(a) CEP + pump

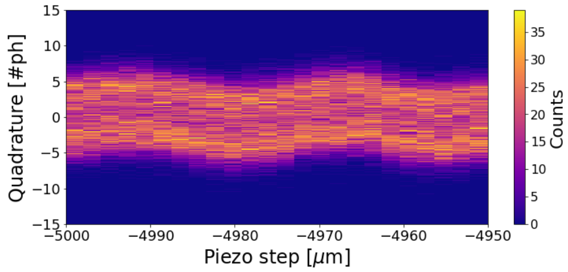

(b) no CEP + pump

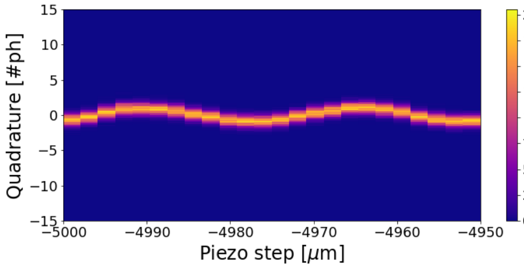

(c) CEP + no pump

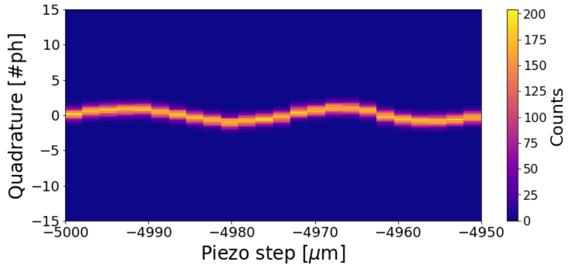

(d) no CEP + no pump

Figure 5.21: in this panel we present histogrammatic plots obtained with the signal beam opened. Figures (a)-(b) present signal + pump second harmonic heterodyne trace when the stabilization system is switched on/off. In figures (c)-(d) pump beam is blocked, thus we see the signal + LO distribution. Also in this case, bimodal distribution is cancelled when the stabilization system is working. When the pump is blocked((c)-(d)), CEP doesn't alter the measurement distribution.

5.5 Quantitative estimations by means of Pattern Function Tomography

In previous section we qualitatively proved that the state measured in the pump second harmonic heterodyne experiment is a superposition of phase randomized states. However, we lack an estimation of important quantities like mean photon number, $\sigma^2_{\hat{n}}$, etc. We're interested in retrieving these information to understand if the superposition is composed by coherent states or by something else.

For this purpose, we use quantum tomography, and in particular *Pattern Function Tomography*. In the following, we present the theoretical principles of this analysis technique and then we discuss the results obtained for our experimental data.

5.5.1 Pattern Function Quantum Tomography

The aim of Pattern Fucntion Quantum Tomography is estimating, for an arbitrary quantum system, the mean value $\langle \hat{O} \rangle$ of a system operator $\hat{O}$ using only the results of the measurements on a set of observables $\{\hat{Q}_\lambda, \lambda \in \Lambda\}$ called *quorum* [22]. This is achieved using the *estimator* $R[\hat{O}](q;\lambda)$, also called *pattern function*, which is a function of the eigenvalues q of the quorum operators. Pattern Function Quantum Tomography processes the data acquired by means of the estimator and returns and estimation of the observable mean value. In particular, by integrating the estimator with the probability $p(q,\lambda)$ of having outcome q when measuring $\hat{Q}_\lambda$, the mean value of $\hat{O}$ is obtained as follows:

$$\langle \hat{O} \rangle = \int_\Lambda d\lambda \int dq_\lambda \; p(q,\lambda) R[\hat{O}](q;\lambda) \tag{5.2}$$

where the first integral is performed on the values of λ that denote all quorum observables, and the second on the eigenvalues of the quorum observable q_λ determined by the λ variable of the outer integral.

In the case of heterodyne data samples, the quorum of observables is composed by the quadrature operators: $\{x_\phi, \phi \in [0, 2\pi]\}$. According to [23], equation 5.2 becomes:

$$\langle \hat{O} \rangle = \int_0^{2\pi} \frac{d\phi}{\pi} \int_{\mathbb{R}} dx \; p(x,\phi) R[\hat{O}](x;\phi) \tag{5.3}$$

Moreover, for a discrete value of quorum observables and data acquired, both integrals appearing in equation 5.3 can be replaced [22] by an infinite sum:

$$\langle \hat{O} \rangle = \lim_{M \to \infty} \frac{1}{M} \sum_{k=1}^{M} R[\hat{O}](x_k;\phi_k) \tag{5.4}$$

Since in a heterodyne measurement we obtain a finite number of experimental data pairs:

$$\{(x_1;\phi_1), (x_2;\phi_2), ..., (x_k;\phi_k), ..., (x_M;\phi_M)\}$$

we approximate the infinite sum of equation 5.4 with:

$$S_M = \frac{1}{M} \sum_{k=1}^{M} R[\hat{O}](x_k;\phi_k) \tag{5.5}$$

The error we commit assuming $\langle \hat{O} \rangle = S_M$ is given by the Central Limit Theorem:

$$\epsilon_M = \sqrt{\frac{\sum_{k=1}^{M} \left(R[\hat{O}](x_k;\phi_k) - S_M \right)^2}{M(M-1)}} \tag{5.6}$$

Therefore, the finite sum converges to the mean value of the operator with a statistical error that decreases as $1/\sqrt{M}$.

Calculation of the pattern functions

Now that we have explained the working principles of pattern tomography, we need to find an expression of the estimator $R[\hat{O}]$ for the operators we want to estimate. In the case of optical systems, one can reduce the estimation of the expectation value of any operator to the estimation of normally ordered products of creation and annihilation operators $(\hat{a}^\dagger)^n \hat{a}^m$ [23]. Therefore, we can estimate any operator[14] with the formula that Richter et al. retrieved in [24]:

$$R[(\hat{a}^\dagger)^n \hat{a}^m](x;\phi) = \frac{e^{i(m-n)\phi} H_{m+n}(x)}{\sqrt{2^{m+n}\binom{n+m}{m}}} \tag{5.7}$$

where $H_n(x)$ are Hermite polynomials.

If we consider also the quantum efficiency η contribution to the measurement, equation 5.7 becomes:

$$R_\eta[(\hat{a}^\dagger)^n \hat{a}^m](x;\phi) = \frac{e^{i(m-n)\phi} H_{m+n}(\sqrt{\eta}x)}{\sqrt{(2\eta)^{m+n}\binom{n+m}{m}}} \tag{5.8}$$

In table 5.1 we report the estimators $R_\eta[\hat{O}](x,\phi)$ of some useful operators calculated with equation 5.8.

$\hat{O}$	$R_\eta[\hat{O}](x,\phi)$
$\hat{a}$	$\sqrt{2}e^{i\phi}x$
$\hat{a}^2$	$e^{2i\phi}\left(2x^2 - \frac{1}{\eta}\right)$
$\hat{x}_\theta$	$2xcos(\phi-\theta)$
$\hat{x}_\theta^2$	$\frac{1}{2}\left\{1 + \left(2x^2 - \frac{1}{\eta}\right)[4cos^2(\phi-\theta) - 1]\right\}$
$\hat{a}^\dagger\hat{a}$	$x^2 - \frac{1}{2\eta}$
$(\hat{a}^\dagger\hat{a})^2$	$\frac{2}{3}x^4 - x^2\left(\frac{2-\eta}{\eta}\right) + \frac{1-\eta}{2\eta^2}$

Table 5.1: we report the estimators of some useful operators.

Now that we have presented the working principle of Pattern Function Tomography, we apply it to our pump second harmonic experimental data.

[14] Since we're interested in optical systems.

5.5.2 Quadrature expectation values

In the following we use pattern function quantum tomography techniques to study pump second harmonic heterodyne data and estimate mean photon number, quadrature values, etc.

Pump SH + LO

We start our analysis from the quadratures expectation values. According to table 5.1, we can estimate the quadrature mean value $\langle \hat{x}_\theta \rangle$ and its related variance $\sigma^2_{\hat{x}_\theta} = \langle \hat{x}^2_\theta \rangle - \langle \hat{x}_\theta \rangle^2$. The results obtained for the pump second harmonic heterodyne trace in the absence of signal are depicted in figure 5.22.

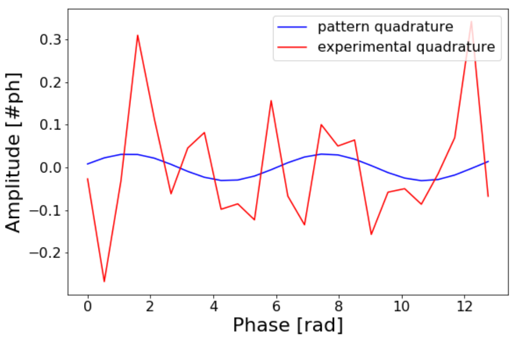

(a) quadrature

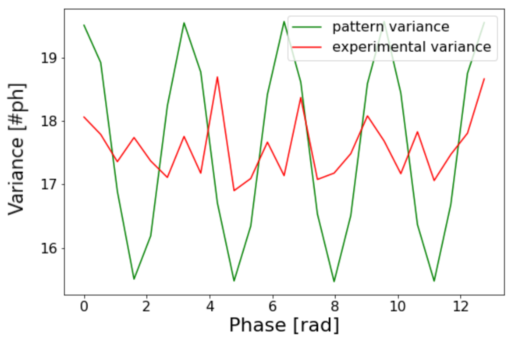

(b) variance

Figure 5.22: comparison between pump second harmonic heterodyne data and Pattern Function Tomography estimations. Measurements were performed with the signal beam blocked. In (a) quadratures obtained with averaged experimental data (red) and tomography estimation (blue) are plotted. Both functions present small oscillations around the zero value. However, the regular oscillation of the pattern function data isn't present in the experimental ones. Figure (b) presents the same comparison for the estimated variances (in red the experimental one, in green the variance estimated with pattern function). Both variances oscillate around values larger then the coherent state reference one (0.5). This is in line with the characteristic enlargement of the bimodal distribution. We attribute the different amplitude oscillations to an overestimation of the pattern function variance due to the phase uncertainty of the quadrature.

In figure 5.22a, a comparison between the quadrature averaged over experimental data (red) and the one estimated with Pattern Function Tomography (blue) is presented. Both lines have small amplitude oscillations around zero. However, quadrature values estimated with Pattern Function Tomography exhibits a regular oscillation that isn't encountered in experimental data.

Moreover, figure 5.22b plots both the pattern function estimated variance (green) and the experimental one (red). We notice that both functions assume values larger then 0.5, that is the vacuum state/coherent state variance. This is explained by the enlargement of the measurement distribution that occurs with the rising of the double peak feature (figure 5.11). Anyway, the Pattern Function Tomography estimated variance exhibits an amplitude oscillation almost twice the experimental data one. We explain this behavior with the phase uncertainty determined by interferometer instability (figure 3.5). In particular, Pattern Function Tomography does not take into account a phase uncertainty in the experimental data and therefore all the noise enters in the amplitude. The result is an enhancement of the oscillation amplitude.

Pump SH + LO + signal

Figure 5.23 presents a comparison of the experimental and pattern function estimations of quadrature values with the opened signal. In figure 5.23a we retrieve a good agreement between the averaged experimental data and the pattern function estimated values. Both exhibit a regular quadrature oscillation, as expected in the presence of signal. On the contrary, the variance comparison (figure 5.23b) shows an overestimation in the oscillation amplitude by Pattern Function

Tomography. Once again, we attribute the mismatch to the phase noise determined by the interferometer instability.

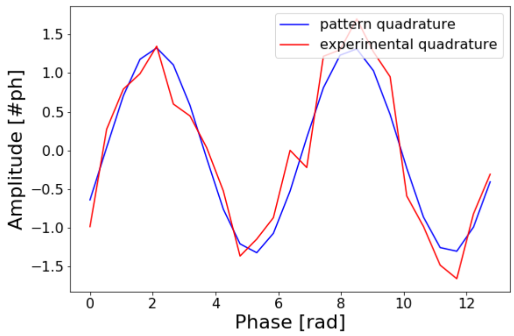

(a) quadrature

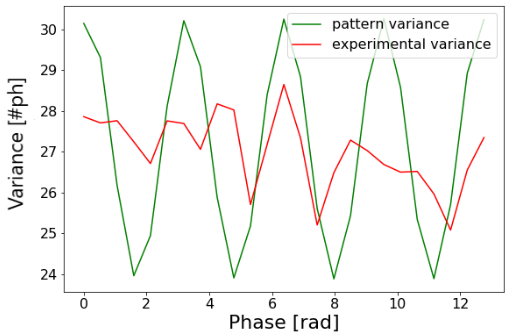

(b) variance

Figure 5.23: comparison between experimental data and values obtained with Pattern Function Tomography with the signal beam opened. In figure (a) we see a good agreement between the averaged experimental data (red line) and the pattern function estimated ones (blue). On the contrary, the variance comparison in (b) shows that pattern function overestimates the experimental data variance. Also in this case, we attribute the estimation error to the phase uncertainty determined by the interferometer instability.

In conclusion, we exploited Pattern Function Tomography to estimate quadrature values and the related variances. We found a good agreement with experimental data for quadrature mean values $\langle x_\phi \rangle$, but not for the estimated variances $\sigma^2_{x_\phi}$ both in the presence/absence of signal. In particular, pattern function variance presented an overestimated oscillation amplitude. We explained this behavior with the lack of phase uncertainty in pattern function formalism. Since the phase has no error, all the noise enters in the amplitude, determining an enhancement of the oscillation.

5.5.3 Photon number estimation

Pattern Function Tomography allows as not only to check some results directly observable in the experimental data (like in the previous paragraphs), but to retrieve hidden information. That is the case for mean photon number $\langle \hat{n} \rangle$ and related variance $\sigma^2_{\hat{n}}$ estimation.

We underline that, since there is no phase dependence in the expression of the number operator estimators (table 5.1), we do not have to deal with interferometer instabilities and hence we don't expect a variance overestimation.

Photon number vs frequency

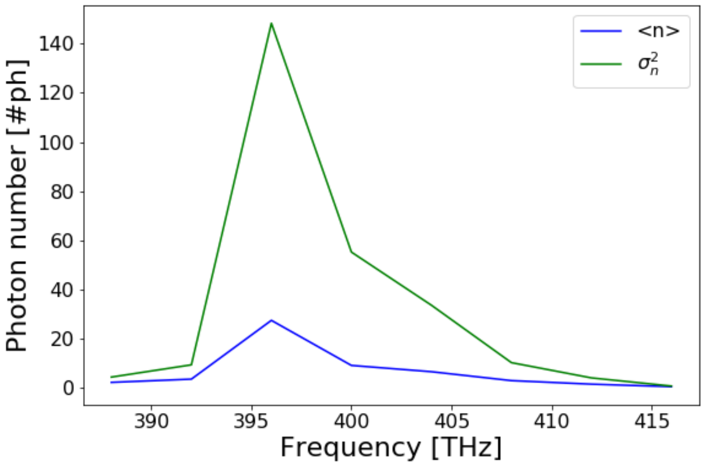

Figure 5.24: estimations performed on the pump second harmonic heterodyne data. Photon number mean value (blue) and variance (green) of the pump are plotted as a function of the pulse frequencies. We see that both photon number and variance exhibit a maximum at 396 *THz*. This behavior matches with the distribution enlargement retrieved in correspondence of the pulses overlap (figure 5.11). In addition, estimated variance results always bigger than mean photon number. This evidence suggests that observed phase randomized states have a distribution larger than the coherent state one.

Figure 5.24 shows the estimated photon number with the related variance for the pump second harmonic[15] heterodyne trace. We first see that both the photon number and the variance present a maximum at 396 *THz*. This evidence matches with the distribution enlargement observed in correspondence of the pulses overlap (figure 5.11).

Moreover, we notice that variance is larger than the related mean values. Recalling that for a coherent state holds $\langle \hat{n} \rangle = \sigma^2_{\hat{n}} = |\alpha|^2$, phase randomized states we measure are most likely not a superposition of coherent states (see Appendix C).

Photon number vs pump power

To proceed in quantitative estimations , we apply Pattern Function Tomography on pump second harmonic heterodyne data acquired as a function of the power pump (figure 5.15).

Figure 5.25 shows the photon number mean value and variance behavior as a function of the power of the pump. Estimated mean values (blue line) have a growth almost linear, whereas variance grows much faster. However, what we're really interested in is the behavior of the variance as a function of the photon number. Therefore, we take the estimated values of figure 5.25 and we build a variance vs mean value graph. The result is depicted in figure 5.26.

Figure 5.26 definitely proves that the relation between variance and photon number is not linear. Moreover, a quadratic curve (blue line) fits estimated values with a very good agreement.

[15]Produced with the $\alpha-$quartz sample

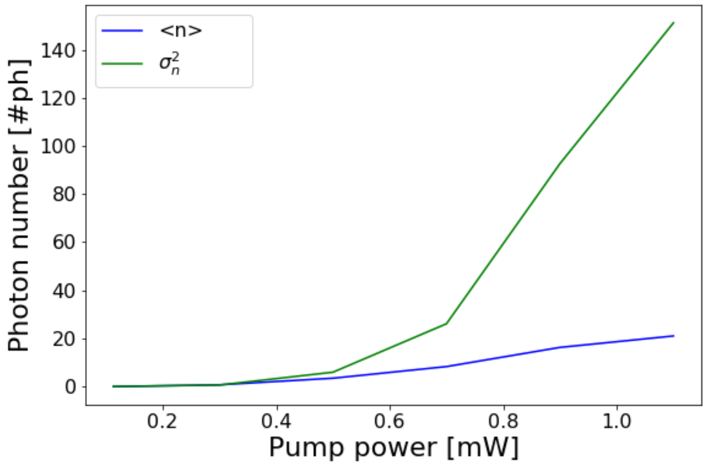

Figure 5.25: estimations performed on the pump second harmonic heterodyne data with Pattern Function Quantum Tomography. Photon number mean value (blue line) and variance (green line) are plotted as a function of the pump power. We see that the variance growth is much faster then the mean value one.

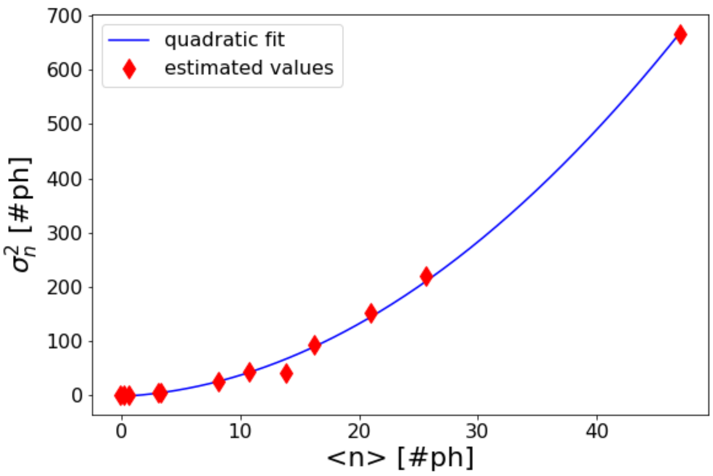

Figure 5.26: graph of the estimated variance vs the estimated mean photon number of the pump second harmonic heterodyne trace. We retrieve a quadratic relation (blue line) between the two quantities. This is qualitatively different from the coherent state linear behavior. Moreover, we can address the quadratic relation to the second harmonic generation process. Indeed, SHG involves second order polarization $P^{(2)}$, which has a quadratic dependence from the electric field.

In Appendix C we show that for a coherent state variance and photon number scale linearly (figure C.3). These two evidences confirm that the fundamental unity of the incoherent superposition we observe most likely isn't a coherent state.

A possible explanation of the quadratic behavior retrieved in figure 5.26 can be the non linearity of the second harmonic generation process. Indeed, SHG involves second order polarization field:

$$P^{(2)} = \epsilon_0 \chi^{(2)} E^2$$

that has a quadratic dependence from the electric field (and hence from the number of photons). Anyway, these are just conjectures that will be tested by future studies. The work of this thesis stops at the characterization of the generated state.

Photon number vs CEP

As a conclusion of the Chapter, we present in table 5.2 estimations of the pump second harmonic heterodyne data acquired with the CEP switched on/off both in the presence/absence of signal. To perform these estimations we use the set of data presented in section 5.4.1 (figures 5.20 and 5.21).

data	CEP	$\langle\hat{n}\rangle$	$\sigma^2_{\hat{n}}$
sig	off	17.36 ± 0.07	115.69 ± 3.35
sig	on	12.31 ± 0.06	96.37 ± 2.26
no sig	off	17.02 ± 0.07	95.02 ± 2.95
no sig	on	7.72 ± 0.04	53.38 ± 1.42

Table 5.2: estimations of mean value and variance photon number when the CEP system is switched on/off. For both cases, we present the results obtained in the presence/absence of the signal beam.

In order to understand the estimations presented in table 5.2, we first look at the results obtained in the absence of the phase stabilization system (CEP off).

We notice that mean photon number in the presence of signal differs from the estimation with the signal stopped by a value of

$$\langle\hat{n}\rangle_{sig} - \langle\hat{n}\rangle_{no\ sig} = 0.34 \pm 0.1\ ph \tag{5.9}$$

This value estimates the number of photons in the heterodyne trace when the pump is stopped. If we compare it with the LO + signal estimation[16] (0.47 ± 0.02 *photons*), we retrieve a good agreement between the two. This proves the accuracy of Pattern Function Tomography for photon number estimations.

We now look at the estimations performed on data acquired with the phase stabilization system switched on.

We notice that both with and without the signal, CEP usage diminishes the number of photons detected. This reflects into a fall of the variance too. We address this feature to a non ideal stabilization efficiency of the system, i.e. not every photon coming out of the laser + CEP system has a stable phase. Our hypothesis is that the interferential heterodyne signal is washed out by the phase noise.

In conclusion, we employed Pattern Function Tomography to estimate some state features, most importantly photon number and the related variance. We found out that there isn't a linear dependence between these two quantities, as one would expect for a coherent state. Moreover, variance grows quadratically with mean photon number. We attributed this behavior to the second harmonic generation process, because of the involvement of the quadratic electric field.

Finally, photon number estimations unveiled that, when CEP is switched on, some photons get lost. We associated this loss to a stabilization inefficiency of the system.

[16] This quantity isn't reported in table 5.2.

Conclusions

A typical approach to address low energy excitations in solids is pump and probe spectroscopy. In this technique, an ultrashort laser pulse (pump) impinges on the sample to excite the system and then, after a variable time delay, a second ultrashort pulse (probe) interacts with the system out-of-equilibrium. Standard pump-probe techniques measure the intensity of the output probe, addressing its spectral modifications as a function of time delay to the system excitations dynamics.

However, in these kind of experiments all the information encoded in the spectral phase is lost, since intensity is determined just by the electric field amplitude. In this thesis we have overcome this limitation by mean of an interferometric technique named Balanced Heterodyne Detection (BHD) which has been coupled to the standard pump-probe set-up.

In a BHD scheme, the optical field under investigation (signal) is mixed in a 50:50 beam splitter (whence the attribute balanced) with a strong classical field (local oscillator) whose phase is tunable. In a BHD experiment, the measured observable is the intensity of the differential photon current (heterodyne trace) between the two outcoming branches of the beam splitter. By looking at the evolution of the heterodyne trace as a function of the relative phase between signal and local oscillator, we're able to reconstruct both in amplitude and phase the quadrature field, a representative observable of the electric field. Therefore, the combination of pump-probe spectroscopy with Balanced Heterodyne Detection provides a full reconstruction of probe amplitude and phase dynamics.

Nonetheless, potentialities of our setup do not limit to phase and time-resolved measurements. Indeed, we exploit the broad spectral content of ultrashort light pulses to perform a frequency-resolved measurement. In particular, we implement two different Multimode Heterodyne Detection configurations:

- the first configuration employs two multi channel detectors, each one consisting in an array of photodiodes. To acquire independently probe modes, each beam exiting from the BHD 50:50 beam splitter is dispersed by mean of a prism and impinges on the photodiode array with its spectral components spatially separated. Thus, every detector pixel measures a different portion of the pulse spectrum, frequency-resolving the measurement.
- the second configuration uses a single channel differential detector characterized by a low electronic noise. Since a simultaneous acquisition of the different pulse modes can't be accomplished, we acquire a pulse mode at a time scanning the entire pulse spectrum. In order to modulate pulses spectral content, we employ a programmable ultrafast pulse shaper.

In this thesis we first exploit Multimode Heterodyne Detection to study how photon-phonon coupling is mapped on mean values of amplitude and phase of each probe mode. We apply this approach to $\alpha-$quartz to find in the probe spectral features direct signature of the phonon.

Amplitude and phase exhibit two different frequency-dependent responses as a function of the pump-probe time delay:

- the phase of all the probe modes oscillates at the frequency of the excited phonon. This phase trend is due to a linear modulation of the refractive index ruled by the phonon oscillations (Linear Refractive Modulation).

- the amplitude oscillations exhibit a frequency-dependence that results in a time-dependent spectral shift. These spectral shifts are imprinted on the probe spectrum by Impulsive Stimulated Raman Scattering (ISRS).

Furthermore, our detection system provides a shot by shot pulse acquisition that enables the access to the full statistics of the measurement. Moreover, the differential acquisition in balanced conditions permits to kill classical noise and hence to work in shot-noise regime. For this reason, the detected signal fluctuations pertain to the intrinsic quantum nature of light.

We exploit these features of our Multimode Heterodyne Detection setup to perform a fluctuation study on the pump second harmonic generation process. This study is performed with the pump in resonance condition, i.e. with an overlap between the pump second harmonic and the local oscillator spectra. Measurement distribution exhibits a non trivial behavior:

- for the frequencies in the overlap region the measurement distribution isn't described by a standard gaussian profile but presents a bimodal feature. The bimodal distribution has two symmetrical peaks and a valley in correspondence of the mean value.
- the distance between the two peaks, and hence the spread of the distribution, increases with the number of photons in the pump pulse.
- bimodal distribution is replaced by a standard gaussiam distribution if the laser phase stabilization system is switched on.

In the model we propose, bimodal distribution doesn't take origin from the pump distribution, since the latter is single peaked, but from the random relative phase between pump second harmonic and local oscillator. This phase uncertainty generates an incoherent superposition of phase-randomized quantum states. Fixing the relative phase between pump and local oscillator by means of Carrier-Envelope Phase stabilization system fixes also the phase of the measured quantum states. Quantitative estimations performed with Pattern Function Quantum Tomography suggest that random phase states that give rise to the incoherent superposition most likely aren't coherent states.

As future perspectives, we propose two different possibilities. The first one consists in a continuation of the fluctuation study of the pump second harmonic generation process. In particular, we would like to address the nature of phase randomized states by means of other tomographic techniques, like *Wigner function reconstruction*. Since phase-averaged coherent states are of common use in quantum information [20], we should also understand if the generation process we use to determine phase uncertainty could be of interest for the community.

As a second perspective, both the mean value and the fluctuation approach could be used to investigate complex materials. In particular, other members of our research group have characterized cuprates samples, a class of superconducting materials, by means of pump-probe [25] or pump-push-probe experiments [26]. However, Multimode Heterodyne Detection could provide additional information for these systems. In particular, addressing separately amplitude and phase probe dynamics could possibly unveil non trivial features of the pseudo-gap phase.

Riassunto

Il tipico approccio utilizzato per lo studio delle eccitazioni a bassa energia nei materiali è la spettroscopia pump-probe. In questa tecnica un impulso di luce ultracorto (probe) incide sul campione con lo scopo di eccitare il sistema. Dopo un intervallo di tempo arbitrario, un secondo impulso ultracorto (probe) interagisce con il sistema fuori equilibrio e viene successivamente rivelato.

Esperimenti standard di spettroscopia pump-probe misurano l'intenistà del campo elettrico dell'impulso di probe. Una misura standard di intensità però non resituisce una rappresentazione completa del campo elettrico. Infatti, l'informazione di fase spettrale viene completamente persa, dal momento che l'intensità dipende solo dall'ampiezza del campo. In questa tesi abbiamo superato questo limite accoppiando la spettroscopia pump-probe alla tecnica interferometrica chiamata *Detezione Eterodina Bilanciata* (BHD).

In uno schema di BHD il campo investigato (segnale) interferisce in un beam splitter 50:50 (da questo rapporto deriva l'appellativo di *bilanciata*) con un più intenso campo classico (oscillatore locale) di cui si può controllare la fase. L'osservabile misurata in un esperimento di Detezione Eterodina Bilanciata è la corrente di fotoni differenziale (corrente eterodina) dei bracci uscenti dal beam splitter. Guardando al comportamento della corrente eterodina in funzione della fase relativa tra segnale e oscillatore locale siamo in grado di ricostruire il campo quadratura, un osservabile rappresentativa del campo elettrico. Quindi la combinazione di detezione eterodina e spettroscopia pump-probe ci restituisce una ricostruzione delle dinamiche di ampiezza e fase dell'impulso di probe.

Tuttavia, la potenzialità del nostro setup non si limita alla risoluzione in tempo e in fase delle misure. Infatti, sfruttando l'ampia larghezza di banda degli impulsi ultracorti, siamo in grado di effettuare delle misure risolte in frequenza. In particolare, nel nostro setup abbiamo implementato due configurazioni:

- la prima configurazione utilizza due detector a multi canale: nello specifico, ogni detector è costituito da un array di fotodiodi. Per misurare indipendentemente i diversi modi del probe, ognuno dei due fasci uscenti dal beam splitter 50:50 viene disperso tramite un prisma. In questa maniera, il fascio che incide sull'array di fotodiodi presenta le varie componenti spettrali separate spazialmente. Di conseguenza, ogni pixel del detector vede una componente spettrale dell'impulso diversa e la misura viene risolta in frequenza.
- la seconda configurazione utilizza un detector differenziale a singolo canale caratterizzato da un basso rumore elettronico. Dal momento che in questa configurazione non si può effettuare un'acquisizione simultanea delle diverse componenti spettrali, acquisiamo singolarmente un modo alla volta effettuando poi uno scan delle frequenze dell'impulso. Per fare ciò, moduliamo il contenuto spettrale dell'oscillatore locale tramite un modulatore di impulsi programmabile (pulse shaper).

In questa tesi sfruttiamo la Detezione Eterodina Multimodo per studiare come l'accoppiamento fotone-fonone si riflette nelle mappe di valor medio di ampiezza e fase spettrale del probe. Per trovare una traccia diretta della presenza del fonone nelle modifiche spettrali del probe, utilizziamo un campione di $\alpha-$quarzo.

Ampiezza e fase mostrano due risposte diverse per le varie frequenze in funzione del ritardo dalla pompa:

- la fase di tutti i modi del probe oscilla alla frequenza del fonone eccitato tramite pompa. Questo comportamento uniforme della fase è determinato da una modulazione lineare dell'indice di rifrazione del campione.
- le oscillazioni in ampiezza mostrano una dipendenza dalla frequenza che risulta in una redistribuzione del peso spettrale dipendente dal tempo. Questo rimescolamento delle frequenze all'interno dell'impulso di probe è determinato dal fenomeno di Impulsive Stimulated Raman Scattering.

L'approccio di valor medio non è tuttavia l'unico possibile con il nostro setup. Infatti, il nostro sistema di detezione fa un acquisizione impulso per impulso, rendendoci accessibile l'intera statistica della misura. Inoltre, l'acquisizione differenziale bilanciata permette di ridurre drasticamente il contributo di rumore classico permettendoci di lavorare in regime di shot-noise. Di conseguenza, le fluttuazioni che misuriamo sono quelle direttamente legate alla natura quantistica della luce.

Sfruttando queste caratteristiche, in questa tesi presentiamo uno studio delle fluttuazioni nel processo di generazione di seconda armonica dell'impulso di pompa. Questo esperimento viene realizzato in condizioni di risonanza, ovvero lo spettro della seconda armonica della pompa e quello dell'oscillatore locale presentano una regione di sovrapposizione. La distribuzione della misura presenta le seguenti caratteristiche:

- per la regione di frequenze dove seconda armonica e oscillatore locale si sovrappongono, la distribuzione della misura non è descritta da una gaussiana ma da un profilo bimodale. Questa distribuzione presenta due picchi simmetrici e una valle in corrispondenza del valor medio.
- la distanza tra i due picchi, e quindi l'allargamento della distribuzione, aumenta con l'aumentare del numero di fotoni nella pompa.
- la distribuzione bimodale viene sostituita da una gaussiana quando il sistema di stabilizzazione della fase degli impulsi viene attivato.

Nel modello che proponiamo la distribuzione bimodale non è determinata dalla distribuzione della pompa, che infatti ha un profilo gaussiano, ma dalla fase relativa casuale tra seconda armonica della pompa e oscillatore locale. Questa indeterminazione di fase genera una sovrapposizione incoerente di stati quantistici a fase casuale. Fissare la fase relativa tra seconda armonica e oscillatore locale tramite il sistema di stabilizzazione permette di fissare anche la fase di questo stato generato. In conclusione, stime quantitative effettuate tramite Pattern Function Quantum Tomography suggeriscono che lo stato a fase casuale che generiamo non sia una sovrapposizione di stati coerenti.

Come conclusione presentiamo due prospettive di sviluppo per quanto concerne questo lavoro di tesi. Il primo consiste nell'estendere le analisi quantitative effettuate sullo studio di generazione di seconda armonica ad altre tecniche di tomografia, come la ricostruzione della funzione di Wigner. In questo modo si potrebbero integrare i risultati ottenuti con la Pattern Function Quantum Tomography per discriminare definitivamente se gli stati a fase casuale siano o meno degli stati coerenti. Inoltre, dal momento che gli stati coerenti a fase casuale vengono utilizzati nell'ambito dell'informazione quantistica [20], vorremmo anche capire se il metodo che utilizziamo per generare le sovrapposizioni incoerenti possa essere di interesse per quel campo.

Come seconda prospettiva, sia l'approccio di valor medio che quello con le fluttuazioni potrebbe essere utilizzato per investigare materiali complessi. Nello specifico, altri membri del nostro gruppo di ricerca hanno caratterizzato dei campioni di cuprati, una classe di materiali superconduttori, tramite esperimenti pump-probe [25] e pump-push-probe [26]. In quest'ottica, la Detezione Eterodina Multimodo potrebbe fornire informazioni addizionali su questi sistemi. In particolare, studiare separatamente le dinamiche di ampiezza e fase del probe potrebbe rivelare proprietà non banali della fase di pseudo-gap.

Appendices

Appendix A

A Beam Splitter Model for Heterodyne Detection

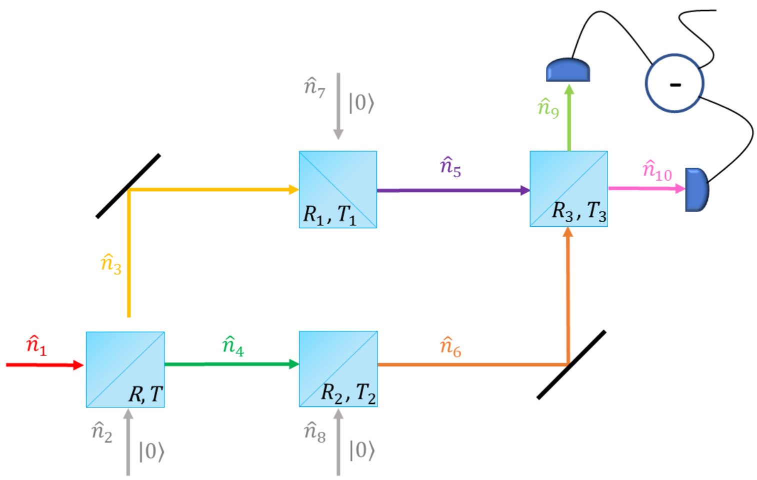

Figure A.1: scheme of a Balanced Heterodyne Detection setup where, according to the Beam Splitter Model, every optical element is substituted by a beam splitter. The first beam splitter divides the initial beam into signal and local oscillator, the following two (labelled 1 and 2) simulate dissipation on the two optical paths and finally the last beam splitter (labelled 3) recombines signal and LO to perform the differential photon current measurement.

In this Appendix we present the extension of the Beam Splitter Model [6] to a Balanced Heterodyne Detection setup (figure A.1). To schematize it, we use 4 different beam splitters: the first one divides the initial beam into signal and local oscillator, the following two (labelled 1 and 2) simulate dissipation on the two optical paths and finally the last beam splitter (labelled 3) recombines signal and LO to perform the measurement. Using the notation reported in figure A.1, the creation operators $\hat{a}_i$ can be written:

$$\begin{aligned}
\hat{a}_3 &= R\hat{a}_1 + T\hat{a}_2 \\
\hat{a}_4 &= T\hat{a}_1 + R\hat{a}_2 \\
\hat{a}_5 &= T_1\hat{a}_3 + R_1\hat{a}_7 = T_1R\hat{a}_1 + T_1T\hat{a}_2 + R_1\hat{a}_7 \\
\hat{a}_6 &= T_2\hat{a}_4 + R_2\hat{a}_8 = T_2T\hat{a}_1 + T_2R\hat{a}_2 + R_2\hat{a}_8 \\
\hat{a}_9 &= R_3\hat{a}_5 + T_3\hat{a}_6 = R_3T_1R\hat{a}_1 + R_3T_1T\hat{a}_2 + R_3R_1\hat{a}_7 + T_3T_2T\hat{a}_1 + T_3T_2R\hat{a}_2 + T_3R_2\hat{a}_8 \\
\hat{a}_{10} &= T_3\hat{a}_5 + R_3\hat{a}_6 = T_3T_1R\hat{a}_1 + T_3T_1T\hat{a}_2 + T_3R_1\hat{a}_7 + R_3T_2T\hat{a}_1 + R_3T_2R\hat{a}_2 + R_3R_2\hat{a}_8
\end{aligned}$$

Since $\hat{n}_i = \hat{a}_i^\dagger \hat{a}_i$ and $\langle \hat{n}_2 \rangle = \langle \hat{n}_7 \rangle = \langle \hat{n}_8 \rangle = 0$, we can easily calculate the differential photon current measured on the detector:

$$\begin{aligned}
\langle \hat{I} \rangle &= \langle \hat{n}_{9-10} \rangle = \langle \hat{n}_9 \rangle - \langle \hat{n}_{10} \rangle \\
&= \left[\left(|T_1|^2|R|^2 - |T_2|^2|T|^2 \right) \left(|R_3|^2 - |T_3|^2 \right) - 4|R_3||T_3||T_1||T_2||R||T| cos(\Phi_{T1} - \Phi_{T2}) \right] \langle \hat{n}_1 \rangle
\end{aligned}$$

that in case of balanced detection ($|R_3|^2 = |T_3|^2 = 1/2$) becomes:

$$\langle \hat{I} \rangle = |T_1||T_2||R||T| cos(\Phi_{T1} - \Phi_{T2} + \pi) \langle \hat{n}_1 \rangle \tag{A.1}$$

To obtain the upper formulae, we substituted $T_1 = |T_1| e^{\Phi_{T1}}$[1], $T_2 = |T_2| e^{\Phi_{T2}}$, and we set for the first beam splitter

$$\begin{pmatrix} Re^{i\Phi_R} & Te^{i\Phi_T} \\ Te^{i\Phi_T} & Re^{i\Phi_R} \end{pmatrix}$$

and for the last one

$$\begin{pmatrix} R_3e^{i\Phi_{R3}} & T_3e^{i\Phi_{T3}} \\ T_3e^{i\Phi_{T3}} & R_3e^{i\Phi_{R3}} \end{pmatrix}$$

with the condition $\Phi_{R3} - \Phi_{T3} = \Phi_R - \Phi_T = \pi/2$[2]. We underline that in general, the phase shifts experienced by the incoming beams are different (i.e. the phases of the four beam splitter matrix elements are all different). Instead, we're imposing the same phase shift for the two transmitted/reflected beams. This doesn't infer on the result, since we're interested in the variation of the relative phase between the signal and the local oscillator beams, and not in its absolute value.

Given the well known variance formula:

$$\sigma^2_{9-10} = \langle \hat{n}^2_{9-10} \rangle - \langle \hat{n}_{9-10} \rangle^2 = \langle \hat{n}^2_9 \rangle + \langle \hat{n}^2_{10} \rangle - \langle \hat{n}_9 \hat{n}_{10} \rangle - \langle \hat{n}_{10} \hat{n}_9 \rangle - \langle \hat{n}_9 \rangle^2 - \langle \hat{n}_{10} \rangle^2 + 2 \langle \hat{n}_9 \rangle \langle \hat{n}_{10} \rangle$$

we obtain:

$$\sigma^2_{9-10} = \frac{\sigma^2_1 - \langle \hat{n}_1 \rangle}{\langle \hat{n}_1 \rangle^2} \langle \hat{n}_{9-10} \rangle^2 + \left(|T_1|^2|R|^2 + |T_2|^2|T|^2 \right) \langle \hat{n}_1 \rangle \tag{A.2}$$

where we can clearly distiguish a classical component, depending on the measured intensity $\langle \hat{n}_{9-10} \rangle$, and a quantistic one related to the initial beam number of photons $\langle \hat{n}_1 \rangle$.

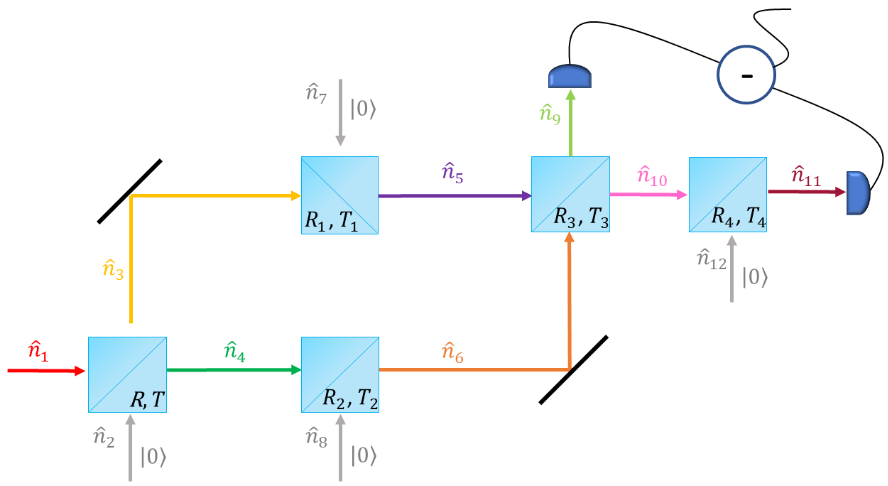

Figure A.2: scheme of a real Balanced Heterodyne Detection setup, where the recombining beam splitter (labelled 3) isn't a perfect 50:50 one. In order to achieve balanced detection, dissipative elements (represented by beam splitter 4) are inserted along the more intense beam.

[1] In this framework, Φ_{T1} indicates the phase shift that the trasmitted beam experiences on beam splitter 1.

[2] This condition comes from the imposition of the photon number conservation (equation 2.X)

When we deal with real optical elements, we have to consider that a perfect 50:50 recombining beam splitter (labelled 3) doesn't exist. Therefore, we have to introduce dissipative elements along the more intense final beam in order to perform a balanced measurement. To schematize this setup (figure A.2), we introduce a fifth beam splitter (labelled 4). Following the same procedure operated before, we obtain:

$$\begin{aligned}\langle\hat{I}\rangle &= \langle\hat{n}_{9-11}\rangle = \langle\hat{n}_9\rangle - \langle\hat{n}_{11}\rangle \\ &= \Big[|R_3|^2\Big(|T_1|^2|R|^2 - |T_4|^2|T_2|^2|T|^2\Big) - |T_3|^2\Big(|T_4|^2|T_1|^2|R|^2 - |T_2|^2|T|^2\Big) \\ &- 2|R_3||T_3||T_1||T_2||R||T|\Big(1+|T_4|^2\Big)cos(\Phi_{T1}-\Phi_{T2})\Big]\langle\hat{n}_1\rangle\end{aligned}$$

and

$$\begin{aligned}\sigma^2_{9-11} &= \frac{\sigma_1^2 - \langle\hat{n}_1\rangle}{\langle\hat{n}_1\rangle^2}\langle\hat{n}_{9-11}\rangle^2 + \Big[|T_1|^2|R|^2\Big(1-|T_3|^2\Big(1-|T_4|^2\Big)\Big) + |T_2|^2|T|^2\Big(1-|R_3|^2\Big(1-|T_4|^2\Big)\Big) \\ &- 2cos(\Phi_{T1}-\Phi_{T2})|R_3||T_3||T_1||T_2||R||T|\Big(1-|T_4|^2\Big)\Big]\langle\hat{n}_1\rangle\end{aligned}$$

We underline that, by substituting $|T_4|^2 = 1$, we obtain again the no dissipation equations A.1 and A.2.

Appendix B

A Beam Splitter Model for Balanced Heterodyne Detection with polarizing beam splitters

In this section, we provide an extension of Beam Splitter Model (figure 3.1) to light with arbitrary polarization. In particular, we're interested in modelling the configuration with polarizing beam splitters we use to perform balanced detection (section 2.3).

The first thing we have to introduce is the unitary operator whose action is the one of a polarizing beam splitter (PBS). We recall that a polarizing beam splitter is an optical element that splits an incoming beam into two beams with orthogonal polarization. To take into account different polarizations, we represent the PBS action by a 4x4 matrix[1]:

$$\hat{U}_{PBS} = \begin{pmatrix} R_x & 0 & T_x & 0 \\ 0 & R_y & 0 & T_y \\ T_x & 0 & R_x & 0 \\ 0 & T_y & 0 & R_y \end{pmatrix} \tag{B.1}$$

where R_x, R_y, T_x, T_y are respectively reflectivity and transmittance coefficients for the two orthogonal polarizations x and y.

Therefore, the action of a PBS on an incoming beam[2] arbitrarily polarized $(\hat{a}_x, \hat{a}_y)$ will be:

$$\begin{pmatrix} R_x & 0 & T_x & 0 \\ 0 & R_y & 0 & T_y \\ T_x & 0 & R_x & 0 \\ 0 & T_y & 0 & R_y \end{pmatrix} \begin{pmatrix} \hat{a}_x \\ \hat{a}_y \\ \hat{b}_x \\ \hat{b}_y \end{pmatrix} = \begin{pmatrix} \hat{c}_x \\ \hat{c}_y \\ \hat{s}_x \\ \hat{s}_y \end{pmatrix} = \begin{pmatrix} R_x\hat{a}_x + T_x\hat{b}_x \\ R_y\hat{a}_y + T_y\hat{b}_y \\ T_x\hat{a}_x + R_x\hat{b}_x \\ T_y\hat{a}_y + R_y\hat{b}_y \end{pmatrix}$$

In order to have equation B.1 describing the action of a polarizing beam splitter, coefficients must assume values:

$$\begin{aligned} |T_x|^2 &>> |R_x|^2 \\ |R_y|^2 &>> |T_y|^2 \end{aligned} \tag{B.2}$$

Typical values[3] are $|T_x|^2 = 0.95$ and $|R_y|^2 = 0.99$.

[1] The matrix is 4−dimensional because there are two beam splitter entries (and of course two exits), and each of them has a polarization that is described by a linear combination of two orthogonal polarizations (x and y).

[2] Of course, in the Beam Splitter Model formalism, we have to take into account also the second entry $(\hat{b}_x, \hat{b}_y)$, that will be in a vacuum state $|0\rangle$.

[3] We underline that, with $|T_x| < 1$ and $|R_y| < 1$, we're describing the action of a real polarizing beam splitter, i.e. a PBS where the two outcoming beams are not the perfect split of the two incoming orthogonally polarized components.

Moreover, our balancing setup employs a Half Wave Plate, whose action has to be represented by a matrix too. We recall that a Half Wave Plate is an optical element that rotates the polarization of an incoming beam. The operator we obtain can be written as:

$$\hat{U}_{HWP} = \begin{pmatrix} R_x & 0 & T_x cos\theta & T_y sin\theta \\ 0 & R_y & -T_x sin\theta & T_y cos\theta \\ T_x cos\theta & -T_y sin\theta & R_x & 0 \\ T_x sin\theta & T_y cos\theta & 0 & R_y \end{pmatrix} \tag{B.3}$$

We underline that Half Wave Plate produces a single outcoming beam, and therefore could be represented by a 2x4 matrix[4]. However, the 4x4 representation takes into account dissipation and enables us to impose photon number conservation. Imposition of photon number conservation in equation B.3 gives rise to the following conditions[5]:

$$\begin{aligned} &|T_x|^2 + |R_x|^2 = 1 \\ &|T_y|^2 + |R_y|^2 = 1 \\ &T_x^* R_x + R_x^* T_x = 0 \\ &T_y^* R_y + R_y^* T_y = 0 \\ &T_x^* R_y + R_y^* T_x = 0 \\ &T_y^* R_x + R_x^* T_y = 0 \end{aligned}$$

Now that we have introduced all optical components representation, we can move to our balancing setup (figure B.1). Two beams orthogonally polarized impinge on a PBS, where they are recombined. Subsequently, a Half Wave Plate rotates the polarization of the beam. Then, a second PBS splits the two ortogonal polarizations that are finally acquired by two photodiodes arrays (a mirror is placed along one of the two optical paths to reach the detector). We can now calculate, similarly to what we did in Appendix A, the final annihilation operators in order to compute mean heterodyne current and the related variance.

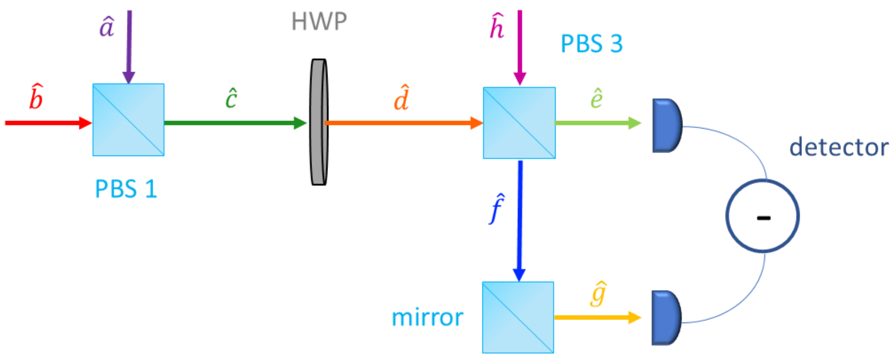

Figure B.1: scheme of the balancing configuration with polarizing beam splitters adopted.

With two initial beams $(\hat{a}_x, \hat{a}_y)$ and $(\hat{b}_x, \hat{b}_y)$, after the propagation through optical elements, we get:

[4]We always have to consider two incoming beams, even if HWP acts on a single one, in order to simulate the quantum noise introduced by the optical element.

[5]We underline that equation B.3 is a sort of extension of equation B.1 to inefficiencies that rotate polarization of an exiting beam. Therefore, conditions for equation B.1 are a subset of Half Wave Plate matrix conditions.

$$\begin{pmatrix}\hat{e}_x\\ \hat{e}_y\end{pmatrix} = \begin{pmatrix}A_1\hat{a}_x + A_2\hat{b}_x + A_3\hat{a}_y + A_4\hat{b}_y + A_5\hat{m}_x + A_6\hat{h}_x\\ B_1\hat{a}_x + B_2\hat{b}_x + B_3\hat{a}_y + B_4\hat{b}_y + B_5\hat{m}_y + B_6\hat{h}_y\end{pmatrix}$$

$$\begin{pmatrix}\hat{g}_x\\ \hat{g}_y\end{pmatrix} = \begin{pmatrix}C_1\hat{a}_x + C_2\hat{b}_x + C_3\hat{a}_y + C_4\hat{b}_y + C_5\hat{m}_x + C_6\hat{h}_x + C_7\hat{l}_x\\ D_1\hat{a}_x + D_2\hat{b}_x + D_3\hat{a}_y + D_4\hat{b}_y + D_5\hat{m}_y + D_6\hat{h}_y + D_7\hat{l}_y\end{pmatrix}$$

where operators coefficients are:

$$A_1 = R_{x1}T_{x2}T_{x3}cos\theta\ ; \quad A_2 = T_{x1}T_{x2}T_{x3}cos\theta\ ; \quad A_3 = -R_{y1}T_{y2}T_{x3}sin\theta\ ;$$
$$A_4 = -T_{y1}T_{y2}T_{x3}sin\theta\ ; \quad A_5 = R_{x2}T_{x3}\ ; \quad A_6 = R_{x3}$$

$$B_1 = R_{x1}T_{x2}T_{y3}sin\theta\ ; \quad B_2 = T_{x1}T_{x2}T_{y3}sin\theta\ ; \quad B_3 = R_{y1}T_{y2}T_{y3}cos\theta\ ;$$
$$B_4 = T_{y1}T_{y2}T_{y3}cos\theta\ ; \quad B_5 = R_{y2}T_{y3}\ ; \quad B_6 = R_{y3}$$

$$C_1 = R_{x1}T_{x2}R_{x3}R_{x4}cos\theta\ ; \quad C_2 = T_{x1}T_{x2}R_{x3}R_{x4}cos\theta\ ; \quad C_3 = -R_{y1}T_{y2}R_{x3}R_{x4}sin\theta\ ;$$
$$C_4 = -T_{y1}T_{y2}R_{x3}R_{x4}sin\theta\ ; \quad C_5 = R_{x2}R_{x3}R_{x4}\ ; \quad C_6 = T_{x3}R_{x4}\ ; \quad C_7 = T_{x4}$$

$$D_1 = R_{x1}T_{x2}R_{y3}R_{y4}sin\theta\ ; \quad D_2 = T_{x1}T_{x2}R_{y3}R_{y4}sin\theta\ ; \quad D_3 = R_{y1}T_{y2}R_{y3}R_{y4}cos\theta\ ;$$
$$D_4 = T_{y1}T_{y2}R_{y3}R_{y4}cos\theta\ ; \quad D_5 = R_{y2}R_{y3}R_{y4}\ ; \quad D_6 = T_{y3}R_{y4}\ ; \quad D_7 = T_{y4}$$

Labels 1, 2, 3 and 4 indicate respectively the first polarizing beam splitter, the Half Wave Plate, the second PBS and the final mirror. Considering the initial beams linearly polarized with orthogonal polarizations (i.e. $\langle\hat{n}_{ax}\rangle = \langle\hat{n}_{by}\rangle = 0$), we obtain an heterodyne current of the form:

$$\langle\hat{n}_{e-g}\rangle = \langle\hat{n}_1\rangle + \langle\hat{n}_2\rangle + \langle\hat{n}_3\rangle + \langle\hat{n}_4\rangle \tag{B.4}$$

where the four $\langle\hat{n}_i\rangle$ components are:

$$\begin{aligned}
\langle\hat{n}_1\rangle &= |T_{x1}|^2|T_{x2}|^2\Big(|T_{x3}|^2cos^2\theta + |T_{y3}|^2sin^2\theta - |R_{x3}|^2|R_{x4}|^2cos^2\theta - |R_{y3}|^2|R_{y4}|^2sin^2\theta\Big)\langle\hat{n}_{bx}\rangle\\
\langle\hat{n}_2\rangle &= |R_{y1}|^2|T_{y2}|^2\Big(|T_{x3}|^2sin^2\theta + |T_{y3}|^2cos^2\theta - |R_{x3}|^2|R_{x4}|^2sin^2\theta - |R_{y3}|^2|R_{y4}|^2cos^2\theta\Big)\langle\hat{n}_{ay}\rangle\\
\langle\hat{n}_3\rangle &= T^*_{x1}R_{y1}T^*_{x2}T_{y2}sin\theta cos\theta\Big(-|T_{x3}|^2 + |T_{y3}|^2 - |R_{x3}|^2|R_{x4}|^2 + |R_{y3}|^2|R_{y4}|^2\Big)\langle\hat{b}^\dagger_x\hat{a}_y\rangle\\
\langle\hat{n}_4\rangle &= T_{x1}R^*_{y1}T_{x2}T^*_{y2}sin\theta cos\theta\Big(-|T_{x3}|^2 + |T_{y3}|^2 - |R_{x3}|^2|R_{x4}|^2 + |R_{y3}|^2|R_{y4}|^2\Big)\langle\hat{b}_x\hat{a}^\dagger_y\rangle
\end{aligned}$$

Considering dominant terms (equation B.2), heterodyne current reduces to :

$$\begin{aligned}
\langle\hat{n}_{e-g}\rangle &= |T_{x1}|^2|T_{x2}|^2\Big(|T_{x3}|^2cos^2\theta - |R_{y3}|^2|R_{y4}|^2sin^2\theta\Big)\langle\hat{n}_{bx}\rangle +\\
&+ |R_{y1}|^2|T_{y2}|^2\Big(|T_{x3}|^2sin^2\theta - |R_{y3}|^2|R_{y4}|^2cos^2\theta\Big)\langle\hat{n}_{ay}\rangle +\\
&+ T^*_{x1}R_{y1}T^*_{x2}T_{y2}sin\theta cos\theta\Big(-|T_{x3}|^2 + |R_{y3}|^2|R_{y4}|^2\Big)\langle\hat{b}^\dagger_x\hat{a}_y\rangle +\\
&+ T_{x1}R^*_{y1}T_{x2}T^*_{y2}sin\theta cos\theta\Big(-|T_{x3}|^2 + |R_{y3}|^2|R_{y4}|^2\Big)\langle\hat{b}_x\hat{a}^\dagger_y\rangle
\end{aligned}$$

If we perform the same calculations for the variance, we obtain:

$$\sigma^2_{e-g} = \sum_i \left[\frac{\sigma^2_{\hat{n}_{ki}} - \langle\hat{n}_{ki}\rangle}{\langle\hat{n}_{ki}\rangle^2}\langle\hat{n}_i\rangle^2 + X_i\langle\hat{n}_i\rangle\right] + \sum_{i,j\neq i} C(\hat{n}_{ki},\hat{n}_{kj})\langle\hat{n}_i\rangle\langle\hat{n}_j\rangle \tag{B.5}$$

where we indicated with $\hat{n}_{kj}$ the four operators (in index ordering) $\hat{n}_{bx}$, $\hat{n}_{ay}$, $\hat{b}^\dagger_x\hat{a}_y$ and $\hat{b}_x\hat{a}^\dagger_y$, with $\sigma_{\hat{n}_{ki}}$ the variance of the operator $\hat{n}_{ki}$, with $C(\hat{n}_{ki},\hat{n}_{kj})$ the covariance of $\hat{n}_{ki}$ and $\hat{n}_{kj}$ and with X_i a constant resulting from a combination of reflectivity and transmittance coefficients.

Appendix C

Pattern Function Quantum Tomography for a coherent state

In Chapter 5 we introduced Pattern Function Tomography as a tool for estimating operators expectation values. This is done with an estimator $R[\hat{O}]$, according to:

$$\langle \hat{O} \rangle = \frac{1}{M} \sum_{k=1}^{M} R[\hat{O}](x_k; \phi_k) \tag{C.1}$$

where $(x_k; \phi_k)$ represents one of the M experimental heterodyne data pairs acquired. In order to find an expression of the estimators we need, we use the formula retrieved in [24] with a non-unitary quantum efficiency η:

$$R_\eta[(\hat{a}^\dagger)^n \hat{a}^m](x; \phi) = \frac{e^{i(m-n)\phi} H_{m+n}(\sqrt{\eta} x)}{\sqrt{(2\eta)^{m+n}} \binom{n+m}{m}} \tag{C.2}$$

Equation C.2 can be used to obtain the pattern functions of the quadrature operator $\hat{x}_\theta$ and of its square $\hat{x}_\theta^2$ at the specific phase θ. Considering the quadrature operator definition (equation 1.10), we find:

$$\begin{aligned} R[\hat{x}_\theta](x, \phi) &= \frac{R[(\hat{a}^\dagger)^0 \hat{a}^1](x, \phi) e^{-i\theta} + R[(\hat{a}^\dagger)^1 \hat{a}^0](x, \phi) e^{i\theta}}{\sqrt{2}} \\ &= 2x cos(\theta - \phi) \end{aligned}$$

We underline that θ is the phase of the quadrature that we're estimating, whereas ϕ is the phase of the experimental data. Therefore, from the same data set $\{(x_k; \phi_k),\ k = 1, \ldots, M\}$, we can estimate the quadrature expectation value at every phase $\phi \in [0, 2\pi]$. An example of $\hat{x}_\theta$ estimations for a coherent state is depiceted in figure C.1.

Figure C.1 shows a good agreement between the averaged experimental data of the signal heterodyne trace[1] (red line) and the mean values estimations performed with Pattern Function Tomography (blue line).

Following the same procedure that we used to find $R[\hat{x}_\theta](x, \phi)$, we can retrieve the estimator of $\hat{x}_\theta^2$

$$R[\hat{x}_\theta^2](x, \phi) = \frac{1}{2} \Big\{ 1 + \Big(2x^2 - \frac{1}{\eta}\Big) [4cos^2(\phi - \theta) - 1] \Big\}$$

and eventually find the variance $\sigma^2_{\hat{x}_\theta}$ using the well known property

$$\sigma^2_{\hat{x}_\theta} = \langle \hat{x}_\theta^2 \rangle - \langle \hat{x}_\theta \rangle^2$$

The comparison between experimental and estimated variance is shown in figure C.2.

[1] We recall that our signal is described by a light coherent state.

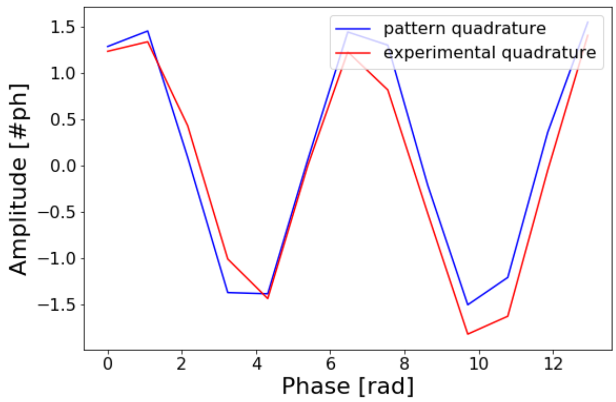

Figure C.1: comparison between experimental data (red) and pattern function estimations (blue) for the signal heterodyne trace mean value (i.e. a coherent state). We retrieve a good agreement between averaged values and estimated ones.

Looking at experimental data (red line of figure C.2), we see that variance values are kind of oscillating around 0.5, that is the variance reference value of a coherent state. Instead, variance values estimated with Pattern Function Tomography are underestimated and oscillate around a value lower than 0.5. This confirms the problems retrieved in Chapter 5 for the estimation of the quadrature variance.

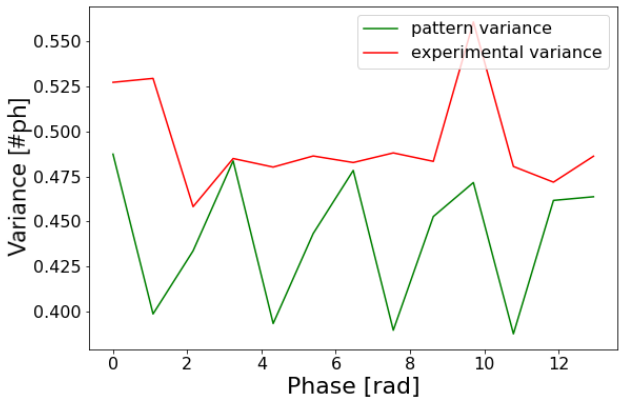

Figure C.2: comparison between experimental (red) and pattern function estimated variance (green). Experimental data exhibit non regular oscillations around the value of 0.5, the reference variance of a coherent state. On the contrary, estimated variance oscillates around a lower value, showing that in this case estimation didn't work properly.

However, we can estimate[2] two other important quantities, that are mean photon number $\langle \hat{n} \rangle$ and variance $\sigma^2_{\hat{n}} = \langle \hat{n}^2 \rangle - \langle \hat{n} \rangle^2$. The result is plotted in figure C.3.

We see that both photon number mean value (green line) and variance (blue line) exhibit a peak at 402 THz, perfectly matching LO/signal pulse frequencies (figure 5.10). Most importantly, figure C.3 shows that mean photon number and variance assume almost the same values. Since for a coherent state holds $\langle \hat{n} \rangle = \sigma^2_{\hat{n}} = |\alpha|^2$, Pattern Function Tomography estimations confirm that signal is in a coherent state.

[2]Estimators $R[\hat{O}]$ of $\hat{n}$ and $\hat{n}^2$ are reported in table 5.2.

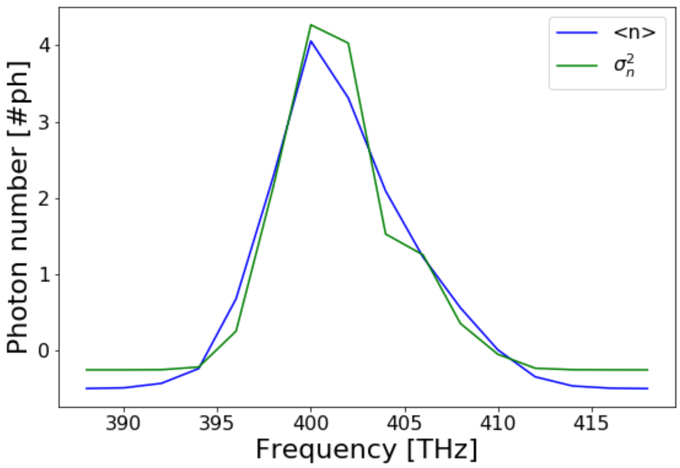

Figure C.3: comparison of photon number mean value (blue) and variance (green) as a function of the pulse frequencies. Both estimated quantities exhibit a peak at 402 THz, the central frequency of the LO/signal pulses (figure 5.10). Moreover, mean value and variance assume the same values, confirming that the measured state is a coherent one.

Bibliography

[1] U. Fano. “Description of States in Quantum Mechanics by Density Matrix and Operator Techniques”. *Reviews of Modern Physics* 29.1 (1957), pp. 74–93.

[2] M. O. Scully and M. S. Zubairy. *Quantum Optics*. Cambridge University Press, 1997.

[3] D.-G. Welsch, W. Vogel, and T. Opatrný. “II Homodyne Detection and Quantum-State Reconstruction”. *Progress in Optics*. Elsevier, 1999, pp. 63–211.

[4] R. Loudon. *The Quantum Theory of Light*. Oxford Science Publication, 1993.

[5] M. Esposito. “a new spectroscopic approach to collective excitations in solids: pump-probe quantum state tomography”. PhD Thesis. Italy: Università degli Studi di Trieste, 2016.

[6] F. Giusti. “Intensity and fluctuation dynamics in pump-probe experiments in complex materials”. PhD Thesis. Italy: Università degli Studi di Trieste, 2018.

[7] G. Jarc. “Multimode homodyne detection applied to time-resolved Raman spectroscopy”. Master Thesis. Italy: Università degli Studi di Trieste, 2019.

[8] A. Montanaro. “Noise Correlation Spectroscopy”. Master Thesis. Italy: Università degli Studi di Trieste, 2018.

[9] A. M. Weiner. “Femtosecond pulse shaping using spatial light modulators”. *Review of Scientific Instruments* 71.5 (2000), pp. 1929–1960.

[10] J. C. Vaughan, T. Hornung, T. Feurer, and K. A. Nelson. “Diffraction-based femtosecond pulse shaping with a two-dimensional spatial light modulator”. *Optics Letters* 30.3 (2005), p. 323.

[11] E. M. Rigoni. “Messa a punto di un modulatore di luce per il controllo di impulsi ultracorti”. Bachelor Thesis. Italy: Università degli Studi di Trieste, 2018.

[12] K.-X. Sun, E. K. Gustafson, M. M. Fejer, and R. L. Byer. “Polarization-based balanced heterodyne detection method in a Sagnac interferometer for precision phase measurement”. *Optics Letters* 22.17 (1997), p. 1359.

[13] J. Reichert, R. Holzwarth, T. Udem, and T. Hänsch. “Measuring the frequency of light with mode-locked lasers”. *Optics Communications* 172.1-6 (1999), pp. 59–68.

[14] H. Telle, G. Steinmeyer, A. Dunlop, J. Stenger, D. Sutter, and U. Keller. “Carrier-envelope offset phase control: A novel concept for absolute optical frequency measurement and ultrashort pulse generation”. *Applied Physics B* 69.4 (1999), pp. 327–332.

[15] D. J. Jones. “Carrier-Envelope Phase Control of Femtosecond Mode-Locked Lasers and Direct Optical Frequency Synthesis”. *Science* 288.5466 (2000), pp. 635–639.

[16] J. Appel, D. Hoffman, E. Figueroa, and A. I. Lvovsky. “Electronic noise in optical homodyne tomography”. *Physical Review A* 75.3 (2007).

[17] M. Esposito, F. Benatti, R. Floreanini, S. Olivares, F. Randi, K. Titimbo, M. Pividori, F. Novelli, F. Cilento, F. Parmigiani, and D. Fausti. “Pulsed homodyne Gaussian quantum tomography with low detection efficiency”. *New Journal of Physics* 16.4 (2014), p. 043004.

[18] F. Glerean, S. Marcantoni, G. Sparapassi, A. Blason, M. Esposito, F. Benatti, and D. Fausti. “Quantum model for impulsive stimulated Raman scattering”. *Journal of Physics B: Atomic, Molecular and Optical Physics* 52.14 (2019), p. 145502.

[19] F. Glerean, G. Jarc, A. Marciniak, F. Giusti, G. Sparapassi, A. Montanaro, E. M. Rigoni, J. O. Tollerud, and D. Fausti. "Time-resolved multimode heterodyne detection for dissecting coherent states of matter". *Optics Letters* 45.13 (2020), p. 3498.

[20] A. Allevi, M. Bondani, P. Marian, T. A. Marian, and S. Olivares. "Characterization of phase-averaged coherent states". *Journal of the Optical Society of America B* 30.10 (2013), p. 2621.

[21] A. Baltuška, T. Fuji, and T. Kobayashi. "Controlling the Carrier-Envelope Phase of Ultrashort Light Pulses with Optical Parametric Amplifiers". *Physical Review Letters* 88.13 (2002).

[22] G. M. D'ariano, M. G. A. Paris, and M. F. Sacchi. *Quantum tomography.* Vol. Advances in Imaging and Electron Physics 128. Elsvier Inc., 2003, pp. 205–308.

[23] S. Olivares. *introduction to generation, manipulation and characterization of optical quantum states.* Vol. Lecture Notes. 2018.

[24] T. Richter. "Determination of field correlation functions from measured quadrature component distributions". *Physical Review A* 53.2 (1996), pp. 1197–1199.

[25] F. Giusti, A. Marciniak, F. Randi, G. Sparapassi, F. Boschini, H. Eisaki, M. Greven, A. Damascelli, A. Avella, and D. Fausti. "Signatures of Enhanced Superconducting Phase Coherence in Optimally Doped $Bi_2Sr_2Y_{0.08}Ca_{0.92}Cu_2O_{8+\delta}$ Driven by Midinfrared Pulse Excitations". *Phys. Rev. Lett.* 122 (2019), p. 067002.

[26] A. Montanaro, F. Giusti, M. Colja, G. Brajnik, A. M. A. Marciniak, R. Sergo, D. D. Angelis, F. Glerean, G. Sparapassi, G. Jarc, S. Carrato, G. Cautero, and D. Fausti. "Visible pump–mid infrared pump–broadband probe: Development and characterization of a three-pulse setup for single-shot ultrafast spectroscopy at 50 kHz". *Review of Scientific Instruments* 91.7 (2020), p. 073106.

Ringraziamenti

Ed infine eccoci qua, all'ultima pagina di questa tesi, la pagina dei ringraziamenti. Probabilmente l'unica pagina in cui non rischiate di leggere *Heterodyne* o *quantum state*. Non riuscirei a scrivere tutti i motivi per cui vi devo dire grazie, quindi non ci proverò nemmeno. Prendete questa pagina per quello che è: l'ultima pagina di una tesi dove posso scrivere (in italiano) quello che mi passa per la testa.

Il primo grazie va a Daniele. Grazie per tutti i consigli che mi hai dato quando ero davanti a scelte importanti, grazie per avermi permesso di essere parte di un gruppo fantastico e grazie per chiedermi sempre se voglio un caffè anche se non ti do mai la soddisfazione di un sì. Grazie anche per aver tifato Inter in finale. Giuro che alla prossima occasione ricambio.

In secundis, grazie a tutto il gruppo per le chiacchierate sulla fisica ma soprattutto per le pizzate, le pause caffè e tutto quello che rende questo ambiente così speciale. Quindi grazie Francesca, Angela, Giacomo, Giorgia, Alexandre ... e ovviamente Filippo. Ti sei sorbito due tesi su due. Prometto che alla prossima ti lascio in pace.

Passiamo quindi a chi in questi cinque anni ha condiviso questo percorso da pazzi (furiosi), andando a costituire un *gruppo perfettamente normale*. Grazie Mene, Virtus, Giamma, Stizzale, Pedro, Giova, Mason, Claudia (non sai quanto volevo scrivere Botoz) e due grazie a parte.

Il primo è per Seba. Grazie per aver condiviso gli stress da tesi, le storie da x2 e, quando si poteva, la stanza. Non hai mai provato a strozzarmi nel sonno, e lo reputo un grande attestato di stima.

Il secondo grazie è per Willy. Grazie per tutti i discorsi, le litigate, le gite, i tuffi nel fiume e tutto quello che non so esprimere a parole ma che spero si capisca comuque.

Infine grazie a tutte le altre persone che ho incontrato in questi cinque anni: Pietro, Alessandra, Jack, Carmen, Agnese, Cesare, Michele, Vito ecc ecc ecc

E ovviamente grazie Matteo. Perché sappiamo entrambi che svegliarsi con un tuo vocale di 10 minuti è preludio di una grande giornata.

Devo quindi ringraziare chi in questi cinque anni non è stato sui banchi con me, ma c'è stato fuori.

Grazie agli irriducibi dei *4 iperscazzai*, Maxi, Gabri e Giulio, per le pedalate, le *magnade in jugo* e per essere ancora in paziente attesa della fatidica grigliata.

Grazie a coloro che rispondono al motto di *Io non posso* (allargato) per le serate in molo, per quelle da giochi da tavolo e per avermi mostrato come anche un gruppo da *vacanze sul divano* può dare fuoco ad una casa a Capodanno. Quindi grazie Nik, Chiar(z)a, Cami, Niki, Ruzz e JJ.

Grazie poi a tutti quelli che in un modo o nell'altro sono entrati a far parte della mia vita. Grazie Marco per rullarmi sempre (o quasi sempre dai) a scacchi, grazie Dario per i tuoi *come stemo?* e *Ciò, grande!* e grazie Gio per essere sempre il ragazzo serio che ho conosciuto un giorno al campetto. Grazie Giulia per le partite a biliardo, grazie Thomas per le sciate e le domeniche in curva, grazie Matteo M. per tutti i pomeriggi all'Xbox e al mare. Grazie a Jari, Morena, Irene, Rebecca e a tutti quelli che hanno fatto parte della mia infanzia.

Infine grazie a tutti i compagni di spogliatoio che ci sono stati in questi anni, dalle giovanili alla C fino all'ultimo anno in PM. Grazie Tommy, Tosi, Frama, Albi, Maurone, Enrico, Maina, Piero ecc ecc ecc.

Grazie poi a Carla, per avermi condotto per tutta la vita nel mondo della musica, grazie al prof. Michelini per essere la spledida persona che è e grazie al mio pianoforte per essere (suo malgrado) ancora il mio fido compagno.

Un grazie a parte va per chi ha visto questo percorso iniziare ma non ne ha visto la fine. Grazie Dighi, per avermi mostrato che anche la situazione più brutta si può prendere con il sorriso. E grazie ovviamente per avermi insegnato come si avvitano i barattoli.

Infine grazie Nonno per avermi insegnato col tuo esempio che, se la salita sembra invalicabile, bisogna abbassare la testa (tapparsi le orecchie) e pedalare, che prima o poi la cima arriva.

L'ultima parte dei ringraziamenti è dedicata a chi ha reso tutto questo possibile. Non è solo retorica: senza di voi non ce l'averi mai fatta. Quindi grazie a tutta la mia famiglia, ceppo Rigoni o Ziviz che sia. In particolare grazie alle Nonne, per le telefonate, i pranzi e il sostegno che non mi avete mai fatto mancare.

Dulcis in fundo, grazie Mamma e Papà. Credo sappiate quanto vi voglio bene, ma in caso: vi voglio bene. Quello che non credo di essere mai riuscito a comunicarvi appieno è quanto profonda sia l'ammirazione che nutro nei vostri confronti. Da grande non voglio fare il fisico, il musicista o chissà che. Da grande voglio essere come voi. Grazie.